

# Monte Carlo Techniques for Electron Radiotherapy

**UNIVERSITY OF THESSALY**

**SCHOOL OF HEALTH SCIENCES – FACULTY OF MEDICINE**

**DEPARTMENT OF MEDICAL PHYSICS**

Head: Professor Constantin Kappas

---

**A thesis submitted in fulfillment of the requirement for the degree of**

**Doctor of Philosophy**

**By: Hiba Baha Eldin Sayed Omer (B.Sc., M.Sc.)**

Larissa- Greece

2009

## **Committee Members:**

### **Supervision Committee:**

- Professor C. Kappas, Head of Medical Physics Department, University Hospital of Larisa, University of Thessaly
- Assistant Professor K. Theodorou, Medical Physics Department, University Hospital of Larisa, University of Thessaly
- Professor I. Fezoulidis the Head of Radiology Department, University Hospital of Larisa, University of Thessaly

### **Examination Committee:**

Professor C. Kappas

Professor I. Fezoulidis

Assistant Professor K. Theodorou

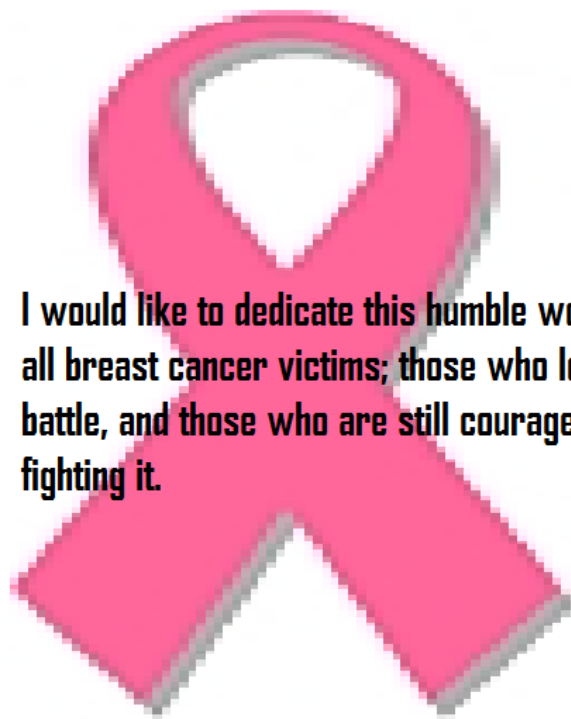
Professor G. Panagiotakis

Professor A. Germanis

Assistant Professor P. Georgoulas

Assistant Professor G. Kyrgias

## **Dedication**



**I would like to dedicate this humble work to  
all breast cancer victims; those who lost the  
battle, and those who are still courageously  
fighting it.**

**Hiba**

**Larisa, 2009**

## Acknowledgment

I would like to sincerely thank all those who stood by my side during my PhD. period; those who assisted me academically, financially and emotionally.

I am ever so grateful to my supervisor **Prof. C. Kappas**, Head of the Medical Physics Department for his continuous support. Prof. Kappas was the first person whom I met when I arrived in Greece. He met me at the airport in Athens and drove me all the way to Larisa. From him I learnt my first Greek word **ευχαριστώ** and ever since then he had offered me all guidance and support. I also learnt from him the value of being humble regardless of one's achievements and status.

I am also extremely grateful to my supervisor **Assistant Professor K. Theodorou**, who had offered unlimited and unconditioned help and support throughout my years in Greece. I learnt from Dr. Theodorou many things including research skills and intellectual thinking and sorting of matters. I also learnt from her some supervision skills, which will help me in my academic career. Thanks for all the time, discussions and guidance.

I would like to express my gratitude to **Prof. I. Fezoulidis** the Head of Radiology Department for providing all the facilities needed for my research.

I don't find sufficient words to express my gratitude to my friend and colleague **Thomas Kilindris** for all the help and support he gave me. Thanks "White Man" for all the technical support and all the discussions we had in the Lab, which made my life more enjoyable. Thanks also for XSTING!

I would also like to thank **Dr. I. Tsougos** for all the help and comments. I learned from Ioannis many computing skills and how to present my results, so thanks for that. Also, thanks for DORES.

My gratitude extends to the entire Monte Carlo group who worked in the Lab during these years; including **Anestis, Miltos, Yannis and Panagiotis**. I would

also like to thank all my colleague researchers and the Physicists at the Medical Physics Department, and all the doctors, nurses and technicians at the Radiotherapy Department.

I am also very grateful to **Prof. C Malizos** and the staff of the Orthopedic and Orthopedic surgery department for saving the life of the most precious person in my life; my mother.

I would also like to thank my friends **Sanaa, Moneim, Hassan, Albiona, Fawaz, Wasim and Hassan** and all the Sudanese and Arab friends in Larisa, Volos, Thessaloniki and Athens for their care and support. Thanks **Dr. Resoul Jwad** for helping me with the Greek language lessons, which allowed me to pass the tough Greek language exam.

Thanks **mom, Mohamed, Isam** and all family, **Omaima** and friends in Sudan for your prayers and support. It gave me strength whenever I felt weak.

Last but not least, I was generously financially supported by:

- The Greek Scholarship Foundation 2005-2009
- Ahfad University for Women Sudan 2004-2009
- Dr. Marten Durieux, and Maurits Wijzenbeek from Holland
- Dr. Hassan Sakkota, Eltadamoun Islamic Bank, Sudan
- My family
- I. Pantalos, ELEKTA Company in Greece: funded me to attend the Monte Carlo workshop and Group meeting in UK in 2006.

I am very grateful for all your help, which made my PhD. possible and my dream come true!

**Hiba, Larisa, 2009**

## **Abbreviations**

Pdd= percent depth dose

Dmax= depth of maximum dose

PTV= planning target volume

FWHM= full width at half maximum

SSD= source-to-surface distance

PMRT= postmastectomy radiotherapy

MC= Monte Carlo

DVH= Dose Volume Histogram

TCP= tumor control probability

NTCP= normal tissue complication probability

DORES= Dose Response Evaluation Software

BED =biologically effective dose

EUD= equivalent uniform dose

# List of Tables and Figures

## Tables

<b>Table 1:</b> The different models used by DORES and the associated set of parameters	59
<b>Table 2:</b> Nominal energy, input energy and energy distribution values	73
<b>Table 3:</b> Summary of effects of input parameters (beam/phantom)	111
<b>Table 4:</b> Effect of Linac configurations	113
<b>Table 5:</b> NTCP and EUD values for lung fibrosis for different scenarios	118
<b>Table 6:</b> NTCP and EUD values for pneumonitis for different scenarios	118

## Figures

<b>Figure 1:</b> Percent depth dose specification for electron beams	18
<b>Figure 2:</b> Interactions of a 10 MeV photon on a slab of lead	30
<b>Figure 3:</b> ELEKTA linear accelerator	39
<b>Figure 4:</b> Isodose lines on the XY plane as displayed by DOSXYZ_show	57
<b>Figure 5:</b> manual organ delineation as performed by XSTING	59
<b>Figure 6:</b> Patient Therapy Data form	61
<b>Figure 7:</b> Linac, component modules and simulated Linac	64
<b>Figure 8:</b> the main input parameters chosen for simulating the Linac	65
<b>Figure 9:</b> DORES primary software components	71
<b>FIGURE 10:</b> 4 MeV verification graphs 6X6, 10X10, 14X14 and 20X20 cm <sup>2</sup> field sizes	74
<b>FIGURE 11:</b> 6 MeV verification graphs 6X6, 10X10, 14X14 and 20X20 cm <sup>2</sup> field sizes	75
<b>FIGURE 12:</b> 8 MeV verification graphs 6X6, 10X10, 14X14 and 20X20 cm <sup>2</sup> field sizes	76
<b>FIGURE 13:</b> 10 MeV verification graphs 6X6, 10X10, 14X14 and 20X20 cm <sup>2</sup> field sizes	77
<b>FIGURE 14:</b> 12 MeV verification graphs 6X6, 10X10, 14X14 and 20X20 cm <sup>2</sup> field sizes	78
<b>FIGURE 15:</b> 15 MeV verification graphs 6X6, 10X10, 14X14 and 20X20 cm <sup>2</sup> field sizes	79
<b>FIGURE 16:</b> 18 MeV verification graphs 10X10cm <sup>2</sup> field sizes	80
<b>FIGURE 17:</b> Effect of alterations of the energy width on pdd and profiles	81
<b>FIGURE 18:</b> Effect of alterations of the source-to-surface distance on pdd and profiles	82
<b>FIGURE 19:</b> Effect of alterations of the size of voxels on pdd and profiles	83
<b>FIGURE 20:</b> Effect of the secondary scattering foil walls on pdd and profiles	84
<b>FIGURE 21:</b> Effect of alterations of the ionization chamber design on pdd and profiles	85
<b>FIGURE 22:</b> Effect of the mirror on pdd and profiles	86
<b>FIGURE 23:</b> Effect of alterations of the jaws opening on pdd and profiles	87
<b>FIGURE 24:</b> Effect of applicator materials on pdd and profiles	88
<b>FIGURE 25:</b> Isodose lines for 6 and 12MeV as given by DOSXYZ_show and XSTING	89
<b>FIGURE 26:</b> comparison between DVH values and isodose and 3D images	90

<b>FIGURE 27-a-b:</b> Isodose lines and DVH for 6 MeV	92-93
<b>FIGURE 28-a-c:</b> Isodose lines and DVH for 8 MeV	94-96
<b>FIGURE 29-a-c:</b> Isodose lines and DVH for 10 MeV	97-99
<b>FIGURE 30-a-c:</b> Isodose lines and DVH for 12 MeV	100-102
<b>FIGURE 31-a-c:</b> Isodose lines and DVH for 15 MeV	103-105
<b>FIGURE 32:</b> DVH for 8, 10, 12 and 15 MeV at gantry angle 50	106
<b>FIGURE 33:</b> NTCP for lung fibrosis	107
<b>FIGURE 34:</b> NTCP for pneumonitis	108
<b>FIGURE 35:</b> Different target areas including the chest wall IMN and SCV nodes	119



## Abstract

In this work simulation of electron beams and electron postmastectomy radiotherapy are evaluated using Monte Carlo Techniques. To achieve this several steps were followed.

The first step was to perform measurements for dose distributions on a water tank for the different energies and field sizes provided by ELEKTA SL18 Linac available at the University Hospital of Larisa. The measurements were performed for the central axis percent depth dose (pdd), and the off-axis dose profiles at the depth of maximum dose (Dmax). Choosing, installing and using a code for the simulation of the Linac follow this. EGSnrc and the accompanying BEAMnrcMP, DOSXYZnrc and BEAMDP codes were installed. The linear accelerator was simulated using the manual provided by ELEKTA Company as a guide. Percent depth dose and dose profiles were generated and compared with the measurements and fine tuning was made to match the measurements and calculations in order to verify the simulated Linac.

To reach a good match on the pdd curves several trials were performed changing the energy of the beam and the energy width, or full width at half maximum. The differences for the PDD curves were more significant in the build-up region and especially at the surface. Possible contaminating neutrons, scattered electrons from the phantom, dependence on the measuring device, the choice of the effective point of measurements and other parameters could be responsible for this mismatch. The mismatch becomes much smaller as the beam energy increases. On the other hand a slight discrepancy between measurements and calculations is noticed at the fall-off region with higher energies. But, in general these differences are within the 2%-2mm range.

Regarding the off-axis dose profiles there was a good match between measurements and calculations. To get to this agreement a slight change in the jaws opening had to be made. The major discrepancy between measurements and calculations was in the right shoulder, where the measurements showed slight depression for some energies and field sizes. When one shoulder is apparently depressed and varies from the other one that is in a good match with MC calculations we consider that the profile is verified.

In the second part of the work, the different sources of systematic error in linear accelerator simulations were studied. This includes slight alterations in the input beam parameters, the phantom design and placement and the configuration of the Linac

components. This study aims at helping future researchers assess from the discrepancy between measured and calculated Pdd and dose profiles, where the mistake in simulation could possibly be.

Simulation of low energy beams was found to be more sensitive to the components that lie perpendicular to the direction of the beam even the very thin mirror, while high energy electron beams are more influenced by alterations at the edges of the beam like the walls of the scattering foils and the applicators.

Percent depth dose curves on the other hand are more influenced by accurate modeling of the different parts of the linear accelerator, especially at depths below Dmax. Little effect is noticed as a result of altering the beam parameters on the percent depth dose before Dmax. Beam and phantom input parameters, as well as some Linac components like scattering foil walls, jaws opening and material of the applicators affect the off-axis dose distributions by altering the side scatter.

In the third part XSTING code, which was used for stereotactic radiosurgery was re-coded to accept input doses from EGSnrc and tested. The generated isodose distributions were compared with those from the benchmarked DOSXYZ\_show. DVHs were also verified using two simple visualization methods. The DVHs could not be compared with DOSXYZ\_show because the latter does not produce allow organ delineation and thus generation of DVHs. Then electron beams with different energies, field sizes and angles of inclination were used for postmastectomy radiotherapy studies. The DVHs generated by XSTING were used as input for the dose response software DORES to assess the effect of this treatment modality on the lung via studying the predictors of pneumonitis associated with postmastectomy electron beam radiotherapy.

Postmastectomy evaluation using XSTING and DORES reveals that the probability of radiation induced pneumonitis in electron postmastectomy radiotherapy is fairly low. The risk increases with increasing energy and gantry angle.

Postmastectomy radiotherapy cannot be performed with a single electron beam, because regardless of the energy, field size or angle, it is not possible to provide adequate target coverage. Multiple electron, photon or electron/photon mix fields with appropriate field shaping using cut-outs or a bolus with partitioned target area will allow better target coverage.

## Contents

Committee Members: .....	2
Supervision Committee: .....	2
Examination Committee: .....	2
Dedication.....	3
Acknowledgment .....	4
Abbreviations.....	6
List of Tables and Figures .....	7
Tables .....	7
Figures .....	7
Abstract .....	9
Contents .....	11
CHAPTER ONE: INTRODUCTION.....	14
1.1 Preface .....	15
1.2 Conformal radiotherapy .....	16
1.2.1 Treatment planning for conformal radiotherapy .....	16
1.2.2 Requirements for conformal treatment planning .....	16
1.3 Electron beam radiotherapy .....	17
1.3.1 Interactions of Electrons with Matter.....	17
1.3.2 Percent depth dose specification .....	18
1.3.3 Electron treatment planning basics .....	19
1.4 Postmastectomy Radiotherapy .....	20
1.4.1 Introduction.....	20
1.4.2 Indication of PMRT .....	21
1.4.3 Challenges in breast cancer irradiation:.....	22
	11

1.4.4 Complications .....	23
1.4.5 The main techniques used for postmastectomy irradiation .....	26
1.5 Monte Carlo Techniques in Radiotherapy: .....	29
1.5.1 Why EGSnrc .....	32
1.5.2 Goal of MC in treatment planning .....	33
1.5.3 Clinical sites for which Monte Carlo may be useful .....	33
1.5.4 Dose response evaluation .....	34
1.6 Objectives of the work .....	34
1.7 Description of the thesis .....	35
CHAPTER TWO: MATERIALS AND METHODS .....	37
2.1 Materials: .....	38
2.1.1 ELEKTA SL18 .....	38
2.1.2 EGSnrc .....	39
2.1.3 XSTING .....	57
2.1.4 Dose Response Evaluation Software: DORES .....	60
2.2 Methods .....	62
2.2.1 MEASUREMENTS .....	62
2.2.3 LINAC SIMULATION AND VERIFICATION: .....	62
2.2.4 Evaluation of sources of systematic errors in simulations .....	66
2.2.5 Electron postmastectomy radiotherapy .....	68
CHAPTER THREE: RESULTS .....	72
3.1 Measurements .....	73
3.2 LINAC SIMULATION AND VERIFICATION: .....	73
3.3 Evaluation of sources of systematic errors in simulations .....	81
3.4 Electron Postmastectomy Radiotherapy .....	89
3.4.1 Verification of XSTING .....	89
3.4.2 Electron Postmastectomy Radiotherapy .....	91
CHAPTER FOUR: DISCUSSIONS .....	109

4.1 LINAC SIMULATION AND VERIFICATION:.....	110
4.2 Evaluation of sources of systematic errors in simulations.....	111
4.3 Electron Postmastectomy Radiotherapy .....	113
4.3.1 XSTING.....	113
4.3.2 Electron Postmastectomy Radiotherapy.....	114
CHAPTER FIVE: CONCLUSIONS AND RECOMMENDATION .....	121
5.1 Conclusions .....	122
5.2 Recommendations.....	123
Περίληψη.....	125
References .....	128
APPENDIX .....	136
APPENDIX 1: Worksheet for measurement correction .....	136
APPENDIX 2: Stopping power ratios.....	139
APPENDIX 3: Ionization to dose conversion example .....	140
APPENDIX 4: The different component modules of BEAM .....	141
APPENDIX 5: DORES output chart.....	142

# **CHAPTER ONE: INTRODUCTION**

## 1.1 Preface

Cancer patients are treated by a variety of options. Treatment options are determined by the type and stage of the cancer and include surgery, radiation therapy, chemotherapy, immunotherapy, etc. Often, a combination of those treatments is used to obtain the best result.

Radiation is a special kind of energy carried by waves or a stream of particles. High dose radiation can be used to treat cancer and other illnesses. It can be delivered from outside of the patient using special machines (teletherapy) or deposited from radioactive substances within the patient (brachytherapy). In the case of external radiotherapy different types of particles are used: photons in the kilovoltage (kV) or megavoltage (MV) energy ranges, electrons, neutrons, protons, or other ions.

The rationale for radiotherapy with electron and photon beams stems from the findings that these funds of radiation are endowed with properties that enable them to interact disruptively in the human body at the cellular level by the initiation of a shower of ionization and excitation events. By strategically choosing the beams and directing them at the neoplastic mass, selective killing of the tumor cells and sparing of normal surrounding tissues may be accomplished. The differential response of normal cells and tumor cells to these kinds of radiation makes it possible to plan a treatment that optimizes the differential response by the strategic employment of dose fractionation schemes. Acceptable plans ensure adequate tumoricidal dose coverage and the simultaneous dosimetric sparing of normal tissues to levels below the known thresholds of complications or radiation-induced carcinogenesis. The preferred plan is the one that optimizes these objectives based on some criteria. Thus radiation therapy with electron and photon beams may be considered to be a clinical optimization process in which certain physical characteristics of radiation transport are extracted to achieve selective cell death in tumorigenic populations of cells by biological, biophysical and biochemical processes.

Critical to the meaningful evaluation of treatment plans are the accurate delineation of the absorbed dose distributions within patients and the availability of the means to deliver them with high fidelity. [1]

## 1.2 Conformal radiotherapy

Conformal radiotherapy has been defined as a procedure of high-precision irradiation of a target volume where the 95% isodose of the dose distribution, or more generally, the high-dose (treated) volume conforms as closely as possible to the shape of the target volume in three dimensions. Whereas initially conformal radiotherapy was concerned with the optimal shape of radiation fields around the PTV, nowadays the focus is shifting to define also an optimal intensity distribution of energy fluence within the fields.

### 1.2.1 Treatment planning for conformal radiotherapy

Treatment planning can be defined as the radiotherapy preparation process in which treatment strategies are defined in terms of planning target volumes, dose distributions tailored to these volumes, and sets of treatment instructions to deliver the dose distributions. Treatment planning plays a key-role in the advancement of radiotherapy. A shortlist of suggestions for accurate treatment planning comprise: (a) better visualization of tumor and normal tissue, (b) presentation of uncertainty bands around isodoses, (c) monitoring of target tissue during treatment, (d) gating of treatment, (e) computer-controlled treatment and (f) reduced treatment volumes. [2]

The present status of advances in treatment technique can be assessed in the light of this historical shortlist. The mentioned suggestions are now entering clinical practice. Modern treatment planning systems indeed have much improved visualization facilities, although especially accurate delineation of tumor and clinical target volumes remains to be one of the greatest challenges. In this perspective, multi-modality imaging, such as CT, MR and/or PET images, and image registration can be of considerable value to better define and, if possible, reduce target volumes. Monitoring of targets is readily approaching the realm of practical feasibility, based on markers of clinically acceptable size that can be automatically detected. Gating of a linear accelerator (Linac) triggered by the breathing cycle is an emerging application. [3, 4, 5, 6]

### 1.2.2 Requirements for conformal treatment planning

The successful application of especially these enhanced conformal techniques depends critically on a very high level of accuracy in both treatment planning and treatment execution. Knowledge about the accuracy of treatment techniques is obtained by appropriate verification. This can be a verification of an entire technique, usually by



application of a phantom in which calculated dose is compared to measurements, e.g. by film, a combination of scans in a water phantom and gel dosimetry.

## 1.3 Electron beam radiotherapy

### 1.3.1 Interactions of Electrons with Matter

The charge and relatively small size of the electron cause its interactions with matter to be rather unique compared to those of photons and other charged particles. Most of the interactions that lead to the loss of the incident electron's energy are inelastic collisions with atomic electrons leading to excitation or ionization transfers, and with atomic nuclei leading to radiative transfers. Elastic interactions with the atomic nuclei are the primary mode by which these electrons are scattered. Those with the atomic electrons are significant only in the energy range less than approximately 100-eV. The kinds of interactions that would occur depend on the kinetic energy of the electrons and their proximity to the atomic electrons or nuclei. If the distance of the electrons is large, comparable or small with the atomic dimensions, the interactions are predominantly with the whole atom, atomic electrons and the nucleus respectively.

The first two interactions described above cause atomic excitation or ionization and may be classified as soft and hard collisions respectively. The distinction is based on the fraction of incident electron energy lost per interaction relative to the kinetic energy of the incident electron. The total energy lost by all soft interactions however is comparable with that lost in hard collisions. The electrons ejected from the atomic orbitals from hard collisions usually have enough kinetic energy to independently undergo their own respective collisions and are called  $\delta$ -rays. The interactions of electrons with distant atoms are complicated by the polarization effect in solid and liquid media that causes the energy losses to be reduced by the action of intervening atoms. Classical and quantum-mechanical approaches have been used to study the ionization and excitation losses of electrons. The stopping-power for ionization losses is essentially inversely proportional to the electron energy between 10 to 100-keV and nearly constant after that. The reason is that the stopping power is inversely proportional to  $\beta^2$  and at higher energies relativistic speeds  $v$  are attained by the electrons and the ratio  $\beta = v/c$  approaches unity, where  $c$  is the speed of light. Materials with higher  $Z$  have a lower stopping-power in general because of the higher ionization potentials associated with higher  $Z$ . The third interaction leads primarily to radiative energy losses (bremsstrahlung) that again according to quantum-electrodynamics theory can be classified as soft or hard relative to the kinetic energy of the

incident electrons. The corresponding stopping-power increases rapidly with  $Z$  and somewhat more slowly with the energy of the electrons. Another possible interaction is an in-flight interaction of positrons. Positrons may interact with an electron encountered en route that will result in annihilation of both and the manifestation of their kinetic energies as two photons. [7, 8, 9]

For over 50 years, electron beam therapy has been an important radiation therapy modality. A single electron beam delivers a uniform 'plateau' of dose ranging from 90% to 100%, of maximum central-axis dose with the dose distribution steeply falling off both laterally and distally. This allowed superficial cancers and disease (within 6 cm of the patient's surface) to be irradiated with little dose to underlying normal tissues and structures, something usually not possible with x-ray therapy. Electron beams are clinically utilized in the treatment of several malignant conditions including; total skin, head and neck (where the proximity of critical organs e.g. the eyes, spinal cord and brainstem, to the majority of the primary lesions and lymph nodes require great care in treatment planning) and the chest wall (where electron beams present the solution to the tedious localization procedures required for photon treatment plans).

At beam energies greater than approximately 20 MeV, depth-dose curves lose their sharp fall-off and begin taking on characteristics of photon beams due to bremsstrahlung energy loss, whereas their penumbrae broaden with depth due to increased multiple coulomb scattering. [10]

### 1.3.2 Percent depth dose specification

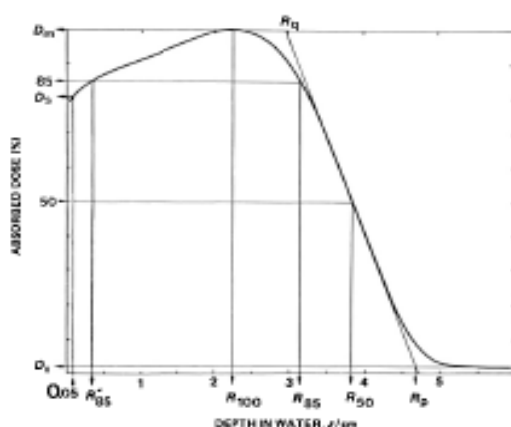


**Figure 1:** Percent depth dose specification for electron beams

In selecting the appropriate beam energy to be used for a specified clinical case, the first consideration is matching the central-axis depth-dose curve parameters to the clinical situation. In accordance with the ICRU 35(1984), several parameters are used to characterize the electron beam central-axis depth-dose curve. Each of these parameters ( $\%D_s$ , relative surface dose at 0.5mm,  $\%D_x$ , relative dose due to x-ray component,  $R_t$ , therapeutic range,  $R_{100}$ ,  $R_{50}$ , and  $R_p$ , depth of maximum dose  $D_{max}$ , depth of 50% dose level and the practical range respectively, and  $G_0$ , the normalized dose gradient) is of clinical importance and can be affected by small differences in energy, scattering foils, collimation and source-to-surface distance (SSD) as shown in figure 1 above [7, 10, 11].

### 1.3.3 Electron treatment planning basics

There are several physical characteristics of the electron beams and fundamental principles that must be considered when planning patient treatment with electron beams:

**Sharp dose fall-off and energy selection:** a unique property of electron beams is that their sharp fall-off in depth-dose beyond  $R_{80}$  (depth of 80% of maximum dose on distal fall-off) offers protection for anatomical structures beyond the PTV. This allows superficial PTVs to be treated with a single en-face beam, something not possible with photon beams. The maximum depth of the PTV determines the beam energy; in unit density tissues, the electron energy should be at least approximately 3-3.3 times the maximum depth of the PTV in cm to cover the PTV with 80%-90% relative dose.

**Dose build-up:** within a few cm of tissue, the dose approaches 90% of the depth of  $D_{max}$  resulting in modest skin sparing. The relative surface dose is lowest for the low energy electron beams ( $\approx 70\%$  at 6 MeV) and greatest for the high energy electron beams ( $\approx 95\%$  at 20 MeV), which is the reverse of photon beams. If low energy electron beams are being used and a high skin dose is required, then bolus is often used to increase the skin dose, requiring the optimal energy-bolus combination.

**Constrictions of the isodose curve at depth:** there is considerable constricting of the 80%-90% isodose curves as the depth increases to  $R_{90}$ . This must be taken into account during treatment planning.

**Dose perturbation due to tissue heterogeneity:** due to the dependence of electron beam scattering and the range of electrons upon density and atomic composition, the effects of tissue heterogeneity upon the dose distribution are more pronounced for electron beams than for photons. The effects of irregular patient surface, bone, lung and internal air cavities on the dose distributions can be significant, causing dose heterogeneity in the PTV,

geographical miss of the PTV in depth and increased dose to normal tissues and critical organs. The impact of tissue heterogeneity on patient dose distribution, which is the subject of many early investigations into electron beam dose distributions, has been reviewed by Hogstrom (1983b, 2004), ICRU Report 35 (ICRU 1984) and AAPM radiation therapy committee task group no. 25.

**Beam mixing:** of photon and electron beams allows the planner to custom design the central-axis dose distribution. The function is particularly useful in patients for whom skin sparing is required, or for penetration slightly deeper than the therapeutic range for the highest energy electron beams [10].

## 1.4 Postmastectomy Radiotherapy

### 1.4.1 Introduction

Breast cancer was recognized by the Ancient Egyptians as long ago as 1600 BC. However, over the past 50 years it has become a major health problem affecting as many as one in eight women during their lifetime [12]. Breast radiotherapy constitutes a large portion of work in any radiation oncology department.

Mastectomy is one of the main options in the treatment of breast cancer patients in an aim to avoid metastases of the disease. Unfortunately, even after a successful operation, an appreciable risk of local recurrence (e.g., in the chest wall or lymph nodes) can remain unless some reliable method of investigation, such as axillary clearance, has found no evidence of nodal involvement. If axillary investigation reveals nodal involvement (or if the axilla has not been adequately investigated), other treatment modalities are mandatory [13].

Advances in diagnosis and treatment in oncology combined with technical advances in radiotherapy have resulted in qualitative and quantitative changes in the use of radiation to treat breast cancer. Over the past 5 decades, there have been more than 50 randomized prospective clinical trials that have evaluated the benefits of radiation after mastectomy for patients with breast cancer [14, 15]. The rationale for the use of post-mastectomy radiotherapy (PMRT) is to decrease locoregional recurrence and improve overall patient survival. Locoregional recurrence occurs mostly in the first five years after initial treatment and can be in the form of local or distant metastases in the body. It depends on many factors including pathological characteristics such as tumor size, nodal involvement, etc, and on the type of surgery. In patients who develop a locoregional recurrence, the chest wall is the most common site, with 70% of all locoregional failures involving the chest wall.

The mastectomy scar on the chest wall is the most common site of chest wall involvement. The supraclavicular / infraclavicular nodes are the next most common site (10-20%), with the axilla and internal mammary nodes being the least common (5 - 10%). [16, 17]

#### **1.4.2 Indication of PMRT**

There are several reasons or end points that might justify the use of postmastectomy radiotherapy (PMRT) for patients with invasive breast cancer. These include a reduction in the risk of locoregional failure (LRF), with its potential physical and psychological morbidity, as well as a reduction in the risks of distant relapse and death. There are a number of conditions that must be met in order for an individual patient to achieve a survival benefit from postmastectomy radiation. Pathologically close or positive margins of resection, tumor size of 5cm or greater and/or involvement of the chest wall or skin, vascular invasion and greater than three lymph nodes positive for metastatic disease are determinant factors for indication of PMRT. PMRT is also indicated for patients with persistent disease in the local-regional area after mastectomy and those who do not have foci of viable micro-metastatic disease outside of the radiation treatment fields. Radiation must be effective in eradicating the persistent disease in the local-regional area and must not cause a life-threatening injury [18-22]. The role of PMRT for stages I and II is a subject of research. Studies showed that there are no significant effects in the 10-year rates of locoregional recurrence rates, and is thus not recommended [23, 24]. Another controversial question regarding indication for postmastectomy irradiation is whether or not radiotherapy is indicated in patients with 1–3 positive nodes. In two different surveys in North America and Europe, the percentage of centers that would use postmastectomy radiotherapy in patients with 1-3 positive lymph nodes ranged between 40-63% and 35-85% in North America and Europe respectively [25, 26]. This is in-line with numerous recent consensus reports and guidelines concerning postoperative radiotherapy in breast cancer, where the recommendation is no radiotherapy to patients with 1–3 nodes positive as the only criterion. This was contradicted by the results from recent subgroup analysis that strongly indicate that the benefit of postoperative radiotherapy is equally pronounced in patients with 1–3 nodes positive and in patients with 4+ nodes [23, 27-29].

Pauline Truong et.al and The American Society of Clinical Oncology recommended several guide lines for PMRT, for details the reader is requested to go to the references [30, 31].

### 1.4.3 Challenges in breast cancer irradiation:

Irradiation, whether of the postmastectomy chest wall or in the setting of reconstruction, is complex, because of the large, curved target volume and its proximity to heart and lung. A number of challenges or issues should be considered as relevant to breast cancer radiotherapy. Within treatment planning, these include patient positioning, immobilization or localization, proximal-organ (heart lung or contralateral breast) irradiation, tumor motion or correction, dose homogeneity, especially in regions with inhomogeneities as the thoracic region, and cosmic effects. The accuracy of transfer of digital and non-digital data between planning and treatment units and the operator accuracy also affect the accuracy of irradiation. [32, 33]

TUMOR MOTION: Tumor motion can be divided into two categories: intrafractional motion which occurs during irradiation as a result of respiration, cardiac pulsation and gastro-intestinal systems and, interfractional motion which refers to the change or displacement during the course of treatment as a result in variation of tumor size and patients' weight. Motion of the treated volume during the course of treatment presents a big challenge in breast cancer irradiation. In a previous paper we showed that intrafractional variation ranged from 0.85 mm for the inferior central margin (ICM) to 2.1 mm for the central breast distance (CBD), while interfractional variations ranged from 3.2 mm to 6.25 mm for CBD and ICM respectively. Different techniques were suggested for actively and effectively adjusting these movements in order to optimize the treatment. These include breath holding control, respiratory gating techniques, electronic portal imaging, active breath control and real time tumor tracking. [34]

TISSUE INHOMOGENEITIES: The thoracic region is a heterogeneous medium composed of dense bone, water-equivalent soft tissues and lung tissues. A major concern in chest wall irradiation is the penetration of electrons into the lung. Since the lung has a physical density of only about 0.3, after penetrating the chest wall, the remaining portion of the depth-dose curve can penetrate three times deeper in lung than in unit density tissue.

INCREASED NUMBER OF PATIENTS AND TIME: The number of cancer patients who need radiation therapy is increasing every day. It is estimated that over a million breast cancers are diagnosed yearly worldwide. [12, 35] The time required for treatment plays an important role in the efficiency and quality of the service provided to patients. Any delay in treatment may negatively affect the patient especially if the cancer is of an aggressive type.

#### 1.4.4 Complications

Although the beneficial effect of postoperative radiotherapy for breast cancer is well documented, this treatment may be related to a number of complications that may affect patient quality of life and possibly survival. Among significant long-term irradiation sequelae are:

CARDIAC DAMAGE: Case reports of heart injuries resulting from postmastectomy radiotherapy were published as early as the 1950s. [36, 37] Ischemic heart diseases caused by irradiation of the cardiac chambers and coronary vessels are amongst the major causes of mortality in postmastectomy irradiation. This is specially the case when inclusion of internal mammary nodes that lie in close proximity of the heart is necessary. [38, 39] Cardiac damage is more associated with the irradiation of the vascular system than of the heart itself. [40] It is believed that the increase in the risk of myocardial infarction is associated with factors other than radiation, including: age, ethnicity, advanced stage, non-rural residence, more than one comorbid condition, a hormone receptor-negative tumor, and other cardiac risk factors. [41]

LUNG DAMAGE: The lung is one of the important dose limiting organs for radiation therapy of tumors in the thoracic region due to its proximity to the target volume. Pulmonary complications are divided into early effects (radiation pneumonitis) and late effects (lung fibrosis). Clinically, these conditions are usually diagnosed from chest x-rays in symptomatic and asymptomatic patients. [42] Both are confined to radiation portals: antero-lateral peripheral lung after chest wall irradiation or lung apex after irradiation of supraclavicular area. [43] The early phase of radiation induced lung injury, radiation pneumonitis, usually becomes manifested by cough, fever and dyspnea 1-6 months after treatment. The probability and severity of radiation induced lung damage depend mainly on the radiation dose, fractionation schedule and the amount of irradiated lung volume. The irradiated lung volume is a deterministic factor because of the structural organization of the functional subunits of the lung. However, the exact tolerance dose of the normal lung tissue is not fully known in humans. An early study showed that dose effect relation for early changes in perfusion and ventilation show an almost linear increase of the reduction in local function as a function of dose. This suggests that early local pulmonary changes can occur at fairly low dose levels with progressive dysfunction for doses up to 50-80 Gy. [44, 45]

The risks of cardiac and pulmonary toxicities are highly technique-dependent, so appropriate estimates of these risks could aid in clinical decision-making for selection of the

treatment field arrangements. Other factors such as age, sequential chemotherapy hormonal therapy and smoking and eating habits have been reported to influence pulmonary complications post irradiation.

SECOND MALIGNANCIES: Radiation-induced cancers are an uncommon but feared late complication of radiation therapy. Carcinogenic risk seems to be highest for tissues receiving low doses ( $\leq 6$  Gy). However, there seems to be a tissue-specific dose-response effect for radio-carcinogenesis, with radiation-induced sarcomas developing in tissues receiving higher doses (30–60Gy) and carcinomas developing in tissues receiving much lower doses. Both the integral dose to normal tissue and its dose distribution therefore influence this risk. [46]

The data on the incidence of second malignancies in breast cancer survivors are contradictory. ten and fifteen year cumulative incidences of all second tumors in women receiving radiotherapy for breast cancer are in the range of 16-19%, with a similar proportion of contralateral breast cancer and other tumors. Among the latter, as in the general population, the most common are skin, endometrial, colorectal and pancreatic cancers. However, some tumors seem to occur with relatively higher frequency. These include ovarian, uterine and lung cancers, leukemia, malignant melanomas and sarcomas. A proportion of these cases may be a result of misclassification of metastatic disease. Some of these malignancies may be related to interaction between radiation and genetic factors. Indeed, in some series, the use of radiotherapy was related to an overall increase in the risk of second tumors whereas others demonstrated no effect. For example, breast cancer radiotherapy increases the risk of leukemia and lymphomas, but not of thyroid cancer. The increased risk is observed predominantly in women diagnosed with breast cancer at a young age. [43]

OTHER SEVERE LONG-TERM SIDE EFFECTS, including lymphedema, brachial plexopathy, rib fractures, chronic pain, axillary vein thrombosis, bone necrosis, are relatively rare. These complications resulted from large daily doses combined with hot spots from overlapping fields experienced in Co-60 treatments. [20, 38, 43, 47, 48]

COMMON SHORT-TERM SIDE EFFECTS OF PMRT, including fatigue and skin erythema, are generally tolerable and not dose limiting. [43]

The radio-therapeutic doses received by the patient are limited by the tolerance of the normal tissues. Radiation is an unusual toxic agent, because the time of expression of cellular injury can be very variable from one tissue and tumor to another. Moreover, different patients given a standardized treatment can exhibit a range of normal tissue reactions. Thus, there is both dose dependence and variability in individual radio-



sensitivity. However, it is impossible to predict the late effect in normal tissues from the acute reactions. Radiotherapy practice has changed over the years with the recognition of the importance of fraction size, number of fractions, total dose, and overall time for both tumor and normal tissue reactions. A clear distinction has been found between the response of early reacting tissues, which are not much influenced by the size of the dose per fraction, and late reacting tissues for which the fraction size is crucial. In addition, it has been recognized that shorter schedules are more damaging to tumors and early reacting tissues, but these do not increase the damage in critical late reacting tissues. In general, there has been a move toward more and smaller fractions to spare late reactions and to smaller fields in more clearly defined risk groups. The success of RT has thereby led to longer patient survival. [47]

The risks and benefits of postmastectomy radiation treatment for breast cancer patients has been one of the most comprehensively studied topics in all of oncology. Indeed, some of the very first randomized trials in the history of medicine investigated the role of radiation after radical mastectomy. Fortunately, radiation is a highly effective treatment modality for breast cancer. Multiple studies have indicated that radiation reduces the relative risk of local-regional recurrence by 65%-75%. [21, 23, 29, 40, 49-53] Comprehensive meta-analyses of patients in randomized trials of radiation therapy for operable breast cancer have failed to resolve a fundamental question: whether the reduction of locoregional recurrence associated with postoperative radiation therapy is reflected in improved overall survival. In general, these meta-analyses have concluded that postoperative radiation therapy was not statistically significantly associated with increased overall survival at 10 years. Moreover, they have shown that any reduction in breast cancer mortality has been offset by mortality from late side effects of radiation therapy, including heart disease and lung damage. This conclusion has profoundly affected multidisciplinary management of operable breast cancer.

The results of these meta-analyses were based on studies performed by older radiotherapy techniques, where the target volume was more extensive and were thus associated with an excess risk of cardiovascular and pulmonary toxicities. [54, 55] Moreover these meta-analyses were not based on dosimetric analysis. The estimation of the radiation induced risks of today's breast radiotherapy requires the development of reliable dose-response relationships, which, in turn, require detailed organs at risk OAR dosimetry of past regimens given to women for whom long-term follow-up data is available. For example, at present, few heart dosimetry data from breast cancer RT are available. Furthermore, it is unknown which quantitative measures of the heart dose or

volume is most relevant to subsequent heart disease risk. Studies have used a variety of heart dose specifications, including the absorbed dose, biologically effective dose (BED), and the “cumulative radiation effect” (an estimate of the biologic radiation dose). Published data recording the percentage volume of the heart irradiated to various doses are limited. Such information might, however, be important in assessing radiation-related heart disease, because the percentage volume of the heart irradiated to a certain “threshold” dose might be a better predictor for cardiac death than, for instance, the mean heart dose or BED. Information is also needed concerning the effect of irradiating different cardiac structures, especially the coronary arteries. Coronary artery doses have been reported for several techniques, but only for left-sided irradiation; however, most studies have reported only the mean dose to the whole heart. [56]

In the past two decades, new equipment and techniques for radiation therapy have led to a better understanding of the dose–response relationships in the control of sub-clinical breast cancer. This substantially raises the possibility that a more effective dose to the target volume that avoids direct irradiation of the organs at risk could be associated with improved outcomes in patients treated with postoperative adjuvant radiation therapy.

#### **1.4.5 The main techniques used for postmastectomy irradiation**

**PHOTON IRRADIATION:** Photon beams from linear accelerators or from Cobalt-60 sources are widely used in postmastectomy radiotherapy. The different applications of photon beams include:

***Standard tangents:*** this is one of the most common techniques used to treat the chest wall where the chest wall is treated by two opposed tangential fields. The internal mammary nodes (IMNs) are either treated with antero-posterior (AP) electron fields of high energy or mixed electron-photon beams or are not intentionally treated. Anterior or AP photon field are prescribed to the Supraclavicular fields (SCF). [18, 40, 57, 58]

***Cobalt fields*** are also used in some radiotherapy departments. In this technique the medial CW and IMNs are treated by an anterior 60Co field and the SCF is treated with a 60Co beam as per standard tangents. [57]

***Reverse Hockey Sticks:*** This term refers to traditional opposed photon-only CW field in an inverted L fashion, with an abutted anterior field treating the medial CW, IMN and SC lymphatics. [57, 59]

***Partially wide tangent fields (PWTFs):*** This plan was generated with the explicit use of the 3D planning system to identify and treat the IMNs in the first three

intercostal spaces. Medial and lateral coplanar photon tangents are used. The inferior medial CW (heart shadow) is treated with supplemental electrons (6 or 9 MeV). The SCF are treated as per standard tangents. Adequate blocking can be added to spare the contralateral breast, the heart and the lungs. [57, 60, 61]

**ELECTRON IRRADIATION:** The use of electrons for chest wall radiation has been criticized because of reports of pulmonary toxicity. Some earlier studies concluded that patients treated with electron-beam therapy to the chest wall had a higher incidence of pulmonary toxicity. However, the energy of electron beam used to treat those patients was 8 MeV or greater, which has more penetration to the underlying pulmonary tissue. In addition, the prescription point for radiation therapy was the subcutaneous tissue/chest wall junction in many of these studies. [18]

**Anterior electron** fields of energies ranging from 6 to 12 MeV are commonly used to treat the CW IMN's and SCF. An additional posterior field is usually necessary for patients with large AP distance. An electron boost is sometimes recommended to account for the obliqueness of the peripherals. [16, 22, 54, 57, 60]

A technique for CW and IMN irradiation using **oblique electron** fields with gantry angles of 20-30° and with energies of 7.5, 9 and 10.5 MeV was reported to improve coverage of the PTV and minimize irradiation of OAR's. Additional photon boost or mixed photon-electron beams to the IMN and SCF are usually used. [62]

**Electron Arc radiotherapy:** in which the irradiation is performed in 3 segments of 40° each with a customized secondary collimator for each segment is the modality of choice in several radiotherapy departments. Electron fields of energies 9, 12 and 16 MeV are used in the medial segment for the CW and IMN and 6 MeV or 9 MeV are commonly used for the medial and lateral segments. [63, 64]

**Electron rotation technique:** is designed for treating the whole CW, with electron energies between 4 and 10 MeV and a shortened electron applicator. IMNs are treated with mixed electron/photon beams. The starting and end points of irradiation are identical and the irradiated areas outside the target volume of rotational electron field are masked with lead rubber. [49]

**PHOTON ELECTRON MIX:** Using this technique the patient is usually placed in a tilted board. Medial and lateral photon tangents are used for the lateral CW and mixed photons and electrons with ratios (30%/70% or 20%/80%) are used for the medial CW and IMN. [57] A combined 3-field photon electron mix, [61] the modified Kuske effect which employs a 4-field photon electron combination where a direct photon and an angled electron field

covered the IMN region and two shallow tangents covered the chest wall but excluded the IMN were also investigated. [59]

The advantages of mixing as well as sequentially combining fixed electron and photon beams are:

1. Less severe acute and chronic skin reactions even with boost doses added to higher tumor risk areas.
2. Improved homogeneity through the chest wall thickness compared to the use of electrons alone.
3. Decreased lung, heart, mediastinal and spinal doses when compared with photons alone.
4. Fewer match line skin reactions.
5. No apparent compromise of loco-regional control rates. [65]

**PROTON IRRADIATION:** Proton beam therapy is characterized by remarkable depth-dose distributions that have a low to median entrance dose, followed by a unified high-dose region (Bragg peak region) in the tumor area, followed by a steep fall-off to zero-dose distal to the target. As a result, physical dose distributions with protons are both highly conformal and homogeneous. It must be emphasized that protons have biologic effects in tissue similar to those of the megavoltage photons used in conventional therapy. They are regarded as low linear energy transfer particles, unlike other non-conventional radiotherapy particles, such as neutrons or carbon ions. The unique dosimetric features of the Bragg peak of proton therapy make it an attractive treatment modality of three-dimensional conformal external beam radiotherapy. The target dose inhomogeneity encountered with mixing photon and electron beams is thus overcome by the use of proton beams.

Proton beam therapy, however, is more costly than conventional treatment, and any potential benefits must be assessed in the light of the associated costs to the health-care system. Yet it is reasonable to assume that the expense of proton therapy per patient will decrease, as more facilities are built and greater numbers of patients treated. [66, 67]

**INTRAOPERATIVE RADIOOTHERAPY (IORT):** Intraoperative radiotherapy with electrons delivers a single fraction of 21 Gy directly to the tumor bed after wide excision or quadrantectomy, using a mobile linear accelerator in the operation theatre. It has a low inhomogeneity index, with high sparing of surrounding tissue. [66]

**BRACHYTHERAPY:** This is a form of accelerated partial breast irradiation APBI technique in which multi-catheter or single catheter (e.g. MammoSite balloon) high dose rate HDR or low dose rate LDR inserts are used to deliver high doses to the target and lower doses to

the OARs. It is mainly used for patients with a low risk of multi-focal, multi-centric or lymphatic recurrences. [66]

*INTENSITY MODULATED RADIOTHERAPY (IMRT)*: was explored as a technique to improve breast dose homogeneity by decreasing hot spots and dose to normal tissues thus reducing acute and late toxicities. IMRT removes the usual reliance on flat (or uniform intensity) radiation fields and, instead, replaces that simple paradigm with a variable intensity pattern that is usually determined with the aid of a computerized optimization algorithm. Complex dose distributions are achieved using irregular fluence maps obtained through optimization processes. Despite significant improvements in dose inhomogeneity have been demonstrated in these studies, enthusiasm for widespread use of IMRT for breast cancer has been tempered because the breast has been successfully treated with other modalities for many years, resulting in excellent local control rates, low rates of pulmonary and cardiac complications, and excellent cosmesis in most patients. [68- 71]

The optimal dose range — i.e., the range that offers the greatest chance of locoregional control of breast cancer at the lowest cost in locoregional morbidity — appears to be 40 – 60 Gy in 2-Gy fractions [38]. These optimal biologically equivalent doses (BEDs) permit comparison of the total dose delivered in different fractionation schedules. It is now clear that the dose of postoperative radiation therapy in some trials was inadequate or excessive according to the current understanding of the dose – response relationships for minimal residual breast cancer. [40]

### 1.5 Monte Carlo Techniques in Radiotherapy:

Although interaction of photons and electrons in matter is well understood, in general it is impossible to develop an analytic expression to describe particle transport in a medium. This is because electrons can create both photons (e.g. as Bremsstrahlung) and secondary or knock out electrons ( $\delta$ -rays) and conversely, photons can produce both electrons and positrons. In addition, both electrons and photons scatter a great deal.

Figure 2 below demonstrates the interactions of a 10 MeV photon (dotted line) incident from the right on a slab of lead. A pair production event occurs and produces an electron (solid line) and a positron (long dashed line). The electron scatters many times and loses energy to low energy particles. The electron gives off a bremsstrahlung photon near the bottom of the figure. The positron also scatters many times and loses energy and then annihilates in flight (if it were at rest, the two 511 KeV photons would be given off at 180

degrees to each other). The 511-keV photon coming back towards the surface Compton scatters, creating another electron and scattering, apparently at 90 degrees. [11]

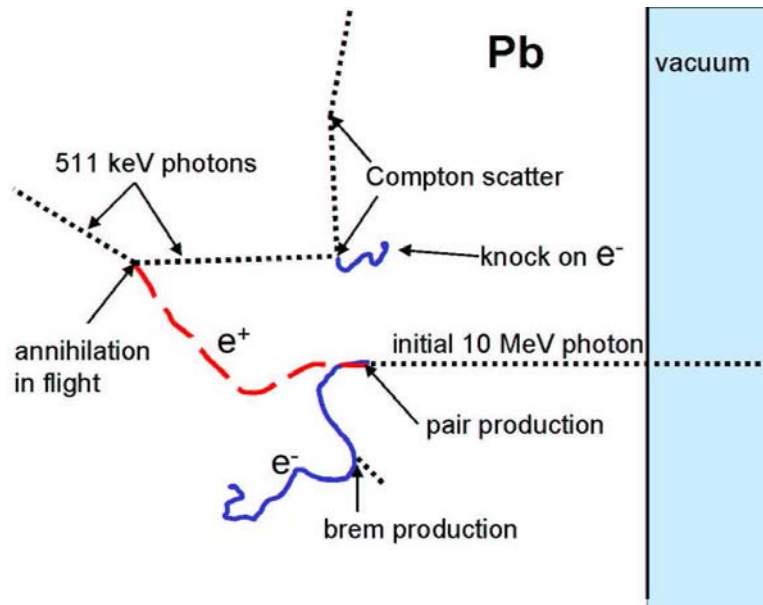


**Figure 2:** Interactions of a 10 MeV photon on a slab of lead

The scattering of electrons is strongly affected by changes in density and composition in the irradiated medium (patient) and the angular distributions are rarely known. Contemporary pencil beams cannot properly account for electron scatter. The underlying Fermi-Eyges model assumes that all heterogeneities are infinite in lateral extent. Three-dimensional implementations of pencil beam algorithms, of which Hogstrom Code is most widely used, often deviates from measurements by more than 10% for even relatively simple geometries. More complex pencil beam algorithms remove some of the consequences of infinite lateral extend of heterogeneities. Although more accurate results are achieved, significant approximations remain. [72]

The transport problem of particles in matter can be solved exactly, within the existing knowledge of the elementary collision processes, by the Monte Carlo (MC) techniques. A Monte Carlo method is defined by Halton (1970) as: representing the solution of a problem as a parameter of a hypothetical population, and using a random sequence of numbers to construct a sample of the population, for which the statistical estimates of the parameter can be obtained.

The MC method has long been recognized as a powerful technique for performing certain calculations, generally those too complicated for a more classical approach. Since the use

of high- speed computers became wide spread in the 1950s, a great deal of theoretical investigation has been undertaken and practical experience has been gained in MC approach.

MC simulation of particles transport in matter is a faithful simulation of physical reality: particles are "born" according to distribution describing the source, they travel certain distances, determined by a probability distribution depending on the total interaction cross-section, to the site of a collision and scatter into another energy and/or direction according to the corresponding differential cross-section.

The particle track can be broken up into individual segments, each of which can be considered to occur in a single material and region. As one crosses the geometrical boundary, one needs to change cross-sections if the material changes, and one has the choice of reselecting a new distance  $x$  to travel in the new medium, or of keeping track of how many mean free paths were traversed in the previous medium using the new cross-section. This choice comes about because once a particle has reached a given point the probability of interacting in the new medium is independent of how far it traveled in the previous medium. Quantities of interest can be calculated by averaging over a given set of MC particle "histories". [73, 74]

MC simulation of coupled photon-electron transport offers the physicist a powerful tool for improving the accuracy in most of the steps mentioned above. From the calibration standards to the solid-state dosimeter, MC calculations offer a means of:

- \* improved accuracy, especially where measurement is difficult or not possible,
- \* answering basic radiation physics questions for complex situations,
- \* establishing trustworthy benchmarks to compare with (e.g., dose distributions).

Implementing the MC method for the simulation of interactions of photons and electrons in matter has lead to the development of several general-purpose programs or codes (Berger and Seltzer, 1973; Halblieb and Mehlhorn, 1984; Breisemeister, 1993; Nelson et al., 1985; Baro et al., 1995; Salvat et al., 2003; Agostinelli et al., 2003; Giani et al., 1998). The basic ingredients of these codes are the probability distributions (differential cross-sections) of electron and photon interactions in various media and algorithms for the random sampling of these various competing process cross-sections for a suitably large number of initial "particle histories". With a sufficient number of initial particles followed (including all additional particles generated along the way) until the "end", the accumulated dose in a volume may be determined with an uncertainty of less than 1%. Photon interaction events are relatively separated in the medium compared to electron interactions and can,

therefore, be rigorously tracked by the MC code. In contrast, when a high-energy (5-30 MeV) electron loses 1 MeV of kinetic energy in water it will have on the order of 10,000 elastic scattering interactions in the medium. There are too many electron events to individually track high-energy electrons and their progeny from start to finish even with current computing power. However, the net accumulation of a sequence of multiple scattering events can be approximated by the multiple scattering models such as those of Molière (Bethe, 1953) or Goudsmit and Saunderson (1940). All the MC programs of interest to clinical dosimetry use a multiple-scattering "condensed history" algorithm to make the electron transport problem practical. MC for microdosimetry, on the other hand, tracks charged particles event by event. The most commonly distributed MC codes are:

ETRAN/ITS (Electron Transport/Integrated Tiger Series) (Berger and Seltzer, 1973; Halblieb and Mehlhorn, 1984)

EGS4 (Electron Gamma Shower, version 4) (Nelson et al., 1985)

EGSnrc (the National Research Council of Canada version of EGS) (Kawrakow and Rogers, 2000)

MCNP5 (MC for Neutrons and Photons, ver. 5) (Breisemeister, 1993)

PENELOPE (Baro et al., 1995)

GEANT4 (GEometry ANd Tracking 4) (Agostinelli et al., 2003; Giani et al., 1998)

These codes, especially the EGS4 and EGSnrc, have been extensively benchmarked with experimental data and, of course, to each other (Jenkins et al., 1988; Siebers et al., 1999; Jeraj et al., 1999; Ye et al., 2004; Sheikh-Bagheri et al., 2000). [75]

### **1.5.1 Why EGSnrc**

In medical physics, EGSnrc remains the most widely used general purpose Monte Carlo radiation transport package but a variety of other code systems are available. The PENELOPE code package has a detailed treatment of cross sections for low-energy transport and a flexible geometry package which allows simulation of accelerator beams (Baro et al 1995, Salvat et al 1996 Sempau et al 2001). The MCNP system is maintained by a large group at Los Alamos National Laboratory and has many applications outside medical physics because it was originally a neutron-photon transport code used for reactor calculations (Brown 2003). This code has a very powerful geometry package and has incorporated the ETRAN code system's physics for doing electron transport. The great flexibility of this code makes it run considerably slower than EGSnrc unless care is taken to adapt it to typical medical physics applications such as dose calculations in a voxelized phantom (DeMarco et al 1998). The GEANT4 code (Agostinelli et al 2003) is a general



purpose code developed for particle physics applications. It can simulate the transport of many particle types (neutrons, protons, pions, etc). GEANT4 has been used for various application in radiotherapy physics (Carrier et al 2004, 2006) and is the basis of the GATE simulation toolkit for nuclear medicine applications in PET and SPECT (Jan et al 2004). GEANT4 still demonstrates some problems when electron transport is involved and runs considerably slower than EGSnrc in these applications (Poon and Verhaegen 2005, Poon et al 2005) but the overall system is very powerful. [75]

### **1.5.2 Goal of MC in treatment planning**

The goal of MC in treatment planning is to be able to simulate and accurately calculate the dose distributions and monitor units (MU) for every field shape and SSD. This requires:

- Reliable reconstruction of full phase space of source
- Reliable positioning of external shielding including inserts suspended above the patient, generally on the downstream scraper bar of the applicator, and cut-outs placed directly on the patients.
- Reliable positioning of the patient CT-volume relative to the prescribed position and orientation of the treatment head, namely isocentre, position and rotation of the gantry, collimator and couch
- Reliable positioning of bolus, which may be a flat surface perpendicular to the beam direction, constant thickness or variable thickness to alter the therapeutic range and position.
- Accurate simulation of shielding, bolus, and patient, with shielding that need not conform to CT voxels.
- Isodose and point dose display with patient geometry, with provision for hard copy of display [75-78]

### **1.5.3 Clinical sites for which Monte Carlo may be useful**

The clinical treatments that will benefit most from improved dose calculation accuracy are those for which the improved accuracy makes possible better informed decisions about clinical plan optimization. These improved decisions will include how to deliver more doses to the tumor without compromising safety and better knowledge of dosimetric limits for normal tissues. Clinical sites which involve tissue inhomogeneities or interfaces between regions of different densities are likely to benefit, as are sites treated

with small fields, sharply varying intensity distributions, complex sets of beam modifiers or other complex treatment techniques which led to lateral electron disequilibrium or other effects which are typically only handled correctly by MC algorithms. Treatments in the head/neck and thorax (lung, breast/chest wall, etc.) are thus obvious candidates due to the significant inhomogeneities involved, but other treatment sites may also be important. [40]

### **1.5.4 Dose response evaluation**

Radiation therapy has long proved to kill or control the spread of tumor cells. Yet, there is always a risk of serious damage to normal tissues. The risk increases with radiation dose, as does the probability of tumor control. The magnitude of the effects of radiation on both tumor cells and organs at risk governs the effect of the radiotherapy treatment i.e. its success in tumor control and the prevention of normal tissue complications.

Great efforts are spent to make it possible to choose the best treatment plan from those that are under consideration, knowing their probable clinical outcome, namely the tumor control probability (TCP) and normal tissue complication probability (NTCP). A set of mathematical models, known as radiobiological Dose-Response models, have been developed, to model the biological effects and complications that arise following irradiation. Amongst these models are the Relative Seriality model (Withers et al. 1988, Kallman et al. 1992b, Lind et al. 1999), the LKB model (Lyman 1985, Kutcher and Burman 1989), and the Parallel model (Boersma et al. 1995).

## **1.6 Objectives of the work**

There are three objectives of this work:

- The first objective is to simulate ELEKTA SL18 electron beams for all the provided energies; 4, 6, 8, 10, 12, 15 and 18 MeV and different field sizes; 6X6, 10X10, 14X14 and 20X20 cm<sup>2</sup>.
- The second objective is to investigate the possible sources of error in electron beam simulations, which can be used by other researchers using Monte Carlo electron beams.
- The third objective is to evaluate electron postmastectomy radiotherapy for different energies, fields and angles of irradiation. To do so, several steps had to be followed.

- Re-write a code for XSTING, which is designed for radiosurgery applications to accept input dose files produced by DOSXYZnrc codes and generate the corresponding isodose distributions and dose volume histograms.
- Test the new XSTING code for MC applications and compare the output isodose lines with the benchmarked DOSXYZ\_show.
- Test the accuracy of the dose-volume histograms DVH, produced by XSTING.
- Apply XSTING for evaluating postmastectomy radiotherapy using electron beams.
- Use the generated DVHs as input parameters in the PatientTherapyDataForm; which will be loaded to DORES to produce the different dose response parameters for the evaluation.

## 1.7 Description of the thesis

This thesis is written in the general format, which consists of five chapters; Introduction, Materials and Methods, Results, Discussion and Conclusions and Recommendations. Each chapter is further divided into units and sub-units.

The **Introduction chapter**, Chapter One reflects the bibliography and previous works. It explains radiotherapy in general, conformal radiotherapy and focuses on electron beam radiotherapy. Some physics of electron beams is then explained in details. This is followed by indepth discussion of postmastectomy radiotherapy (PMRT); indications, challenges and post-treatment complications and the main PMRT techniques used in different centres. Finally, Monte Carlo techniques and their applications are briefly explained.

In Chapter two, the **Materials and Methods** the design of the linear accelerator ELEKTA SL18 is explained. This is followed by brief description of the different software used; including EGSnrc, XSTING and DORES, their functionalities and their applications as well as the applications of the different software to achieve the desired goals.

In the Chapter Three, **Results**, the verification the input values that were used for verification and the verification graphs are displayed. Graphs illustrating the effect of different sources of systematic errors are then shown. This is followed by isodose and DVH verification results for XSTING and then the isodose and DVHs for different energies fields and angles of electron postmastectomy radiotherapy. The DVHs are then exported to DORES and NTCP results for the lung for the different treatments are studied.

These results are discussed in turn in depth in the Chapter Four, **Discussion**. The explanation of the effects of slight alterations of the beam and phantom parameters as well as the Linac configuration on the accuracy of the simulations is given. The physics behind the related systematic errors resulting from such alterations is briefly explained. This is followed by the analysis of the DVHs generated for the postmastectomy study and evaluation of the outcome based on comparison with some published parameters for pulmonary and cardiac complications, such as V20 and V35 respectively. Finally the different treatment electron postmastectomy scenarios are compared in the light of the NTCP values obtained from DORES. At the moment, it is not possible to study the NTCP of the lung injury with DORES so only pneumonitis is investigated.

The final conclusions and remarks based on the discussed results, together with some recommendations for future work at the Monte Carlo laboratory are summarized in Chapter Five **Conclusions and Recommendations**.

## **CHAPTER TWO: MATERIALS AND METHODS**

## 2.1 Materials:

### 2.1.1 ELEKTA SL18

The SL 18 linear accelerator has a dual mode operation; photons, with nominal energies 6 and 15 MV, and electrons with seven different nominal energies of: 4, 6, 8, 10, 12, 15, and 18 MeV. In electron mode, electrons emerge through a thin exit window made of Nickel. The beam then passes through dual scattering foils that consist of a high-z (atomic number) material to broaden the beam into a Gaussian profile and a lower-z Gaussian-shaped foil that minimally scatters the electrons at the tail of the profile and maximally scatters electrons near the centre to flatten the field in the area of interest with a suitably sharp fall-off at the field edges. A tungsten primary collimator separates these foils. The monitor ionization chamber of the SL18, which controls the beam intensity and uniformity, is made in form of thin layers of a Mylar separated by air gaps. This is embedded in an Aluminum disc. The light localizing system consists of the light source and a thin mirror and is used for field size definition within the patients. Beam shaping is performed by a set of jaws made from tungsten and lead, with Nickel and iron added to the trimmer plates. This is followed by different electron applicators in the form of sets of diaphragms or scrapers with a thick base that is attached to the treatment head. Applicators are demountable devices attached to an accessory mount and provide collimation at about 5cm from the patient surface. In the University Hospital of Larissa there are 4 different applicators producing different field sizes on the desirable plane 6x6, 10x10, 14x14 and 20x20 cm<sup>2</sup>. The fields can be further shaped by means of mountable Cerrobend cutouts.

In the photon mode, instead of passing through the Nickel exit window, electrons strike on a target made up from Tungsten and Rhenium, creating a beam of photons. These then pass through the conical collimator to the flattening filter, which is made from stainless steel. The flattening filter selectively absorbs the photons through beam's profile (through a plane perpendicular to the central axis of the beam), creating a beam with uniform intensity across the field. The beam then passes through the monitor ionization chamber and then the jaws. Unlike electron mode no applicators are used. The figure below shows a simple description of SL18 Linac, as provided in ELEKTA manual. The actual design cannot be displayed due to the confidentiality.

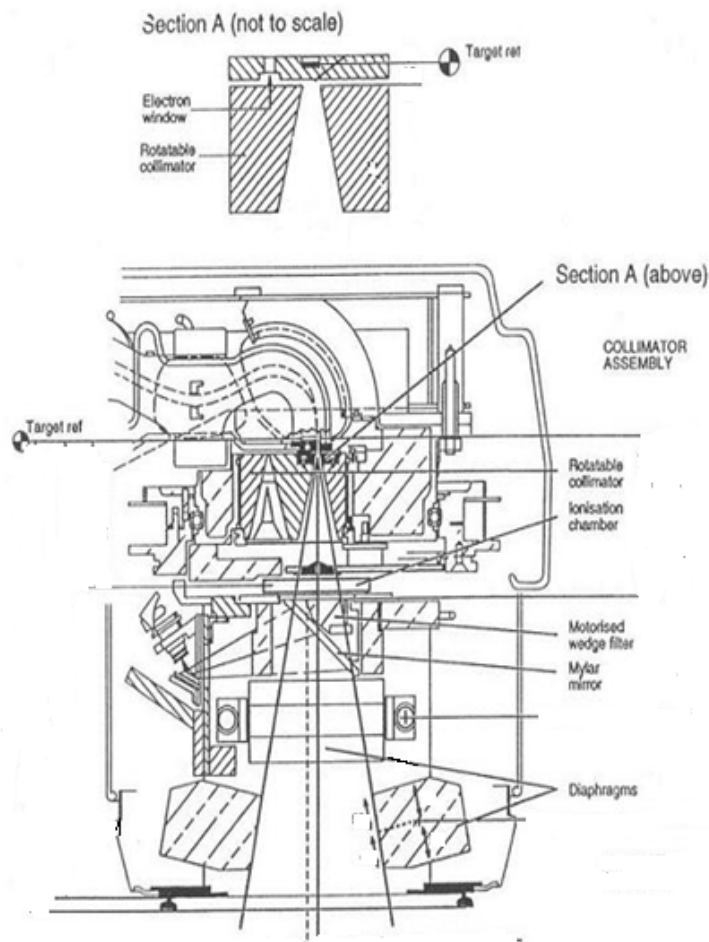


**Figure 3:** ELEKTA linear accelerator (dimensions and materials not displayed for confidentiality reasons) [79]

### 2.1.2 EGSnrc

The EGSnrc system is a set of subroutines that implement the modeling of the various interaction processes and the simulation of electron and photon transport. For a complete application the user must write a "user code". A typical user code consists of a main program, a scoring routine (called ausgab) and two subroutines that provide geometrical information to EGSnrc via a well-defined interface. EGSnrc user codes have been traditionally written in Mortran, a Fortran-like language that is translated into Fortran by the Mortran pre-processor provided with the system. The power of the EGSnrc system is due to the fact that user codes can be tailor-made to calculate exactly what the user wants

and needs, possibly implementing variance reduction techniques that speed up the simulation significantly.

The main features of the EGSnrc Code System, including statements about the Physics that has been put into it and what can be realistically simulated can be summarized as follows:

- i ) The radiation transport of electrons (+ or -) or photons can be simulated in any element, compound, or mixture. The data preparation package, PEGS4, creates data to be used by EGSnrc, using cross section tables for elements 1 through 100. In addition, there are other data files that must be read in to implement many of the new options.
- ii ) Both photons and charged particles are transported in steps of random length rather than in discrete steps.
- iii ) The dynamic range of charged particle kinetic energies goes from a few tens of KeV up to a few hundred GeV.
- iv ) The dynamic range of photon energies lies between 1 KeV and several hundred GeV.

The EGSnrc Code System takes the following physics processes into account:

- Bremsstrahlung production using either Bethe-Heitler cross-sections or the NIST cross-sections.
- Positron annihilation in flight and at rest (the annihilation quanta are followed to completion).
- Multiple scattering of charged particles by coulomb scattering from nuclei is handled using a new multiple scattering theory, which overcomes the shortcomings of Moliere multiple scattering theory. It allows for steps of any size and moves correctly from a single scattering model for short steps to an accurate multiple scattering model for large steps. The user has the option to treat the scattering interactions based on Rutherford scattering theory, as well as to choose whether relativistic theory and spin effects will be taken into account.
- Møller ( $e^-e^-$ ) and Bhabha ( $e^+e^-$ ) scattering. Exact rather than asymptotic formulae are used.
- Continuous energy loss applied to charged particle tracks between discrete interactions.
- Total restricted charged particle stopping power consists of soft bremsstrahlung and collision loss terms.
- Collision loss determined by the restricted Bethe-Bloch stopping power with the Sternheimer treatment of the density effect in the general case but with provision of



using an arbitrary density effect correction and data supplied to use the density effect recommended by the ICRU in Report 37.

- Pair production.
- Compton scattering, either Klein-Nishina or bound Compton.
- Coherent (Rayleigh) scattering can be included by means of an option.
- Photoelectric effect.
- Relaxation of excited atoms after vacancies are created (e.g., after photoelectric or Compton scattering events) to create fluorescent photons (K, L, M shells) and Auger and Coster-Kronig electrons may be produced and tracked if requested. [73]

**The following general-purpose Monte Carlo codes of EGSnrc were used in the work:**

**EGSnrcMP:** (the multi-platform environment for running the EGSnrc Monte Carlo code system for simulating the transport of photons and electrons) is the latest version of the popular EGS code system and features much improved transport physics plus the ability to work on all major operating systems. It also allows more flexibility to the original Unix script. Overview of the changes from EGSnrc is found in:

<http://www.irs.inms.nrc.ca/EGSnrc/pirs877>

**BEAMnrc:** uses the EGSnrc Monte Carlo system of radiation transport. The code models the therapy source with the Z-axis taken as the beam axis and usually the origin is defined as the centre of the beam as it exits from the accelerator vacuum. The model consists of a series of component modules CMs each of which is contained between two planes which are perpendicular to the z-axis and which cannot over-lap. [80]

**User defined parameters for BEAMnrc code based simulation:**

**Geometrical details of the accelerator's components:** The accelerator components are defined as a set of component modules. A component module can be considered as a block that has a front surface and a back surface. An accelerator is built with many such blocks. Each one has different symmetry (cylindrical or square) and features, depending on the geometry and the usage of the specific structure it was initially designed to simulate. Very often there is a gap between two blocks. This gap is automatically filled with air, which is consistent with the case of a real accelerator.

**Main input parameters:**

**IWATCH** controls output to the screen (interactive run) or to the .egslog file (batch run) during beam execution. The possible settings are:

= 0 (default). On completion of each batch, outputs information about the batch (e.g. elapsed time, CPU time, elapsed/CPU time, random number used to begin batch, # of random seeds used in the batch, total number of histories run up to and including the current batch, the total number of particles scored in the first phase space file)

= 1 Outputs batch information plus, after every particle interaction, outputs complete information about the particle(s) involved (e.g. interaction type, particle type, position of particle on stack, particle energy, X-Y-Z position of particle, U-V-W direction cosines, LATCH value of particle, region # of particle); also informs user when a particle is being discarded, when a particle is passing from one CM to another.

= 2 Similar to 1 only complete particle information is output at every step; also outputs total dose in a region whenever energy is deposited there.

= 3 Similar to 2 only particle and dose information are output whenever dose is deposited.

= 4 Outputs same information as 0 plus .egsgph and egsgeom files for graphical representation of the accelerator and particle paths using EGS\_Windows.

**Random Number Generators (RNG)** EGSnrc is supplied with two random number generators, RANLUX and RANMAR. RANMAR is the generator used with EGS4 in the UNIX distributions. The RANLUX generator is the default generator in EGSnrc and comes with a variety of "luxury levels", from 0 to 4, and a period of greater than  $10^{23}$ . It has been found that it gives incorrect answers in some practical EGSnrc calculations with luxury level 0, but when using luxury level 1 or higher this problem does not exist. The RANLUX has been utilized as the default random number generator because it allows explicit testing with higher quality sequences if there are ever any doubts.

Both random number generators offer several important features. First, they are completely portable, producing the same sequences on different machines, although RANMAR occasionally gets slightly out of sequence, something that does not happen with the use of the RANLUX generator. An even more important feature is that either generator can be initialized and guaranteed to produce a random number sequence that is independent from other sequences. This is very useful for doing runs in parallel on multiple machines. To implement one generator or the other requires commenting out (in the configuration file) the two files associated with the generator, which is not required. The relevant files are:

- ranlux.macros or ranmar.macros
- ranlux.mortran or ranmar.mortran.

**Run option:** This parameter allows the user to choose if the simulation is run for the first time or if it is continuing from an interrupted run.

**Latch option:** Each particle in a simulation can be associated to the LATCH variable. This is a 32-bit variable used to track the particle's history. In the BEAM\_GUI, there is an opportunity to define a mapping from geometrical regions to bits using the "Associate with LATCH" option. Thus, it is possible to correspond a bit to one or more geometrical regions. The user has several options about how to set the LATCH\_OPTION:

- Non-Inherited: the secondary particles do not inherit LATCH values from primaries that created them.
- Inherited-set by passage: where LATCH values are passed to secondary particles from the particles that created them.
- Inherited-set by interactions: where in the case of photons, the bits (1-23) record the regions in which the particles have interacted, rather than simply where they have been.

By using LATCH to trace a particle's history the user is being given the ability to break down the dose, in any dose zone, to its components. The dose components can be selected in two ways:

1. Dose from contaminant particles
2. Dose including only or excluding only contributions from particles with a certain LATCH bit, specified by the user.

**Score ZLAST:** ZLAST is, for the photons, the z-coordinate of their last interaction, and for electrons the z-position where the electron or its ancestor was set in motion by a photon. It is important to note that the type of file created to tabulate the particles' parameters depends on whether or not the user selects to score ZLAST (MODE0 or MODE2).

**Variance reduction techniques:** In mathematics, more specifically in the theory of Monte Carlo methods, variance reduction is a procedure used to increase the precision of the estimates that can be obtained for a given number of iterations. Every output random variable from the simulation is associated with a variance which limits the precision of the simulation results. In order to make a simulation statistically efficient, i.e., to obtain a greater precision and smaller confidence intervals for the output random variable of interest, variance reduction techniques can be used.

In general, (i) reducing the variance or (ii) reducing the CPU time per particle simulated can increase the efficiency of MC simulations. Techniques leading to efficiency increase,

although not always associated with variance reduction, are called variance reduction techniques.

Decrease of the variance per particle simulated can be achieved, for instance, by a uniform distribution of the primary interaction sites of the incoming photon beam or by increasing the importance of particles with a large influence on the dose. Reduction of the CPU time per particle history is possible by re-using certain quantities, particle splitting, interaction forcing, etc

#### **Input parameters for the variance reduction techniques:**

##### a) Range Rejection

Range rejection is used to save computing time during simulations. The method is based on calculating the range of a charged particle and terminating its history (depositing all of its energy at that point) if it cannot leave the current region or reach the bottom of the accelerator with energy greater than a certain threshold value. Global ECUT and PCUT define the choice of energy threshold below which the histories of electrons and photons are terminated. AE and AP define the threshold for which the product knock-on electrons and Bremsstrahlung photons are terminated

##### b) Photon Forcing

BEAMnrc offers an option whereby the user can force photons to interact in specified Component Modules within a simulation. This option is useful for improving statistics of scattered photons when photon interactions are sparse, as in thin slabs of material or in materials with low density. One of the main purposes of implementing this option was to study the generation of contaminant electrons in a photon beam.

Briefly, a photon forced to interact in a CM is "split" into a scattered photon whose weight is equal to the probability of interaction and an un-scattered photon carrying the remaining weight. The un-scattered photon proceeds as if an interaction did not take place, and it cannot be forced to interact any more within the specified forcing zone, which can consist of one or several component modules. However, once the un-scattered photon gets out of the forcing zone, it may interact again depending on the sampled path length. The scattered photon can be forced again in the forcing zone depending on how many interactions are allowed to be forced.

### c) Bremsstrahlung photon splitting and Russian Roulette

Bremsstrahlung photon splitting offers the user another variance reduction technique, which improves the statistics of bremsstrahlung photons resulting from electron interactions. BEAMnrc offers two bremsstrahlung splitting techniques, uniform bremsstrahlung splitting (UBS) and selective bremsstrahlung splitting (SBS). Both of these splitting techniques have been optimized in BEAMnrc with the addition of the Russian Roulette feature.

- Uniform Bremsstrahlung Splitting

The input variables associated with uniform bremsstrahlung splitting (UBS) are the IBRSPL, which should be set to 1 for uniform bremsstrahlung splitting, and the NBR SPL, which is the splitting number. It can be also applied to higher-order bremsstrahlung and annihilation photons if Russian Roulette is turned on. Each bremsstrahlung event produces

NBR SPL photons, each having a weight equal to  $\frac{1}{NBR SPL}$  times the weight of the electron

that underwent the bremsstrahlung event. The energy and direction of each photon are sampled individually according to the relevant probability distributions. The energy of the primary electron is decremented by the energy of just one of the photons. This must be done in order to preserve the effects on energy straggling, but this means that energy is not conserved on a given history (the energy would have to be decremented by the average energy of the photons created) but rather it is conserved “on average” over many histories. The splitting number, NBR SPL, is not applied to higher-order bremsstrahlung and annihilation photons unless Russian Roulette is used. This prevents wasting simulation time by tracking many higher-order photons of vanishing weight.

- Selective Bremsstrahlung Splitting

Selective bremsstrahlung splitting (SBS) is a more efficient method of bremsstrahlung splitting. Input variables associated with selective bremsstrahlung splitting (SBS) are the IBRSPL which is set to 29 for selective bremsstrahlung splitting, the NBR SPL which is the Maximum splitting number, the NMIN which is the minimum splitting number, as well as, the splitting number to be used for higher-order bremsstrahlung and annihilation photons if Russian Roulette is on. Another parameter is the FS, which is defined as the biggest side of the treatment field plus 10 cm. In conjunction with SSD, this is used to define the relevant angle for the selective bremsstrahlung splitting routine. Actually, the radius that gives the same area as  $FS^2$  is used. The SSD value is the distance from the beginning of the

bremssstrahlung target at which the above FS is defined. The approach made is that all Bremsstrahlung photons are created on the front surface.

In contrast to UBS, in which the bremsstrahlung splitting number is fixed, SBS uses a varying bremsstrahlung splitting number. At the beginning of a simulation, an array of probabilities that a bremsstrahlung photon will be emitted into the treatment field (defined by FS and SSD) is calculated for different electron directions and energies. This array is used to determine the variable splitting number, NBR, at the time of each bremsstrahlung event, subject to the restriction:  $NMIN < NBR < NBR SPL$ . The split photons are then given a weight equal to  $\frac{1}{NBR}$  times the weight of the electron that underwent the bremsstrahlung event. In SBS, higher-order bremsstrahlung and annihilation photons are split with a fixed splitting number defined by NMIN provided that Russian Roulette is on. Otherwise, higher-order bremsstrahlung and annihilation photons are not split. This prevents long simulation times tracking higher-order photons of diminishing weight.

- Charged Particle Russian Roulette:

Following the whole track of the secondary charged particles created by the “split” photons increases the CPU time required for simulations. If the primary interest is in secondary electrons or their effects (*e.g.* dose deposition), the extra computing time is obviously acceptable. However, as is often the case, the main interest is in the bremsstrahlung photons themselves, one can reduce the CPU time while still preserving the variance reduction advantages of bremsstrahlung splitting by using a Russian Roulette technique with any charged particles generated by the split photons.

If the Russian Roulette is turned on then the higher-order bremsstrahlung and annihilation photons are split with splitting number NBR SPL in UBS and NMIN in SBS. Russian Roulette is implemented by giving secondary charged particles resulting from split photons a survival threshold. The survival threshold is always the inverse of the photon splitting number. Thus,

in the case of UBS, the threshold is fixed and is equal to  $\frac{1}{NBR SPL}$ , while in the case of SBS,

the survival threshold is  $\frac{1}{NBR}$  where NBR is the variable splitting number. Then a random

number is chosen for each charged particle. If the random number is lower than the survival threshold, the charged particle survives, and its weight is increased by a factor of NBR SPL (for UBS) or NBR (for SBS). Otherwise, the charged particle is eliminated.

Secondary charged particles subjected for Russian Roulette are electrons resulting from Compton events and photoelectric events and electrons and positrons resulting from pair production. If Russian Roulette is turned on, then the higher-order bremsstrahlung and annihilation photons are also split. This is due to the fact that any charged particle surviving Russian Roulette has a weight higher than the photon that created it. If radiative products from this surviving charged particle are not split, then their high weight may interfere with the statistics of the original split bremsstrahlung photons. Also, splitting of higher-order bremsstrahlung and annihilation photons does not greatly increase computing time when Russian Roulette is on because most of the secondary charged particles have been eliminated.

**Source Routines:** In general, the incident particles move in the direction of the z-axis. With the exception of ISOURC=3 (internal isotropic source), =10 and 13 (x-ray tube sources) or =21 and 31 (phase space inputs), the particles start being transported on the Z\_min\_CM(1) plane. Conceptually, some of them originate at a point outside the accelerator model and are essentially transported through vacuum to the accelerator which starts at the Z\_min\_CM(1) plane. One of the major features of BEAMnrc is that a phase space file can be used as a source file between any two CMs in the accelerator.

. This feature also allows the accelerator simulation to be broken up into components. For example, one might simulate the fixed components at the top of an accelerator and then feed the phase space file into a variety of calculations with different jaw or applicator settings.

The following subsections describe the source routines available in BEAMnrc.

ISOURC=0 Parallel Circular Beam

ISOURC=1 Isotropic Point Source on Z-axis

ISOURC=3 Interior Isotropic Cylindrical Source

ISOURC=5 NRC Swept Beam

ISOURC=6 Parallel Rectangular Beam

ISOURC=7 Scanning Beam (sawtooth)

ISOURC=8 Scanning Point Source for MM50

ISOURC=9 Discrete Point Source for MM50

ISOURC=10 Parallel Circular Beam Incident from Side

ISOURC=13 Parallel Rectangular Beam Incident from Side

ISOURC=15 NRC Swept Beam with Radial Intensity Distribution and Radial Divergence

ISOURC=19 Circular Beam with 2-D Gaussian X-Y Distribution, Parallel or with Radial Divergence

ISOURC=21 Phase Space Source

ISOURC=31 Beam characterization Model

**Parameters of the scoring plane** The particles proceed through a simulation and the created particles from the interactions that take place in the various component modules (CM) or the air inside the head of the linear accelerator are scored at user-defined planes. A scoring plane is always located at the back side of a CM. The user must:

- i ) Set the number of fluence scoring planes.
- ii ) Specify the CM at the lower part of which, each plane will be scored.
- iii ) Specify the number and the width of the scoring zones within the total scoring plane and whether these zones will be square or annular.

**The processing of the number of simulated events (histories) from the irradiation source and maximum CPU allowed time:** The user should also choose the number of particles to be simulated and the maximum CPU time that is needed to run this number of events. Increasing the number of histories decreases the uncertainty but increases the time required and the size of output files.

**EGSnrc parameters: These are the parameters governing the particle transport and the probability of the various interactions. They include:**

**Step size:** At any instant during a photon history, one or more particles have their position, direction and energy stored on a stack of variables. The transport of a particle to its next position is called a step, after which the variables on the stack associated with that particle are updated.

During a photon step, the following points must be considered:

Distance to the next interaction In a photon step, the particle is transported in its current direction for a random distance. The probability of selecting a particular distance is determined by the mean free path corresponding to: (a) the current photon energy and (b) the medium in which the photon currently resides.

Type of interaction After a step is completed; a decision is made as to which type of interaction takes place at that position. Interaction type is chosen randomly, with probabilities corresponding to photon energy and medium.

New angle and energy When the type of interaction has been chosen the resultant angle and energy of the original particle are chosen. These parameters are determined from cross section tables, again taking into account energy and medium.

Secondary particles As a result of some interactions, new particles are created and/or set in motion. Position, direction and energy of these particles are then added to the data stack.



**Energy loss/step size:** This is the maximum fractional energy loss per electron step.

**XImax:** This is the maximum first multiple elastic scattering moment per electron step. It is equal to roughly half the average multiple scattering angles squared. Make sure you do not set

**Boundary crossing algorithm (BCA):** This controls the algorithm used to transport electrons across region boundaries. There are two possible settings of Boundary crossing algorithm: EXACT and PRESTA-I. The EXACT boundary-crossing algorithm was introduced in EGSnrc to eliminate a known fluence singularity caused by forcing a multiple scattering event at a boundary. In the EXACT case, electrons are transported in single elastic scattering mode as soon as they are within a distance from the boundary given by the EGSnrc input Skin depth for BCA. If the PRESTA-I BCA is used boundary crossing is carried out in a manner similar to EGS4/PRESTA. Specifically, the lateral correlation algorithm is turned off if the perpendicular distance from the electron to the boundary is less than Skin depth for BCA and then, once the electron reaches the boundary, a multiple scattering event is forced.

**Skin depth for BCA:** If Boundary crossing algorithm= PRESTA-I, then Skin depth for BCA is the perpendicular distance (in elastic mean free paths) from the boundary at which lateral path-length corrections are turned off and the particle is transported in a straight line until it reaches the boundary. By default the distance at which to switch off lateral corrections is a fixed value calculated by EGSnrc to be the same as that used in the original implementation of PRESTA in EGS4 and depends on the value of ECUT.

If Boundary crossing algorithm= EXACT, then Skin depth for BCA determines the perpendicular distance (in elastic mean free paths) to the region boundary at which electron transport will go into single elastic scattering mode.

**Electron-step algorithm:** This input determines the algorithm used to calculate lateral and longitudinal corrections to account for elastic scattering in a condensed history electron step. There are 2 possible settings: PRESTA-II (the default) and PRESTA-I. PRESTA-II is the new, more accurate, algorithm developed for use with EGSnrc. PRESTA-I is the original PRESTA algorithm with some modifications.

**Spin effects:** If Spin effects= on (the default), then elastic scattering cross-sections that take into account relativistic spin effects are used in electron transport. If Spin effects= off, then screened Rutherford cross-sections are used for elastic scattering.

With Spin effects= on results are more accurate and it is ABSOLUTELY necessary for good backscatter calculations.

**Electron impact ionization:** This input determines what, if any, theory is used to simulate electron impact ionization. The possible values are "off" (the default), "on", "Casnati", "Kolbenstvedt", and "Gryzinski". When "on" is selected, Kawrakow's electron impact ionization theory is used. For the other selections, the theory associated with the name given is used. Since the details of electron impact ionization are only relevant at KeV X-Ray energies, the default "off" setting should be used in most BEAMnrc simulations.

**Brems angular sampling:** This input determines the type of angular sampling that is done when a bremsstrahlung photon is created. If Bremsstrahlung angular sampling= Simple (the default) then bremsstrahlung angles are sampled using only the leading term of modified equation 2BS of Koch and Motz. If Brems angular sampling= KM, then the bremsstrahlung angles are sampled using the entire modified equation.

**Brems cross sections:** This input determines the differential cross-section used for bremsstrahlung interactions. If Brems cross-sections= BH (the default), then Bethe-Heitler cross-sections (Coulomb corrected above 50 MeV) are used. If

Brems cross sections= NIST, then differential cross-sections from the NIST bremsstrahlung cross-section data base are used.

**Bound Compton scattering:** The Bound Compton scattering input is used to determine whether binding effects and Doppler broadening are simulated in Compton (incoherent) scattering events or not. If this input is set to Off (the default), then the Klein-Nishina formula is used to determine differential cross-sections for Compton scattering.

If Bound Compton scattering= On, then the original Klein-Nishina formula is augmented with the impulse approximation to simulate binding effects and Doppler broadening. Simulation of binding effects and Doppler broadening takes extra time and is only important below 1 MeV and/or if Rayleigh scattering is being simulated.

**Pair angular sampling:** This input determines the method used to sample the positron/electron emission angles (relative to the incoming photon) in a pair production event. There are three possible settings of this input: Off, Simple and KM.

**Photoelectron angular sampling:** The Photoelectron angular sampling input determines the sampling method used by EGSnrc to determine the angle of emission of photoelectrons. If Photoelectron angular sampling= off (the default), then photoelectrons inherit the direction of the incident photon.

If Photoelectron angular sampling= On, then Sauter's formula is used to determine the angle of the photoelectron.

**Rayleigh scattering:** This input determines whether Rayleigh (coherent) scattering is simulated or not. If Rayleigh scattering= on, then Rayleigh events are simulated using the

total coherent cross-sections from Storm and Israel and atomic form factors from Hubbell and Øverbø. If Rayleigh scattering= Off, then Rayleigh events are not simulated. Rayleigh scattering is only recommended for low energy ( $< 1$  MeV) simulations.

Atomic Relaxations: This input determines whether or not the relaxation of atoms to their ground state after Compton and photoelectric events is simulated. If Atomic Relaxations= On, then relaxation after Compton and photoelectric events is simulated via the emission of any combination of K-, L-, M- and N-shell fluorescent photons, Auger electrons and Coster-Kronig electrons. If Atomic Relaxations= off, then atomic relaxations are not simulated. In this case, when there is a photoelectric event, EGSnrc transfers all of the photon energy to the photoelectron.

Atomic Relaxations= on is only recommended for low energy applications.

Bound Compton, photoelectric angular sampling, Rayleigh scattering and atomic relaxations can be turned on/off in selected regions

Photon cross sections: This selects the photon interaction cross-sections to use in the simulation. Cross-sections included with the BEAMnrc/DOSXYZnrc distribution are: "Storm-Israel", "epdl" and "xcom". The Storm-Israel cross-sections are the standard PEGS4 cross-sections. The "epdl" setting will use cross-sections from the evaluated photon data library (EPDL) from Lawrence Livermore. The "xcom" setting will use the XCOM photon cross-sections from Burger and Hubbell.

### **Output Phase space files**

Phase space files: The information concerning all the particles crossing a scoring plane is stored in the phase space files (.egsphsp#). A phase space file contains all the data related to position, direction, charge and interactions of every particle. Separate files are created to give the output of each scoring plane in a simulated accelerator. The input parameter IO\_OPT controls whether phase space files are created for a particular scoring plane.

The information recorded in a phase space file for every particle is (in order): LATCH, E, X, Y, U, V, WT, and (ZLAST) where:

- LATCH contains the particle charge IQ, the number of times the particle has crossed the scoring plane NPASS, and information which allows the particle's history to be traced.
- E is the particle's total energy (kinetic and rest mass, single precision).
- X and Y are the particle X-position and Y-position, respectively (in cm).
- U is the X-direction cosine and V is the Y-direction cosine.
- WT is the particle's weight; WT also carries the sign of W, the Z-direction cosine.

- ZLAST is the Z-position of the last interaction for photons and is the Z-position where an electron or its ancestor was set in motion by a photon. [80]

These files, which represent the electron beams emerging from the Linac, are used as the input source in the phantom simulation using DOSXYZnrc, below

**DOSXYZnrc:** is a general-purpose Monte Carlo EGSnrc user-code for 3-dimensional absorbed dose calculations. EGSnrc/DOSXYZnrc simulates the transport of photons and electrons in a Cartesian volume and scores the energy deposition in the designated voxels. The geometry is a rectilinear volume with the X-Y plane on the page, X to the right, Y down the page and the Z-axis into the page. Voxel dimensions are completely variable in all three directions. Every voxel (volume element) can have different materials and/or varying densities (for use with CT data). [81]

A variety of beams may be incident on the phantom, including full phase-space files from BEAMnrc. Any of the available beams can be incident on this CT phantom. The code includes a restart facility and can be run on parallel computing platforms. The DOSXYZnrc code, like the BEAMnrc system, is written for a pre-processor of Fortran77 called MORTRAN.

The statistical analysis in the DOSXYZ code is done using a standard batching technique. Starting with DOSXYZnrc the statistics on the doses are determined by grouping scored quantities (i.e., energy deposited) on a history-by-history basis and then determining the uncertainties. For most sources, this simply means grouping quantities by incident particle. However, for phase space sources, where more than one incident particle may be traced back to a single primary history, quantities are grouped by primary history. It is worth noting that the method used takes into account the latent variance in any phase space file being used as a source (i.e., the uncertainty introduced by the statistical variations in the phase space file). Hence, the uncertainty cannot be reduced in any dose calculation below that level by recycling the data a large number of times.

#### DOSXYZnrc user-defined parameters:

Similar to BEAMnrc the user defines some input parameters and specifies the EGSnrc parameters defining the physical interactions of the photons or electrons. The latter are not changed. The DOSXYZnrc-specific parameters are those describing the phantom and the source of radiation. The phantom can be defined using non-CT or CT data. When defined using non-CT, the phantom is a rectilinear volume with a right-handed coordinate system: The X-Y plane on the page, X to the right, Y down and the Z-axis into the page. It consists of a number of volume elements called voxels, with each one having different dimensions, material and/or density. The construction of this structure demands that the user:

- a) Define the number and volume of voxels in all three axes. Voxels in each axis are defined separately either individually or in groups. In every direction, the user selects the number of groups and then, starting from the minimum boundary (in cm), defines the width (cm) and the number of elements included in each group. This procedure is repeated for all three axes. The number and volume of the voxels depend on the areas where the user is most interested in scoring the dose and is frequently a compromise between accuracy, statistical error and computing time. For example, smaller voxel size was chosen for the areas of abrupt changes such as the field edges.
- b) Define the number of media that will be used in the simulation, including the material for the region surrounding the phantom. It is possible to select a different material for every group of voxels or for individual voxels by calling the number of the voxel and declaring the material or density needed. This is helpful for phantoms that consist of various materials or for the insertion of an inhomogeneity inside the phantom.
- c) Define the number of voxels for which to score the dose. Each voxel has a "number identity" which corresponds to the position it holds in the group. For example, a voxel in the X-axis with 1cm width which is placed after 10 voxels with 0.5cm width will correspond to the number "11". Selecting one or more groups of voxels for which we score the dose rather than scoring for all the voxels helps the user save valuable computing time.

When defined from CT data, CTCREATE, described below, should be used to create an egs.phant file from the DICOM, or other sorts of patients' information.

Charged particles, photons, or all particles from the source can be used as incident particles. There are different source-types in DOSXYZnrc. These include:

Isource = 0: Parallel Rectangular Beam Incident from Front  
 Isource = 1: Parallel Rectangular Beam Incident from Any Direction  
 Isource = 2: Phase-Space Source Incident from Any Direction DBS Inputs  
 Isource = 3: Point Source Rectangular Beam Incident from Front  
 Isource = 4: Beam Characterization Model Incident from Any Direction  
 Isource = 6: Uniform Isotropically Radiating Parallelepiped within DOSXYZnrc Volume  
 Isource = 7: Parallel Rectangular Beam Incident from Multiple Directions  
 Isource = 8: Phase-Space Source Incident from Multiple Directions  
 Isource = 9: BEAM Treatment Head Simulation Incident from Any Direction [81]

For large and/or complicated accelerators, the input required for BEAMnrc can lead to files that are large and confusing to the user. Similarly the inputs for DOSXYZnrc can be complex, especially for beams coming from arbitrary directions. The **BEAMnrc and DOSXYZnrc GUIs** were created to aid the user in both creating and editing these files by providing a label and a text box or option menu for each parameter, with a detailed explanation available in a help window. When the accelerator components and input parameters have been defined, the GUIs write the files required to run the BEAMnrc or DOSXYZnrc code. The GUIs in BEAMnrc and DOSXYZnrc makes it easy for the user to use these codes without any or limited knowledge of programming. [82]

**STATDOSE:** The STATDOSE is an interactive computer program for 3-dimensional dose analysis and plotting 1-dimensional dose distributions using the *xvgr/xmgr*-plotting package. 3D dose data such as that generated using the EGS4 user-code DOSXYZ, developed at NRCC for the OMEGA project, are examples of typical dose data. STATDOSE functions include normalization, rebinning, plotting and analysis of the dose distributions. Distributions can also be compared both statistically and graphically. Graphs to aid in statistical analysis of the distributions, as well as both cross-plots and depth-doses, are provided by STATDOSE. The main functions of the program are:

- Statistical Analysis: In order to perform any of the statistical analysis routines, at least two distributions must be loaded. The two distributions selected for comparison must have the same structure (i.e. the same number of bins and the same bin boundary

values). Statistical analysis includes calculation of the chi-squared/degree of freedom and RMS deviations, the maximum absolute or percent difference in dose and the maximum dose along the central axis for the two distributions being compared. In addition, STATDOSE produces plots of the dose difference or percent dose difference distribution and of the chi-squared distribution.

- Normalization: This option asks the user to select the number of the data set to normalize. The normalized dose distribution replaces the original dose distribution and the product of the normalization factors applied to a given distribution is stored. The original distribution is retrieved with the 'denormalize' option, which divides the normalized distribution by the stored factor. If the distribution has been rebinned, the result of denormalization will be the original distribution, with all rebinning left intact. Options of normalization are :
  1. Apply Scaling Factor: which prompts the user for a scaling factor and multiply all the dose values in the distribution by this factor.
  2. Normalize to Average Dose: which finds the average dose for the distribution and the voxel where it occurs and also each element of the dose array is divided by the average dose.
  3. Normalize to Maximum Dose along Central Axis: which finds the maximum dose along the central axis of a distribution, the voxel where it occurs and also each element of the dose array is divided by the maximum dose.
  4. Normalize to Dose in Specific Voxel: which prompts the user for the coordinates of a voxel and after that each element of the dose array will be divided by the dose in this voxel.
  5. Denormalize: this option reverses all normalizations performed on a dose distribution by dividing it by the stored cumulative normalization factor in addition to these; denormalization will leave the binning structure intact.
- Plot: This function has two plot options, 'Plot Profiles' and 'Comparison Plot'. Comparison Plot may be selected if there are two or more distributions loaded. Both plot options allow several cross-plots or depth dose curves to be plotted on a single graph. Curves that are parallel to the X- and Y-axes are referred to as cross-plots, and those parallel to the Z-axis are depth-doses. Cross-plots and depth doses in which the curves are all parallel to a single axis of voxel geometry are allowed, but combinations of X, Y and Z-axis plots cannot be mixed on a single graph. Dose values are plotted in the voxels that lie parallel to the axis selected and pass through the selected coordinates.

- **Rebinning:** This option allows the user to choose the number of the dose distribution file to rebin, as well as the number and name of the rebinned file for plotting. Rebinning modifies the size of the bins in a dose distribution by a factor provided by the user. The rebinning factor must be an integer. For instance, a rebinning factor of 4 condenses the contents of 4 bins in the selected dose array into a single bin in a new dose array. Dose values in the 4 bins will be added together and averaged in order to calculate the new dose. Dose in any leftover bins will be added and averaged (where appropriate) and placed in the last bin of the new dose array. This function only handles positive integral rebinning factors, since it cannot perform any sort of data interpolation. This means that the number of bins may only decrease (bins may only increase in size). [83]

**Ctcreate:** The CT phantom option of DOSXYZnrc that allows calculation of dose distributions in phantoms that are derived from CT data sets. It is capable of reading in a CT data set of Hounsfield numbers and converting it into the information needed by DOSXYZnrc to simulate transport in a phantom (i.e., the appropriate material and density are specified in each voxel). The process by which CT phantoms are created by Ctcreate is

1. Read in the format of the CT data
2. Read in the CT header parameters (binary or ASCII).
3. Read in the binary CT data.
4. Choose a subset of the CT data set (if desired).
5. Resample the CT data to correspond to volume elements that dose will be scored in.
6. Convert the CT data to materials and densities for each voxel.
7. Transfer the data via a file to be input to DOSXYZnrc.

The relevant CT phantom information is written into the file, \*.egsphant which is used as a phantom created from CT data in DOSXYZnrc. [81]

**DOSXYZ\_show:** is a slightly modified version of vmc\_show, a small utility program from the VMC distribution, adapted to work with the DOSXYZ CT data and dose formats. It displays dose isolines on top of the corresponding CT data. The isolines are calculated using linear interpolation between the dose grid points. The program is written in C using the OSF Motif widget set and consists of a single file, dosxyz\_show.c [84]

Figure 4 below shows the isodose lines as displayed by DOSXYZ\_show.



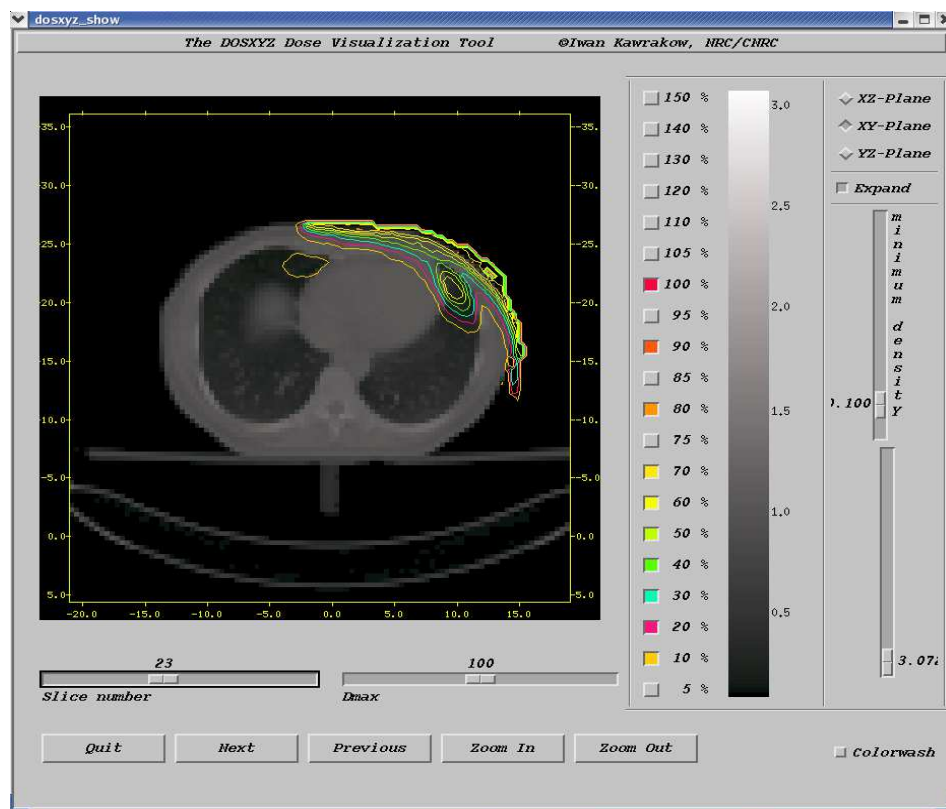


**Figure 4:** Isodose lines on the XY plane as displayed by DOSXYZ\_show

The main flaw of DOSXYZ\_show is that it does not allow contouring of organs, and thereby calculating the dose volume histogram, which is used to evaluate the different treatment options. This necessitates using another dose visualization and analysis tool.

### 2.1.3 XSTING

XSTING is home-built software written in Borland C++, utilizing Kitware's Visualization Toolkit (VTK) and running on Windows XP. It was originally designed for Stereotactic radio-surgery research and clinical treatment planning application and evaluation at the department of Medical Physics. As a research platform it was adapted to work with the DOSXYZ CT data and dose formats. It has the capability of exporting CT data in DICOM format and allows contouring of the different volumes and then superimposes the 3dd dose files produced by DOSXYZnrc to create isodose lines and DVHs.

## Functionality

XSTING shows the density distribution in a given Sagittal (S) Coronal (C) or Anterior (A) planes overlaid on the gray scale anatomic image representation. The dose distribution can be the isoline, color wash or even an isosurface of the planned dose distribution. The user can chose to view the 2D image, a 3D anatomical representation or the different delineated contours by clicking on Windows and selecting the view required. While function as a TPR XSTING calculates the spatial dose distribution for stereotactic applications, but it can also import other formats of 3D dose distribution files to visualize and overlay the dose to the appropriate CT set. The results can then be stored in systems own hierarchical database for future reference and study.

Several windows can be opened by the user these include: localize, contour, BEV, Dose, DVH and View. These windows are explained in details below

**Localize:** allows viewing the slices in full-screen size. In this window the user can chose to:

Changing the slice The user can change the slice by clicking on the Next or Previous buttons or by using the Slice number scale below the viewing area.

Selecting the view plane To select the plane (sagittal, coronal and anterior planes of the CT scans) to be shown in the viewing area.

**Contour:** contouring can be performed manually or semi-automatically. Manual contouring is performed using the mouse by adding points, representing points that belong to the organs external contour or by copying an already delineated contour from a previous slice and adjust it to fit. The delineated organ is then named and saved and a color can be allocated for that organ. After saving a delineated organ, the individual contours are combined to generate a 3D surface model of that organ. NB the extern has the universal orange color but the user can choose the color of other organs.

Editing the manually delineated contours can be performed by selecting the specific organ, click on "delineate", then "manual" and points can be added moved or even deleted.

The user can perform semi automatic delineation by determining the Hounsfield unit HU value then clicking on an already set (ROI) region of interest. This is useful in regions with big difference in density from the surrounding tissues, such as the external contour where the surrounding medium is air.

The user chooses automatic or selectable saving of the contoured region by clicking on/off on auto-save when changing slices.

**BEV:** This displays the "Beam's Eye View" of the specific slice.

**Dose:** From this window the user can choose dose related functions and settings like the Dose normalization point and the dose data matrix to display

**DVH:** this is where DVH calculations both accumulative and differential dose volume histograms DVHs for all delineated organs are computed and displayed.

**View:** this window has variable display options including: image, orientation, axes, patient information, in addition to other functions such as: isodoses and dose wash, grey scale level window, isodose levels, which determines which set of isodose lines to display, e.g. 10 to 100 step 10. There are also the options to choose the density range, i.e. the minimum and maximum densities and iso-surface Dose level, which is a 3D representation of the iso-surface receiving a certain dose range e.g. 50% of the dose can also be viewed as well as the point dose values which can be obtained by placing the mouse at the point of interest and then clicking the left button. The dose value at this point will appear on the screen. Moreover, the position of the hot spot within the patient can be traced by pressing the appropriate button to display the slice where the hot spot is visible. A special symbol displays the hot spot on both the plane as well 3D view of the patient.

Another functionality of XSTING is the ability to zoom the slices, which is performed by clicking on the Zoom-button, and placing the mouse on the required slice then dragging the mouse pressing on the right button.

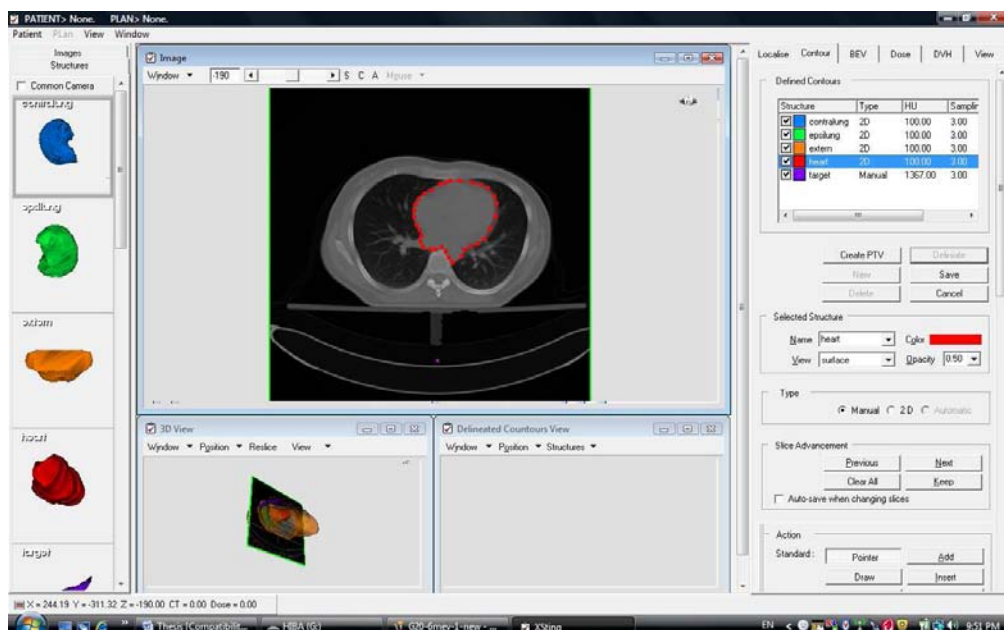


**Figure 5:** manual organ delineation as performed by XSTING

### 2.1.4 Dose Response Evaluation Software: DORES

Absorbed dose information provided by extracted Dose-Volume Histograms (DVH) from each treatment alone does not provide information about the response of healthy and malignant tissue to irradiation due to the loss of spatial information and the assumption that the whole organ is uniformly radiosensitive. However, when incorporated with dose response models (whether TCP or NTCP) this biological response can be quantified (to a certain level that will help positively to a better treatment). DORES (Dose Response Evaluation Software) is a simple tool for the assessment of radiotherapy treatment. It is a user-friendly program developed in Microsoft Visual Basic 6.0 designed to evaluate the biological response of irradiated healthy tissue. The Normal Tissue Complication Probability (NTCP) is computed, using available Dose-Volume information, through the application of three dose-response models (LKB, Relative Seriality and Parallel) and associated published parameter sets.

Table 1 below shows the set of Model parameters used by DORES

Models	Parameter values			
<b>Relative Seriality model</b>	$D_{50}$ (Gy)	$\gamma$	$s$	$\alpha/\beta$
Seppenwoolde <i>et al</i> (2003)	34	0.9	0.06	2.5-3.0
Gagliardi <i>et al</i> (2000)	30.1	0.97	0.01	3
Mah <i>et al</i> (1987)	26	2	0.031	-
<b>LKB model</b>	$TD_{50}$	$m$	$n$	$\alpha/\beta$
Burman <i>et al</i> (1991)	24.5	0.18	0.87	-
Seppenwoolde <i>et al</i> (2003)	30.8	0.37	0.99	2.5-3.0
<b>Parallel model</b>	$TD_{50}$	$m$	$n$	$\alpha/\beta$
Seppenwoolde <i>et al</i> (2003)	31	0.32	0.67	2.5-3.0

**Table 1:** The different models used by DORES and the associated set of parameters [84]

Dose-response curves are provided for associated patient sets, with NTCP, Biological Effective Uniform Dose D and Equivalent Uniform Dose (EUD), values also provided. The predictive power of the dose-response models is evaluated using DORES. By knowing the clinical outcome for each patient treatment DORES can be used as a post

irradiation analysis tool, to evaluate the ability of the dose-response models in accurately foreseeing a specific level complication. The complications observed in the normal tissues after radiation therapy have been described in terms of inactivation of functional subunits (FSU). The organization of the FSU is described as serial, parallel or a combination of these two patterns. If arranged in parallel the response of the associated organ or tissue is a graded response but if arranged in series the response is binary [84].

Dose-volume information for each patient is entered into the required fields of the form as shown in Figure 6 and this is then processed by the DORES application.

PATIENT THERAPY DATA FORM	
HOSPITAL	University Hospital Larisa
Organ Classification	Lung
Patient No.	A
Total Dose	60.1
Number of Fractionations	33

Dose	Volume
0	1173.872314
0.601	1164.349491
0.9015	1127.356987
1.202	1058.865837
1.5025	971.206764
1.803	899.052955
2.1035	830.439727
2.404	772.570262
2.7045	732.281394
3.005	700.782823
3.3055	672.214351
3.606	654.145402
3.9065	646.575978
4.207	641.936653
4.5075	636.076454
4.808	628.01868
5.1085	624.356055
5.409	621.425956
5.7095	617.274981
6.01	614.344881
6.3105	611.414781
6.611	608.728856

**Figure 6:** Patient Therapy Data form [84]

The 'Patient Therapy Data Form' is stored on the hard drive of the PC or an associated database system and is loaded by the user into the primary software tool component. The user is then required to select the dose-response model to perform the evaluation of Normal Tissue Complication Probabilities (NTCP). One of the three most commonly used models of dose-response can be selected for the analysis.

## 2.2 Methods

### 2.2.1 MEASUREMENTS

In our study, the measured data include central axis depth dose distribution and lateral dose distribution at the depth of  $D_{max}$  for field sizes of 6x6, 10x10, 14x14 and 20x20 cm<sup>2</sup>. All measured data were acquired in water using a Markus 2586 ionization chamber. All measurements and measurements corrections were done in accordance with TRS-398 recommendations. Corrections to obtain the dose in water included that for effective detector position, polarity, leakage and stopping power ratios. The central axis depth dose curves and dose profiles were normalized to the maximum dose value  $D_{max}$  at the depth of maximum dose. Measurements were obtained at a source-to-surface distance (SSD) of 100 cm.

### 2.2.2 BEAM INSTALLATION:

The BEAM code including BEAMnrc, DOSXYZ or DOSXYZnrc, BEAMDP, and EGS Windows were installed into a cluster of five computers using the online resources of the National Research Council of Canada at:

<http://www.irs.inms.nrc.ca/inms/irs/BEAM/beamhome.html>

### 2.2.3 LINAC SIMULATION AND VERIFICATION:

Three steps have to be followed to simulate any linear accelerator using EGSnrc/BEAMnrc codes:

**First**, the accelerator has to be "specified". This means which component modules are to be used and in what order. Next, it must be "built", which corresponds to concatenating all of the relevant source code for the CMs and editing it to avoid duplicate variable names. Then these CMs are added together or compiled to make a single, connected linear accelerator. PEGS4 data are then selected, which assigns options for the materials used.

The positions, dimensions, design and materials are chosen for each component module. This is followed by choosing the input parameters for the beam and then, saving the input file. The design of the accelerator's component modules and the beam parameters can be altered but the choice and arrangement of the component modules cannot be altered, and if the user needs to change it, a new accelerator is to be specified, built, etc. A small run, with a few histories is usually performed to check if there is an error in construction, and upon success, the number of histories is altered and the verification run is made. Parallel processing allows reduced running time. This is done by installing and

enabling a queuing and filing system in each computer of the cluster and then starting it using the command:

```
Qmgr start nqs
```

Parallel process is then done by going to the EGSnrc/BEAM/Accelerator directory and typing the command:

```
pprocess BEAM_myaccel - inputfile pegsdata n_parallel long nqs
```

The latter is the queuing system used by the cluster

The phase space files of the different runs are added using:

```
addphsp inputfile outputfile ipar [istart] [iscore] [i_iaea]
```

where inputfile is the name of the original input file (no .egsinp extension), outputfile is the name of the output file for the concatenated phase space data (a .egsphsp[iscore] extension is added automatically), ipar is the number of parallel jobs being added, istart is the job number at which adding begins (i.e. the first value of i\_parallel)-defaults to 1, iscore is the scoring plane number for which you are combining phase space files (i.e. are you adding .egsphsp1, .egsphsp2 or .egsphsp3 files?)-defaults to 1, and i\_iaea is set to 1 if you are adding IAEA-format phase space files-default is 0.

### **The geometrical details of the accelerator's components**

The electron beams from ELEKTA SL18 were simulated according to the manufacturers' data on the treatment head geometry using BEAMnrc/EGSnrc.

The following parameters were used:

The accelerator head was built from the following component modules (CMs) CONESTACK, which consists of a stack of truncated cones, surrounded by a cylindrical wall, was used to simulate the exit window and the primary scattering foils. It was used for the secondary scattering foils for low and moderate-energy beams. CONS3R was used for the primary collimator and the secondary scattering foils for high-energy beams. The distance between the primary and secondary scattering foils varied with the energy of the incident beam. The ionization chamber, jaws and applicators were simulated using IONCHAMB, JAWS and APPLICAT component modules respectively.

**Second**, the resulting phase space file is used as an input source for the DOSXYZnrc phantom simulation. The number of voxels, dimensions, materials as well as the EGSnrc input parameters is then specified. A small run is performed as before, followed by a big parallel run. The resulting .pardose files are then added using: combine dose

command to produce the 3ddose file which contains the information about the simulation geometry and the calculation results.

The **third step** in the verification procedure is the statistical analysis performed by Statdose. From the EGSnrc/DOSXYZnrc directory the user types: Statdose, which takes him to a window where the 3ddose file are read and normalized then used to generate xvgr/xmgr plots for comparison purposes. The generated percent depth dose (PDD), normalized to Dmax, and the dose profiles are then exported to EXCEL to compare them with the measurements taken for the different energies (6, 8, 10, 12, 15 and 18 MeV) and different field sizes (6x6, 10x10, 14x14 and 20x20 cm).

Figure 7 below shows the design and the built Linac

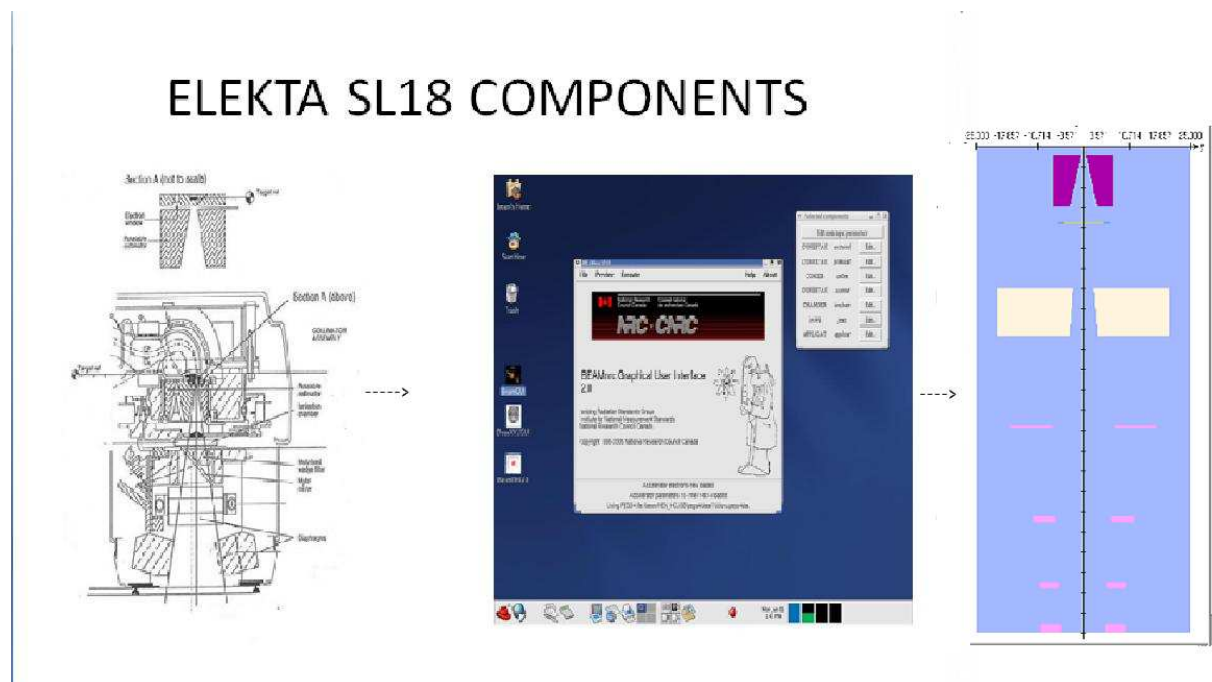


**Figure 7:** Linac, component module and simulated Linac

The choice of energy threshold below which the histories of electrons and photons (global ECUT and PCUT) or their product knock-on electrons and Bremsstrahlung photons (AE and AP) are terminated, was the same for both Linac and phantom simulations. ECUT and AE were both set to 0.521 MeV. PCUT and AP were set to 0.01MeV. Boundary crossing and electron step-size algorithms were chosen to be PRESTA1 and PRESTA2 respectively. A mono-energetic beam from (ISOURCE =19) that involves a circular beam with 2D Gaussian



distribution was chosen for our beam simulations. No photon or electron splitting was performed. In order not to reject any low energy electrons the global ESAVE was set to zero. A cluster of five computers with different processor speeds was used for parallel processing. The number of particles used for simulation ranged from 200-500 million particles depending on the energy and field size. This number decreased with increasing beam energy and field size. In phantom simulations the histories were chosen so that the particles from the phase space files were not recycled more than 30 times to avoid unnecessary uncertainties. Fine-tuning of the beam was performed until a good match in relative depth dose and dose profiles between measurements and calculation was reached. This included alteration in the intrinsic energy as well as energy distribution of the beam. It has been reported that the full width at half maximum (FWHM) of the intrinsic energy spectrum is about 5% and 10% of the most probable energy for accelerators of the travelling wave and standing wave types respectively[85]. This value did not produce a satisfactory match between the measured and the calculated percent depth dose. The value was altered until a better match was produced.

Figure 8 below shows the input parameters chosen for the verification process

Parameter	Value
Title	electron-new
Medium	AIR700ICRU
Bremsstrahlung Splitting	none
WATCH Output	none
Split electrons or photons at CM	none
RNG Seed Options	store RNG at start of each batch
Incident particle	electron
Run option	first time
Source number	19 - Parallel circular beam with gaussian radial distribution
Output Options	phase space at each scoring plane
Global electron cutoff energy - ECUT (MeV)	0.521
Store Data Arrays	yes
Global photon cutoff energy - PCUT (MeV)	0.01
LATCH option	inherited latch - set by passage
Electron range rejection	off
Score Last Z	last interaction
Global electron cutoff (ESAVE_GLOBAL, range rejection, MeV)	
Photon forcing	off
Number of histories	80000000
Number of scoring planes	1
Initial RNG seed 1	33
Dose calculation	Only total dose
Initial RNG seed 2	97
Z of front of 1st CM to reference plane (cm)	0.0
Maximum CPU hours allowed	200

**Figure 8:** the main input parameters chosen for simulating the Linac

Different scattering foils were designed according to the energy of the electron beam. CONSTAK was used to simulate this component module for all energies but 18 MeV.

The openings of the X and Y diaphragms were also altered to reach to a good match between the measurements and simulations. No diagrams of the applicators' designs or materials were provided in the manual. Measurements of the dimensions of the scrapers of each applicator were performed. Simulations were done using different options of materials, specifically lead and Aluminum, which are the common materials for applicators provided by ELEKTA and the output PDDs and dose profiles were used to decide the materials of the applicator.

The effects of these alterations in beam parameters or Linac configurations were studied as explained in the following session

## **2.2.4 Evaluation of sources of systematic errors in simulations**

**BEAM CONFIGURATIONS:** The effect of small alterations in initial beam parameters, and configuration of some accelerator components was investigated for 10x10 fields using 4 MeV, 8 MeV, 15 MeV and 18 MeV electron beams as follows

**ENERGY DISTRIBUTION OF THE INITIAL BEAM:** The effect of decreasing and increasing the FWHM beyond the verified values was studied on both PDD and dose profiles. This is done because the value that produced a good match between measured and calculated central axis PDD was more than the suggested 10% of the most probable energy.

### **PHANTOMS:**

**SOURCE-TO-SURFACE DISTANCE (SSD):** from a practical point of view, a longer distance between the collimator and the patient is often preferable; otherwise the collimator might collide with the shoulder of the patient when tumors in the neck region are to be treated [86]. The effect of SSD was investigated by locating the phantom immediately after the last scraper of the applicator i.e. at a SSD of 95 cm and at 100 cm and 105 cm respectively.

**VOXEL SIZE:** Calculated dose is affected by the size of the scoring voxel. For MC calculations typical values in the scoring dimensions are voxel sides of 2-5 mm for field sizes greater than 3x3 cm<sup>2</sup>. Increasing the voxel size reduces the simulation time as well as the size of the output 3ddose files but may affect the statistical uncertainty [87]. A water phantom consisting of Cartesian voxels of water was simulated using DOSXYZnrc. Different voxel side dimensions: 2.5 mm referred to as small voxels, 5 mm referred to medium voxel size and 10 mm referred to as big voxels were used to study the effect of voxel size on both PDDs and dose profiles.

### ***LINAC CONFIGURATIONS:***

***THE SCATTERING FOILS:*** SL18 has dual scattering foils that consist of a high-z (atomic number) material to broaden the beam into a Gaussian profile and a lower-z Gaussian-shaped foil that minimally scatters the electrons at the tail of the profile and maximally scatters electrons near the centre to flatten the field in the area of interest with a suitably sharp fall-off at the field edges. The effects of materials and dimensions of the scattering foils for mono-energetic and poly-energetic beams have been extensively studied elsewhere. [88-90] No literature was found explaining the influence of walls of the scattering foils. For low and moderate energies of SL18 (up-to 15 MeV), the shape of the foils descends in an increasing diameter pattern, which allows simulation using the CONESTAK component module. This allows simulation of the walls. The situation is different for higher energies, 18 MeV and above, where it was necessary to use CONS3R that does not allow simulation of the walls or FLATFILT option that allows simulation of overlapping cones with varying diameters and simulation of the surrounding walls. In this paper the height of the walls of the scattering foils was altered and the foils were simulated without the walls to compare the PDDs and profiles generated with and without alterations.

***THE IONIZATION CHAMBERS:*** Most Linacs have segmented ion chambers that allow monitor both beam intensity and uniformity [91]. The monitor ionization chamber of the SL18 is made in form of thin layers of a light material separated by air gaps. This is embedded in a metal disk. Accurate simulation of the ionization chamber is not necessary in a simulation of photons where a good match between measured and calculated PDD and profiles was possible with a 1 cm thick water slab simulated by SLAB CM, which is relatively easy to simulate. This is not the case for electron beams, where all components on the beam direction are expected to influence the dose. Simulation of the ionization chamber was performed using IONCHAMB component module, SLAB of Mylar 0.072 cm thick, which represents the total thicknesses of the Mylar films within the ionization chamber, and CONSTAK. SLAB option was used to evaluate the possibility of simplifying the simulations and CONSTAK option was used because IONCHAMB module does not allow accurately simulating the different materials of the inner walls surrounding the different segments. Finally simulation was performed without the ionization chamber and the results were compared.

***THE MIRROR:*** The light localizing system, which consists of the light source and a thin mirror, is used for field size definition within the patients. Despite the very small thickness of the mirror, being on the path of the electron beams, it may have scattering effects. The influence of the mirror was investigated by simulating the Linac with and without mirrors.

*THE JAWS:* The jaws opening, which indicates the field size at a named SSD, usually 100 cm and the inclination of the jaws are automatically defined at the Linac monitor according to the applicator used and the energy. Using these values for x and y openings from the monitor of the Linac did not always produce a good match between measured and calculated profiles. Neither did calculations of the openings according to the opening of the upper scraper of the applicators or according to the required field size, 10x10 for example. The effect of altering the jaws opening was studied in this work.

*APPLICATORS:* In radiotherapy with high-energy electron beams, scattered radiation from the applicator influences the dose distributions in patients. The amount of radiation is dependent on the applicator design [92]. Electron applicators provided by ELEKTA are in the form of sets of diaphragms or scrapers with a thick base that is attached to the treatment head. This reduces the intensity outside the useful beam to less than 2%. In this paper the effect of two different materials: lead and aluminum, which are the materials for ELEKTA applicators, are investigated.

## **2.2.5 Electron postmastectomy radiotherapy**

### **STEP 1: Verification of XSTING:**

The first step was the verification of XSTING, which is used for the first time with outputs from MONTE CARLO BEAM. This is done by producing isodose lines using both Ctcreate/DOSXYZ\_show combination and XSTING and comparing them. Then the created DVHs are visually compared with the 3D representation of volumes receiving a certain dose range, to make sure that XSTING accurately computes DVHs.

**Using BEAM,** CT data in DICOM format is imported to the system using CT phantom option of DOSXYZnrc, Ctcreate.

From the EGSNRC/DOSXYZnrc directory the user types:

Ctcreate

This takes to the window where CT format is chosen. Ctcreate supports Pinnacle, CADPLAN and DICOM format. Next, the CT Filename is given. On output, the CT phantom will be named:

CTFilename.egsphant

Then, xctsubmin, xctsubmax, yctsubmin, yctsubmax, zctsubmin, and zctsubmax are used to create six planes which describe a cube. The subsection of the original CT data contained in this cube will be used to create the CT phantom. In this manner only the portion of interest in the original CT data is used in the simulation. This allows the particle

simulation to be performed at a higher resolution than if the calculation used the entire CT volume, and allows the user to trim some of the air that surrounds a typical CT image from consideration in the phantom.

The third line of the input to Ctcreate is the spatial resolution that the user requires for the simulation. xyz\_xthickness, xyz\_ythickness, xyz\_zthickness are the 3 dimensions of the voxels to be used in the CT phantom. The maximum voxel dimension in a given direction is the distance between the planes delimiting the subset of the CT data to be used in that direction

The materials are then defined by: num\_material is the number of materials that are to be used for the ramps that are to convert each voxels from CT number to material and density. If this is set to zero then a standard set of CT ramps are used in the conversion. This was the number of choice for the following work. [81]

The phase space files of the verified electron beams with energies of 4-18 MeV, with different field sizes are then used with a phantom derived from the desired CT scans depending on the thickness of the chest wall. The coordinates of the isocentre are then chosen. The position and orientation of the beam are then determined using the values Theta, Phi and collimator angle and the distance from source to isocentre. Theta is the angle between the positive z direction (of the irradiated phantom) and a line joining the centre of the beam where it strikes the phantom surface to the isocentre. Phi is the angle between the positive x direction (of the irradiated phantom) and the z projection on the x-y plane of the line joining the centre of the beam on the phantom surface to the isocentre on the x-y plane. Phi collimator is the angle by which the source is rotated in the source plane perpendicular to the (beam) direction. The dose visualization tool DOSXYZ\_show to produce isodose lines then uses the resulting .3ddose file. The 3ddose files are also exported to XSTING for further applications as explained below.

### **Using XSTING**

CT data are imported in XSTING using: PATIENT→ IMPORT →EXT DICOM IMAGE.

The 3ddose files produced earlier are then imported and superimposed on XSTING using: PATIENT→ IMPORT →Dose; and normalized. The isodose distributions displayed by XSTING are then compared with that of the benchmarked DOSXYZ\_show to evaluate the performance of XSTING.

DVHs are then computed by XSTING and visually compared with the 3D representation of volumes receiving a certain dose range, to make sure that XSTING accurately computes DVHs.

In the next step to verify the output of XSTING, the DVH of one organ, the (ipsilateral lung), using one of the energies (12 MeV) was generated. The isodose line and 3D image for volume of the lung that receives specified dose-levels e.g. 10% and 70% of the normalized dose,  $D_{norm}$ , were compared with the values of the DVH.

## **STEP2: Treatment Planning**

Organs' delineation of the extern, target, ipsilateral and contralateral lung and heart, is then performed manually. The resulting contours are then saved and exported to the C-directory to be re-imported many times during the study. The 3ddose files for the different energies, angles and field sizes are then imported and DVHS for the organs at risk are computed and exported to EXCEL files

## **STEP3: Dose Evaluation**

### **DVH evaluation**

Dose volume histograms (DVH) were calculated for the target and organs at risk. These are used to study:

- The homogeneity of the dose distribution in the target
- The maximum dose received by the organs at risk
- The volume of organs that receive a certain threshold dose
- The volume of organs that receive low doses of radiation.

### **Dose response Evaluations using DORES:**

The exported EXCEL DVH files are uploaded into the Patient Therapy Data form to be processed by DORES. The volume of the different organs is changed from percent to actual volume, and the results are placed in decreasing dose pattern. The Patient Therapy Data form, which is stored in the hard drive of the computer, is then loaded. The dose response model to perform the evaluation of Normal Tissue Complication Probability for the lung and heart is then chosen. (LKB or Relative seriality) The parameters intended for NTCP calculations, which are available in the literature and in a window in DORES selected by clicking on 'view parameters' button, are then entered. The LKB model was chosen for this study and parameter sets from Seppenwoolde et al. were used for the evaluations based on recommendations by Tsougos et al. [84]. Selecting the organs' classification follows this; here, single lung and heart were chosen. Finally, DORES is set to perform the analysis. DORES process the DVH files to produce NTCP values for each study. The NTCP values are plotted on the theoretical dose-response curve against BEUD (Biological Effective Uniform Dose) for the case of the Relative Seriality model, or against EUD

(Equivalent Uniform Dose) for the LKB and parallel models. [84]. Figure 9 below demonstrates this procedure.

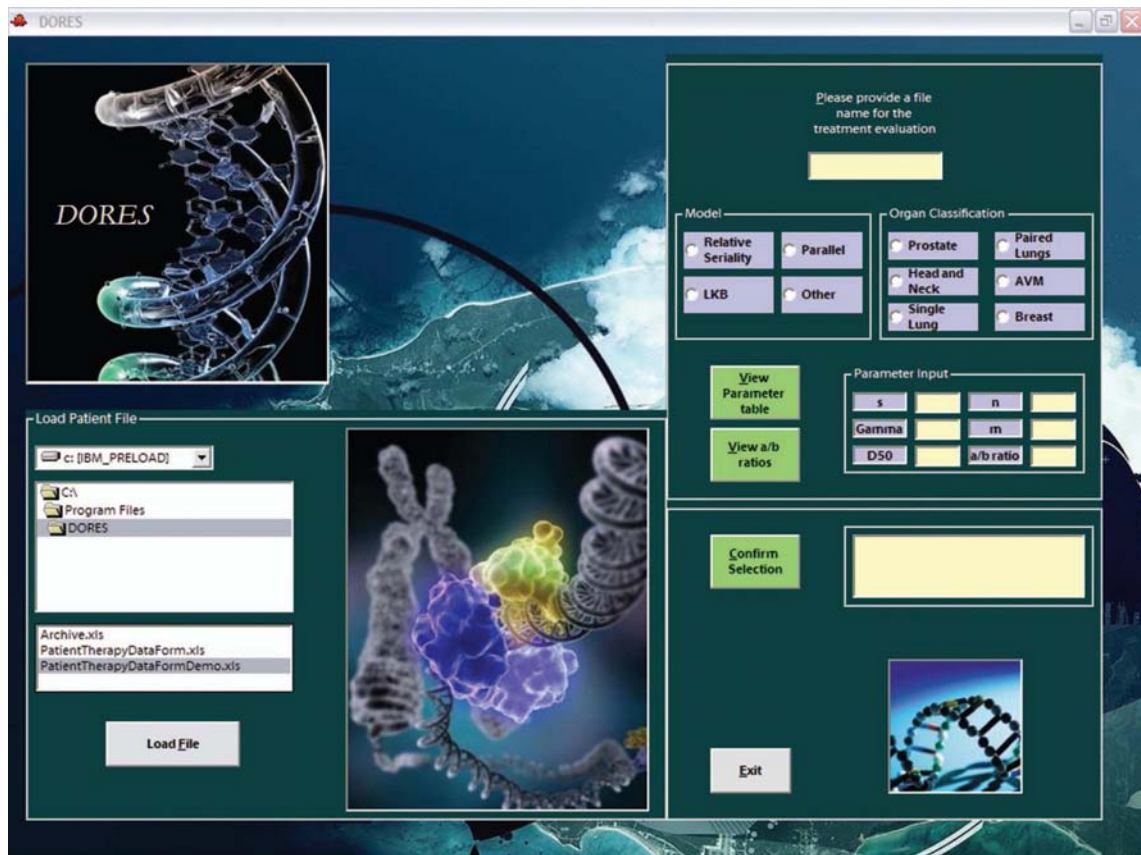


**Figure 9:** DORES primary software components. On the right hand side of figure 7 is the "load file" button, where the user loads the patient's information. On the left hand side there are the different NTCP models, from which the user chooses one model. There is also the organ to be studied, prostate, head and neck, etc. Below these are the input parameters to be chosen, with an option of viewing the published parameters. The user then confirms the selections and allows DORES to perform the analyses. [84]

## **CHAPTER THREE: RESULTS**



### 3.1 Measurements

The measured, normalized depth ionization curves were transferred into an Excel data sheet and transferred to depth dose curves by multiplying each value with the stopping power ratios provided by TRS398 group.

### 3.2 LINAC SIMULATION AND VERIFICATION:

Beam Configurations:

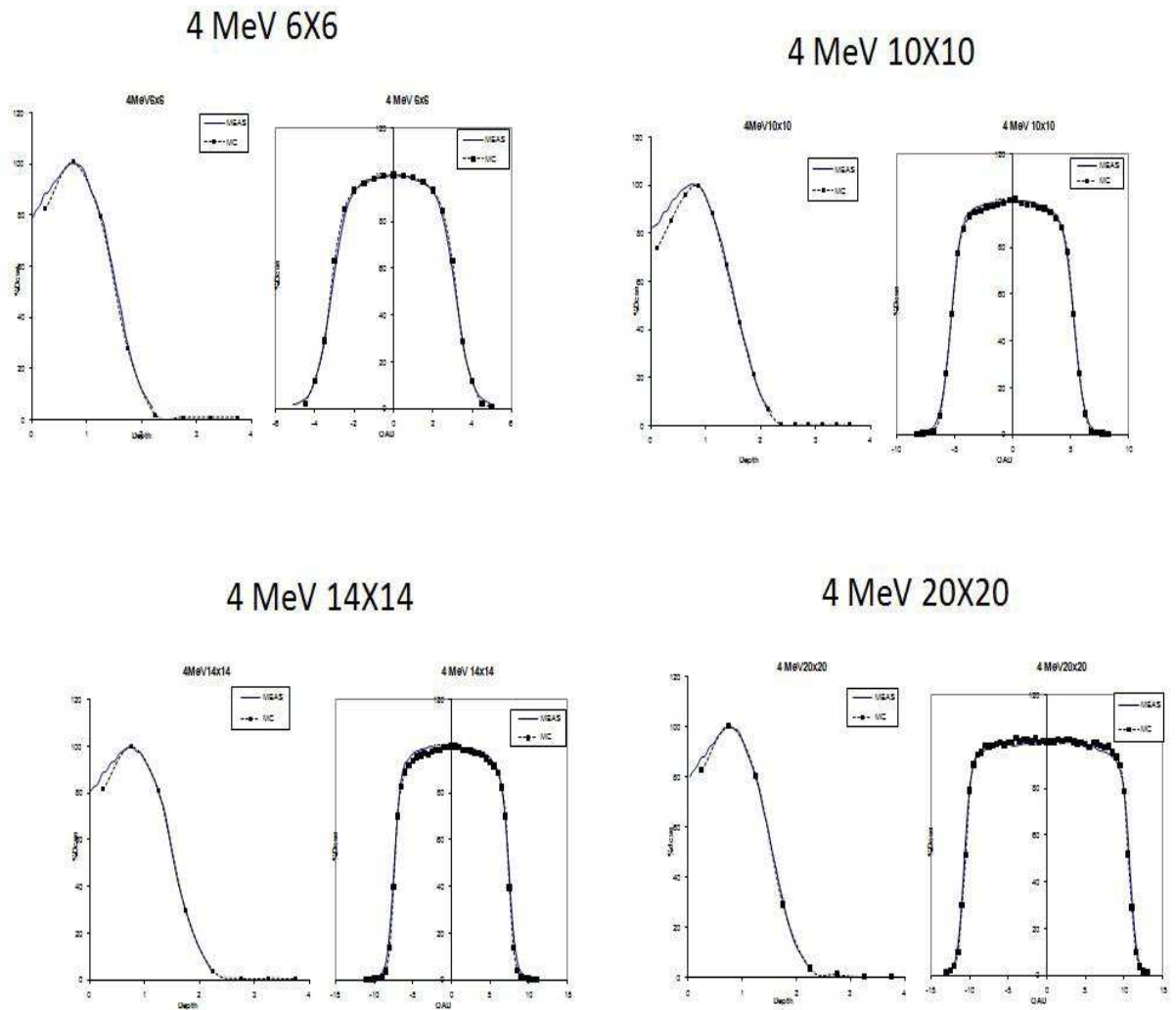
The Linear accelerator was said to be verified when the comparison between measured and calculated percent depth dose and dose profile curves produced a similarity with a maximum deviation of 2% or 2 mm.

In order to satisfactorily simulate and verify the Linac, different beam input energies and beam widths were tried and compared with the measured absorbed dose. The Linac configuration was not much altered. Each component module was simulated as the manual although slight changes in the dimensions of the jaws openings were necessary for verification. The energy of the input beams slightly varied with the field size. The energy width of the beams also slightly changed with the energy of the beam. Table I below shows the energy range of the input beam as well as the beam's energy width for each of the simulated energies.

<b>E<sub>0</sub> (MeV)</b>	<b>E<sub>1</sub>(MeV)</b>	<b>FWHM (MeV)</b>
4	4.5-4.6	1.7
6	6.55	1.8
8	9	2.5
10	10.7-10.8	1.8
12	12.6-12.7	2.1
15	15.5-15.55	2.0
18	18.55	2.1

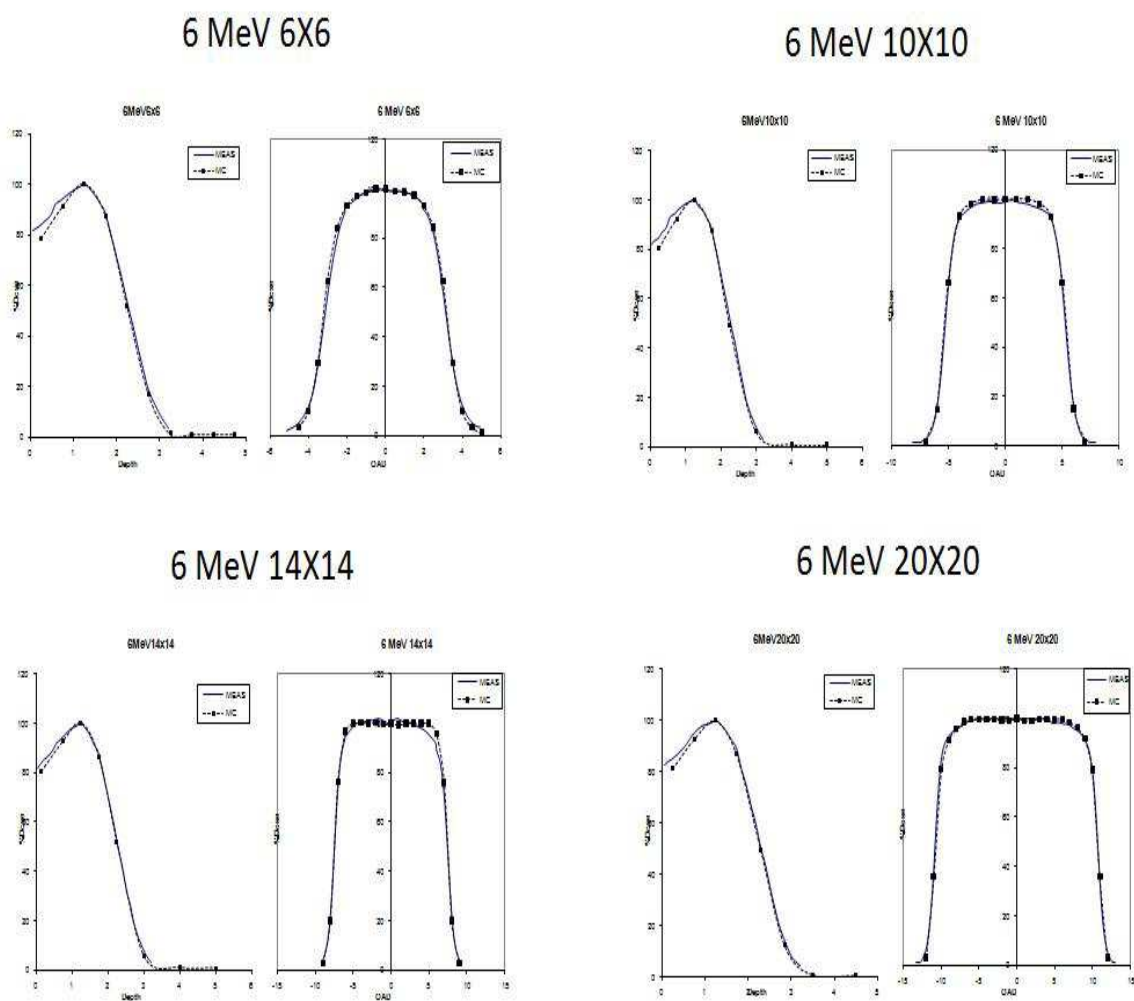
**Table 2:** nominal energy, input energy and energy distribution values

Figure 10 to Figure 16 below show the percent depth dose and dose profiles at Dmax for different energies and field sizes. As can be seen from the graphs, the discrepancy between the measurements referred to as MEAS and the calculation, referred to as MC, curves is below 2% of the point dose except at the surface.



**FIGURE 10:** 4 MeV verification graphs for 6X6, 10X10, 14X14 and 20X20 cm<sup>2</sup> field sizes

Except for the surface dose, the discrepancy between measured and calculated curves is within 1% for all field sizes.



**FIGURE 11:** 6 MeV verification graphs 6X6, 10X10, 14X14 and 20X20 cm<sup>2</sup> field sizes

A slight depression of jaws in right shoulder of measured 14x14 dose profile is noticed but the discrepancy is still within the allowed 2% value.

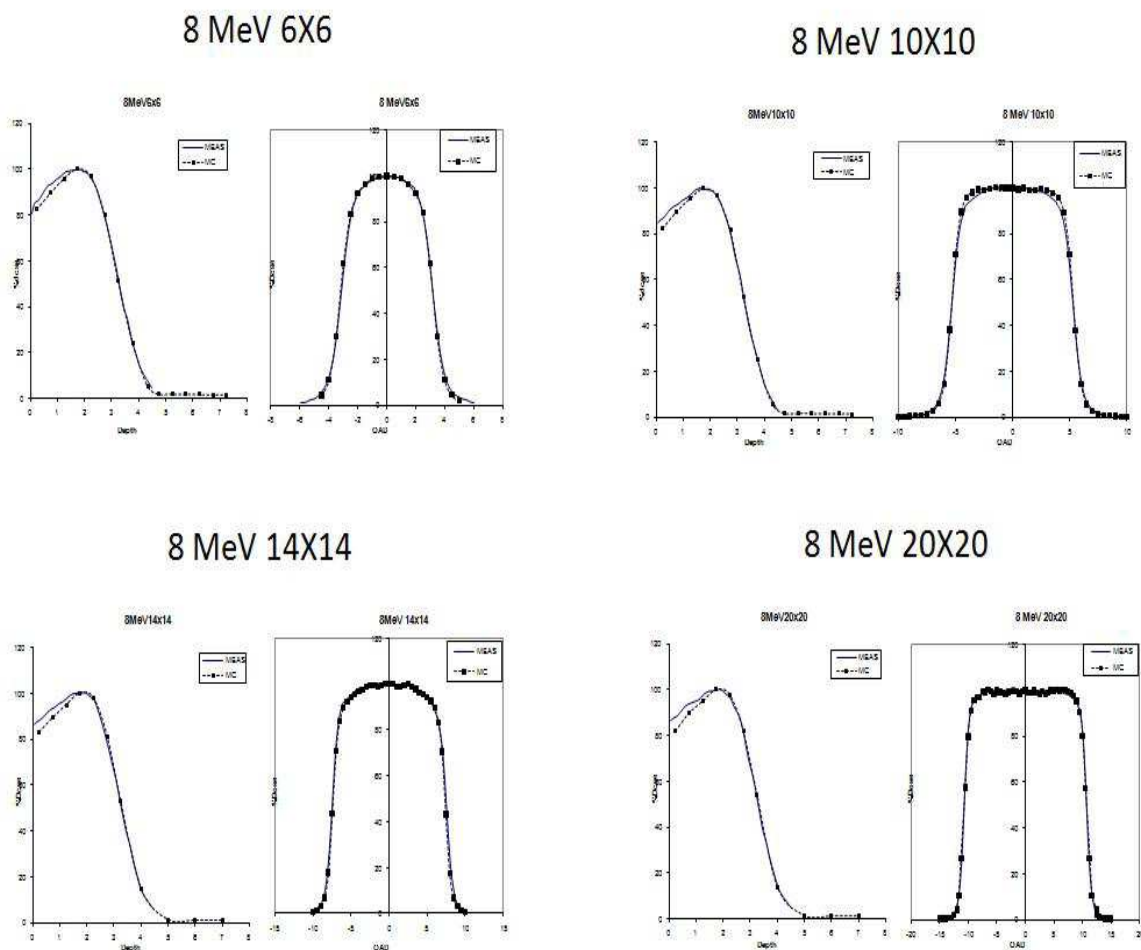


**FIGURE 12:** 8 MeV verification graphs 6X6, 10X10, 14X14 and 20X20 cm<sup>2</sup> field sizes

A good agreement between measured and calculated depth dose and dose profiles is seen from the above graphs. As before, the maximum discrepancy between measured and calculated data is in the surface dose.

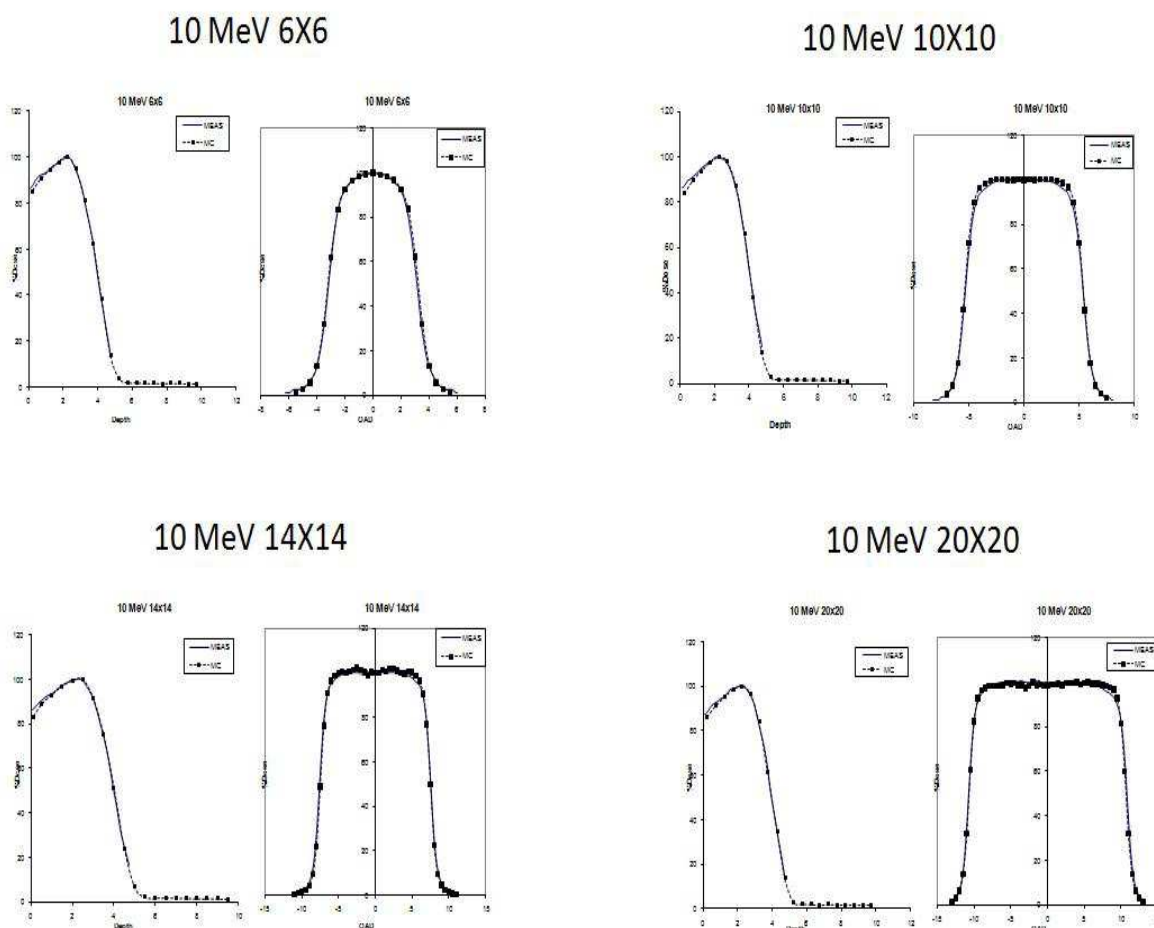


**FIGURE 13:** 10 MeV verification graphs 6X6, 10X10, 14X14 and 20X20 cm<sup>2</sup> field sizes

Similar to the above results, the discrepancy between measurements and calculations is within 2% as interpreted from the graphs. The highest deviations are noticed, again, at the right shoulder, where a slight depression is noticed in the measured dose profiles.

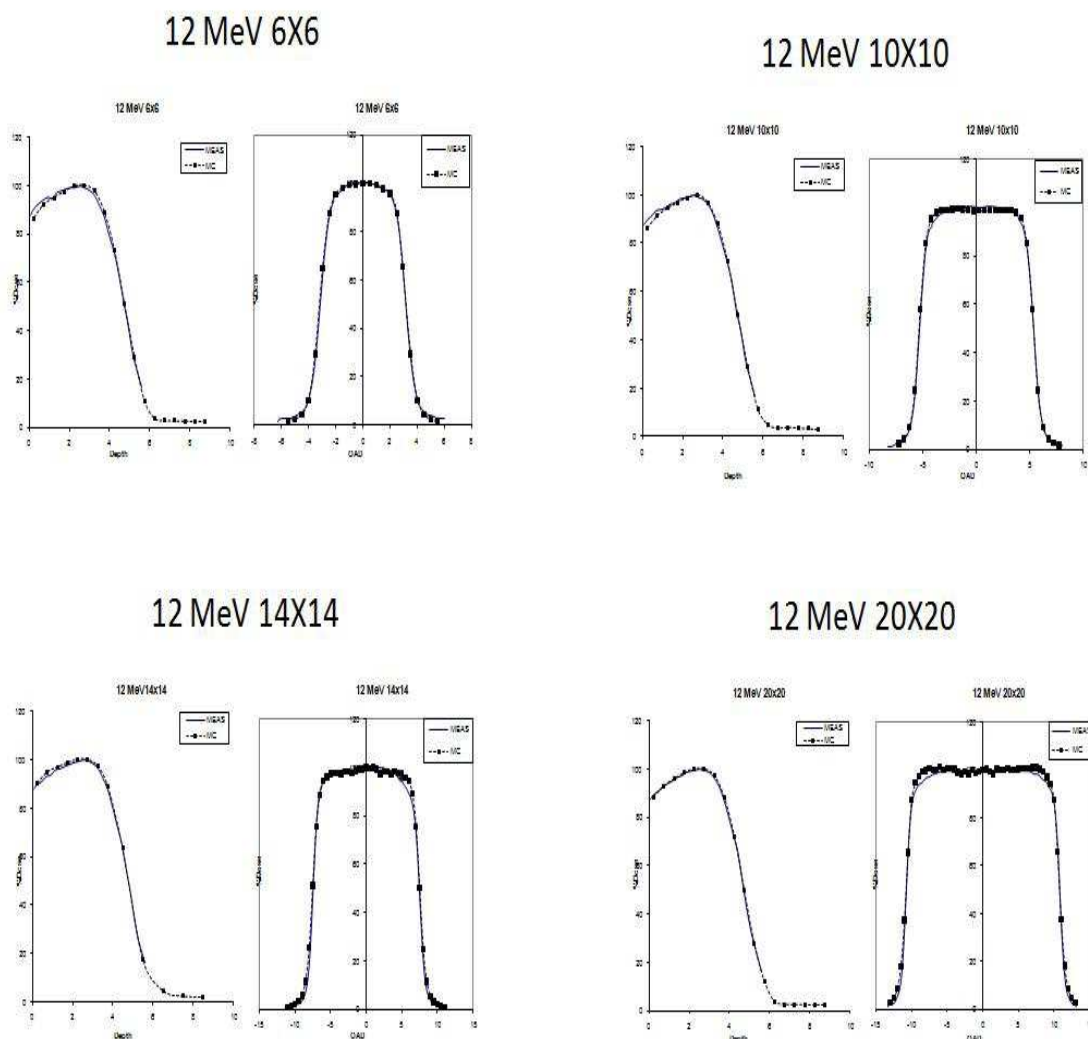


**FIGURE 14:** 12 MeV verification graphs 6X6, 10X10, 14X14 and 20X20 cm<sup>2</sup> field sizes

There is a good agreement between the measured and calculated percent depth dose curves. The right side shoulder of the measured profile for the 14X14 field is also slightly depressed. The calculated profiles of the calculated 20X20 field seem to have 'horns' but the difference does not exceed 2mm.

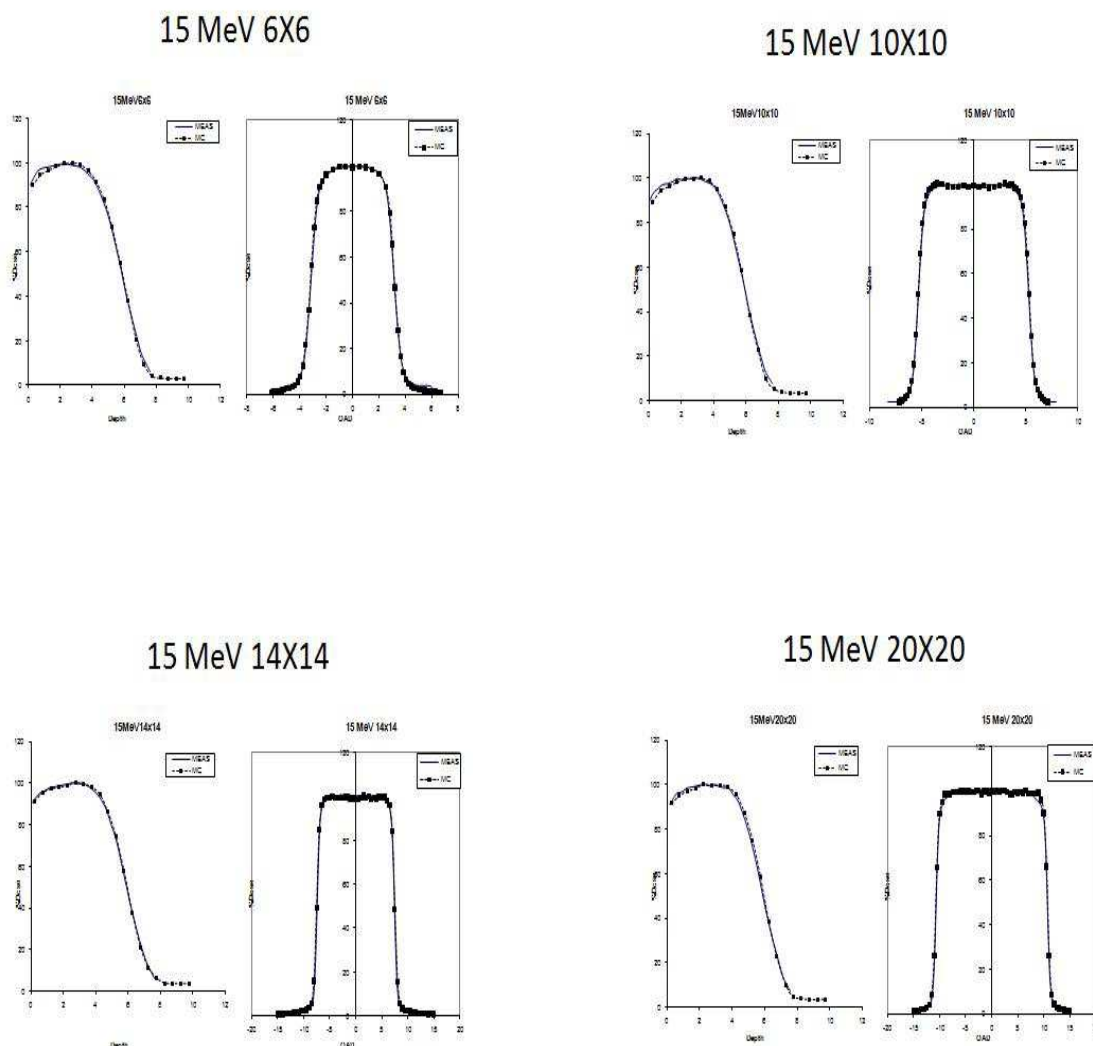


**FIGURE 15:** 15 MeV verification graphs 6X6, 10X10, 14X14 and 20X20 cm<sup>2</sup> field sizes

As can be seen, a very good agreement occurs between the measurements and calculations, even in the surface dose.

## 18 MeV 10X10

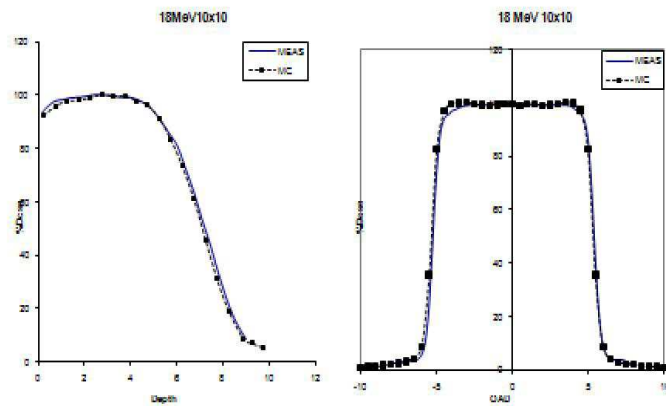


**FIGURE 16:** 18 MeV verification graphs 10X10cm<sup>2</sup> field sizes

Comparison was performed between measurements and calculations for 10X10 cm<sup>2</sup> and the measured and calculated percent depth dose curves and dose profiles, and the results were within the 2%-2mm discrepancy.

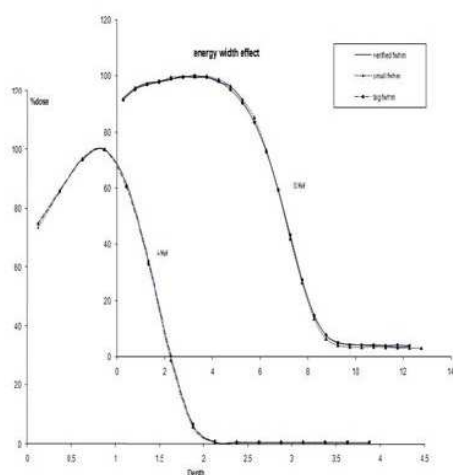


### 3.3 Evaluation of sources of systematic errors in simulations

The effect of slight alterations on beam parameters and Linac configurations are summarized below:

**ENERGY DISTRIBUTION OF THE INITIAL BEAM:** Increasing the beam width from 10% of the most probable energy (referred to as small FWHM in the graphs) to the verified FWHM MeV slightly decreased the dose gradient and slightly increased the Bremsstrahlung tail for the different energies. More effect is noticed on the PDD of the high energy (18 MeV). A much smaller alteration is noticed with further increase in the FWHM. The increase in FWHM slightly affects the dose profiles where the flatness is reduced and the shoulder is depressed with a further increase in beyond the verified value, referred to as big FWHM. This can be seen more clearly for the small energy (4 MeV). The effect of energy width on PDD and dose profiles is demonstrated in Figure 17 below for 4 MeV and 18 MeV electron beams.

**Effect of fwhm on pdd**



**Effect of fwhm on profiles**

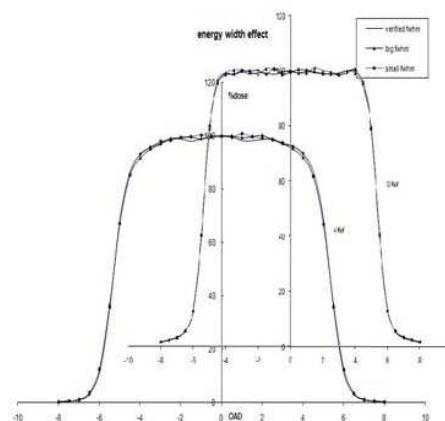


**FIGURE 17:** Effect of alterations of the energy width on pdd and profiles

### PHANTOMS:

**SOURCE-TO-SURFACE DISTANCE (SSD):** From Figure 18 below it is evident that increasing the SSD from 95 cm to 105 cm slightly reduced the surface dose with almost no effect in the remaining parts of the PDD. This is basically because the difference in distance from the source is not big enough to cause the effect of the inverse square law for distances. The big effect is witnessed on the dose profiles, where the penumbra increases drastically with increase in SSD, as a result of the air gap.

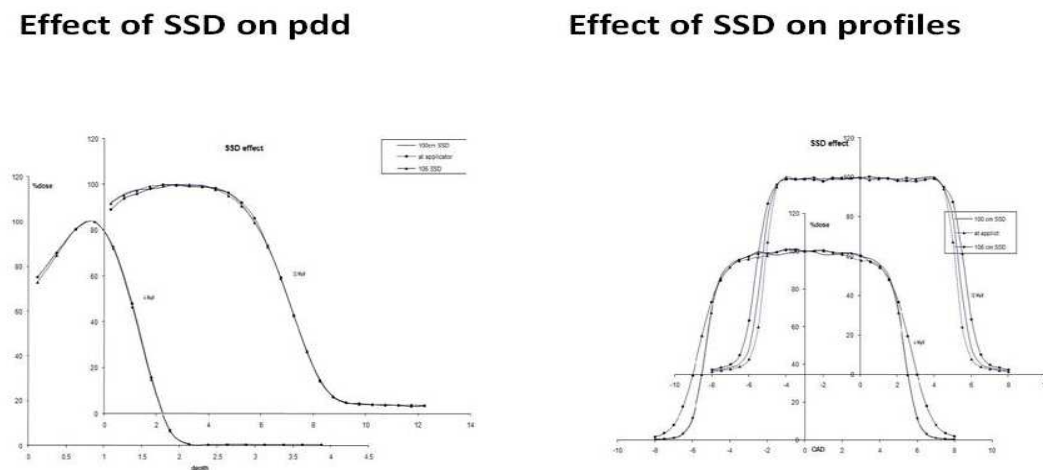
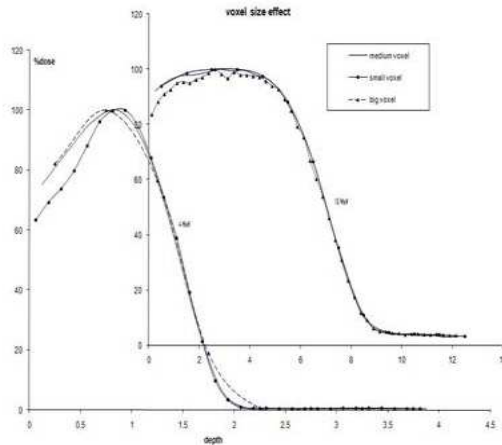


**FIGURE 18:** Effect of alterations of the source-to-surface distance on pdd and profiles

**VOXEL SIZE:** Figure 19 below demonstrates the effect of voxel size on both PDD and dose profiles. It was determined that using small voxel dimensions affect the surface dose. A difference of more than 10% is realized between the small voxel size and the medium or big voxel sizes. The effect on the profiles is more witnessed with big voxel sizes, where the shoulders become narrower and the penumbra much wider. With small voxels the profile is less flat and the percentage error of the highest doses is much larger than the other values. The maximum error of the highest doses exceeds 1% only with small voxels.

### Effect of voxel size on pdd



### Effect of voxel size on profiles

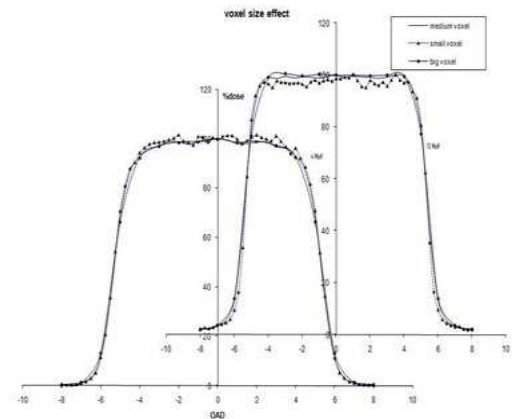


**FIGURE 19:** Effect of alterations of the size of voxels on pdd and profiles

### LINAC CONFIGURATIONS:

THE SCATTERING FOILS: The presence of the walls of the secondary scattering foils affects both Pdd's and beam profiles. More effect is noticed on the Pdd of the high energy (18 MeV). Dmax and the whole fall-off region are shifted towards the surface and the dose gradient is slightly increased when the walls were simulated using FLATFILT component module. The walls improve the flatness of the profiles, especially at the shoulder region. No effect is seen on the penumbra. This is illustrated in Figure 20 below.

## Effect of sec-scat walls on pdd

## Effect of sec-scat walls on profiles

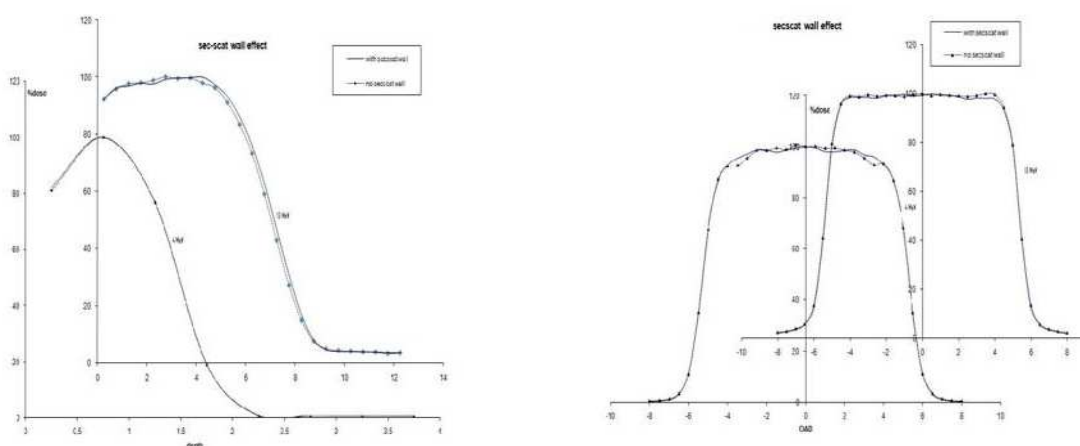
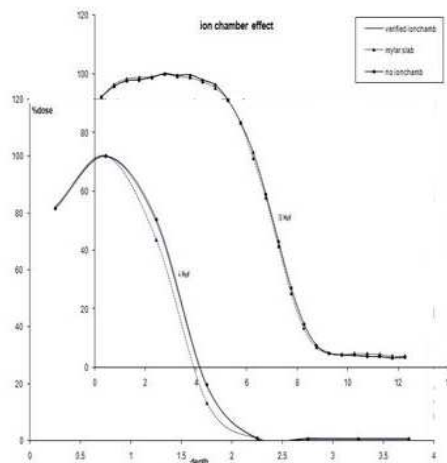


**FIGURE 20:** Effect of the secondary scattering foil walls on pdd and profiles

**THE IONIZATION CHAMBERS:** Little effect is seen on the PDD when simulating the Linac without the ionization chamber or when altering the thickness of its walls or when simulating it using CONSTAK rather than IONCHAMB CM for all energies. A big different though is noticed when simulating it using SLAB, especially for the low energy (4 MeV) beam. The whole fall-off region is shifted towards the surface and the dose gradient is slightly decreased. Regarding the dose profiles, a slightly higher dose is noticed around the central axis when simulating the Linac without the ionization chamber. SLAB option also causes depression of the profiles at the shoulder region. Less effect is noticed as the energy of the beam increases. The effect of alteration of the ionization chamber is illustrated in Figure 21 below for 4 MeV and 18 MeV.

## Effect of ionchamb on pdd



## Effect of ionchamb on profiles

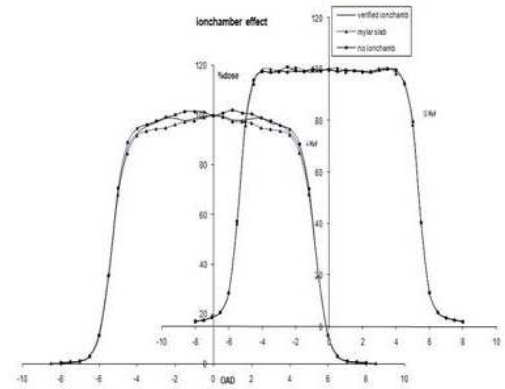
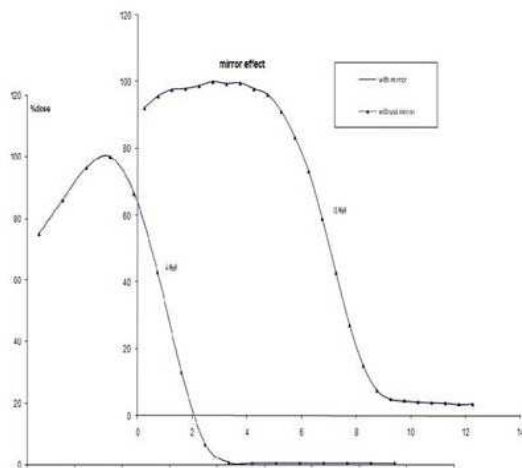


**FIGURE 21:** Effect of alterations of the ionization chamber design on pdd and profiles

**THE MIRROR:** The presence of the mirror does not affect high-energy beams. It slightly increased the surface dose of the PDDs for low energy beams without affecting the dose gradient. A slight depression in the shoulder region of the profile of the low energy beams is noticed when the Linac is simulated without the mirrors. No effect is realized on the penumbra as the result of absence of the mirror. Figure 22 below illustrates the effects of the mirror on the PDD and dose profiles for 4 MeV and 18 MeV.

### Effect of mirror on pdd



### Effect of mirror on profile

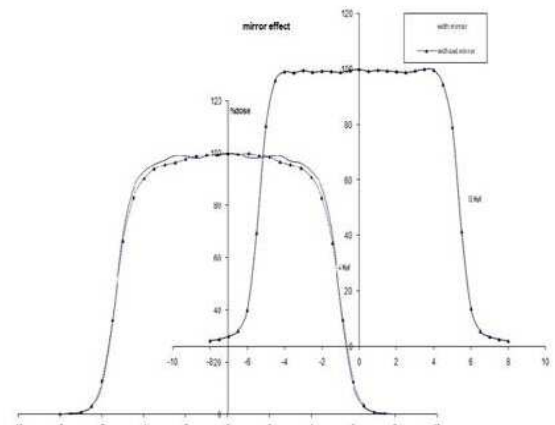
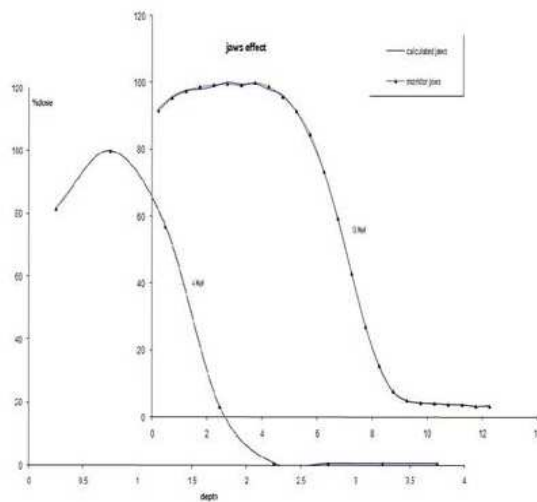


**FIGURE 22:** Effect of the mirror on pdd and profiles

The JAWS: The jaws opening obtained from the Linac monitor, referred to as monitor jaws slightly underestimates the surface dose of the PDD for low energy beams. No effect is noticed for higher energies, or in the fall-off region or Bremsstrahlung tail of any of the energies. More effect is realized on the dose profiles where “horns” are produced with the monitor jaws openings. The effects of the jaws opening are illustrated in Figure 23 below.

## Effect of jaws on pdd



## Effect of jaws on profiles

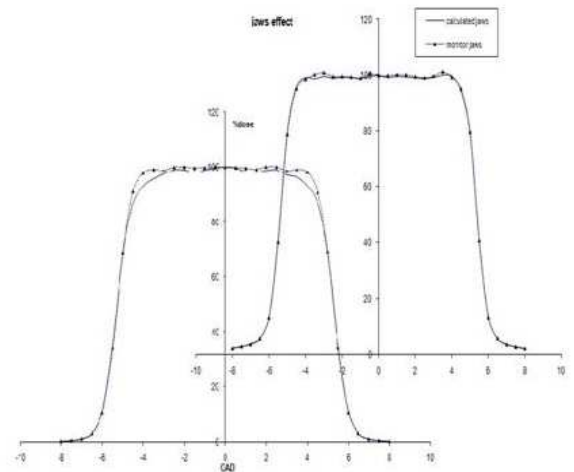
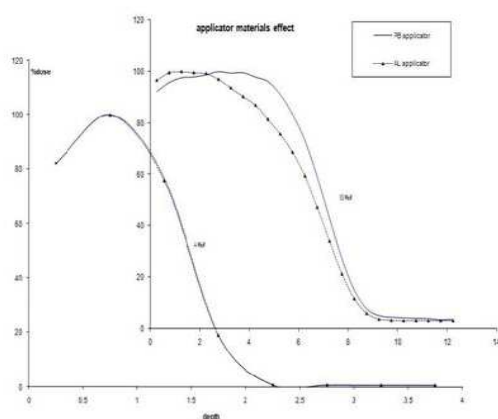


**FIGURE 23:** Effect of alterations of the jaws opening on pdd and profiles

**APPLICATORS:** The effect of the applicator materials is very evident for high energy electron beams as seen on Figure 24 below. Using Aluminum applicators completely deforms the PDD by reducing the “plateau” of uniform dose and decreases the dose gradient and decreasing the Bremsstrahlung tail. It also affects the dose profiles by reducing the dose near the central axis and increases the dose at the edges. Less effect is seen for the low (4 MeV) beam.

## Effect of applicators on pdd



## Effect of applicators on profiles

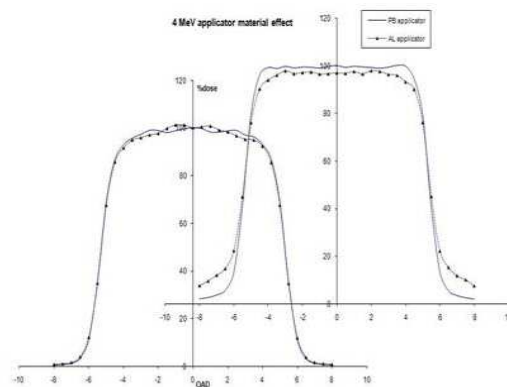


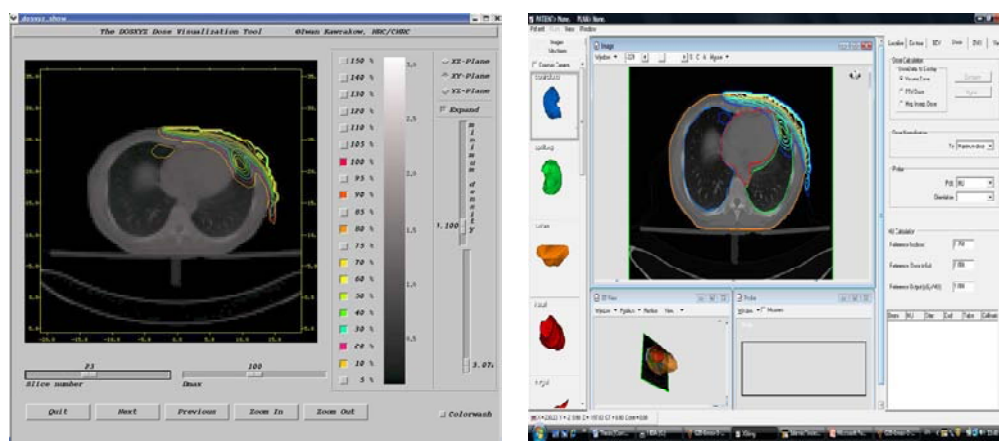
**FIGURE 24:** Effect of applicator materials on pdd and profiles



## 3.4 Electron Postmastectomy Radiotherapy

### 3.4.1 Verification of XSTING

6 MeV dose distribution by DOSXYZ\_show and XSTING



12 MeV dose distribution by DOSXYZ\_show and XSTING

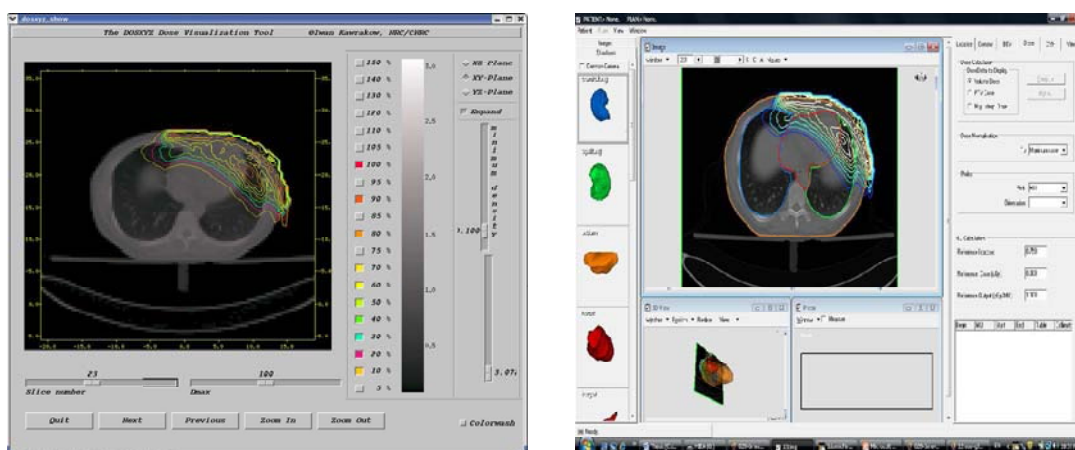


**FIGURE 25:** Isodose lines for 6 and 12MeV as given by DOSXYZ\_show and XSTING

From Figure 25 we can see good resemblance between the isodose distributions shown by the benchmarked DOSXYZ\_show and XSTING. There are minor differences in the dose patterns. These may be attributed to contouring algorithm, pixel resolution and slice sizes.

The comparison between the DVH of the ipsilateral lung and the 10% and 70% dose levels, both as 3D image and isodose lines can be seen in Figure 26 below

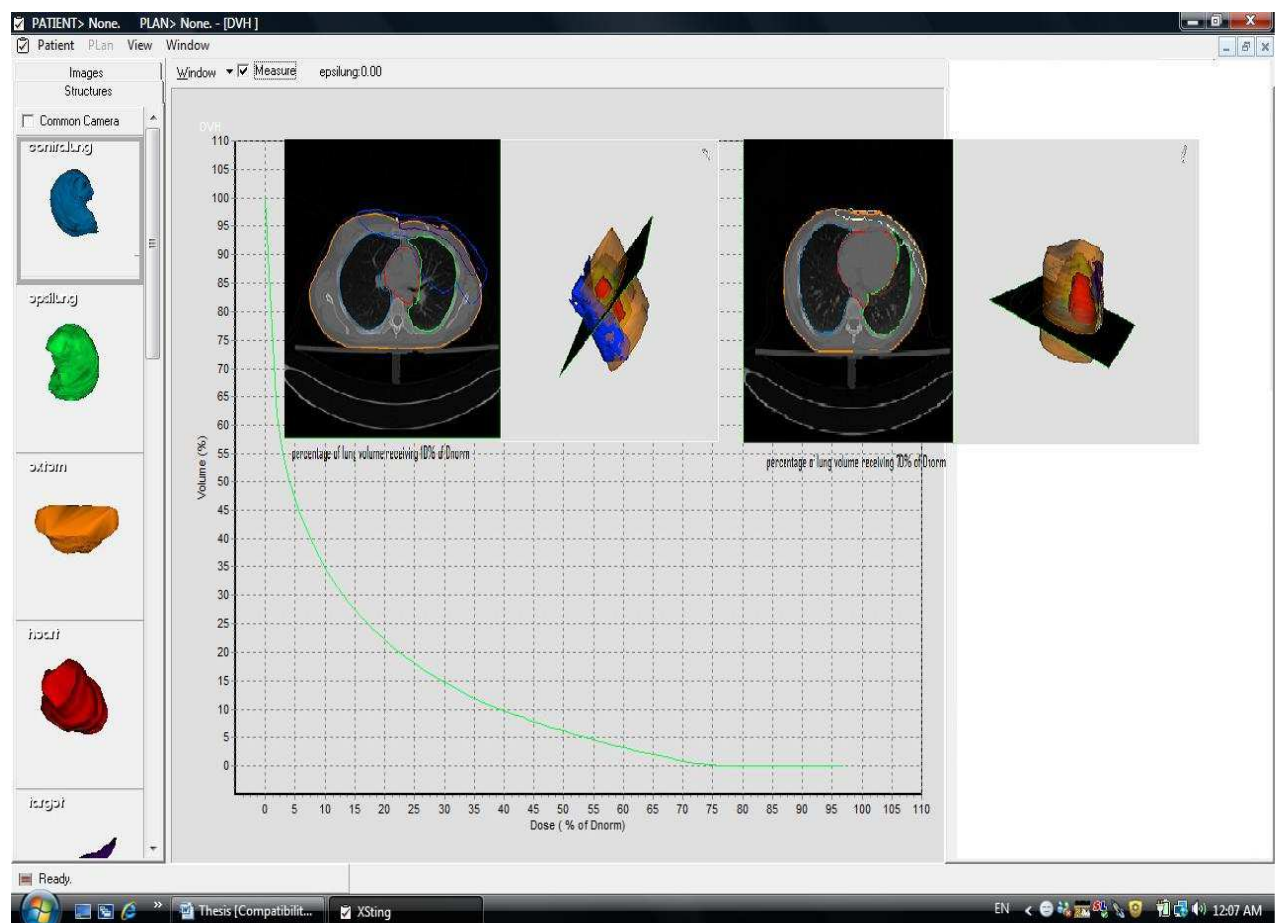


**FIGURE 26:** comparison between DVH values and isodose and 3D images receiving 10% and 70% of Dnorm

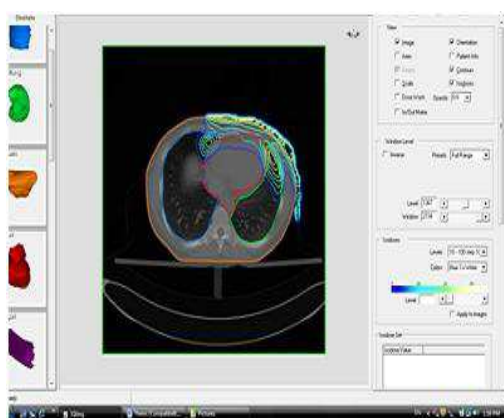
It can be seen from the isodose distribution and the 3D image that the volume of the lung receiving 10% of Dnorm is about one-third, which is in line with the DVH, which shows that 35% of the lung's volume receives 10% of Dnorm. Moreover, the isodose distribution and the 3D image reveal that a negligible percentage of the lung's volume

receives 70% of the dose, and this is also proven by the DVH, where about 1% of the lung is shown to receive 70% of  $D_{norm}$ .

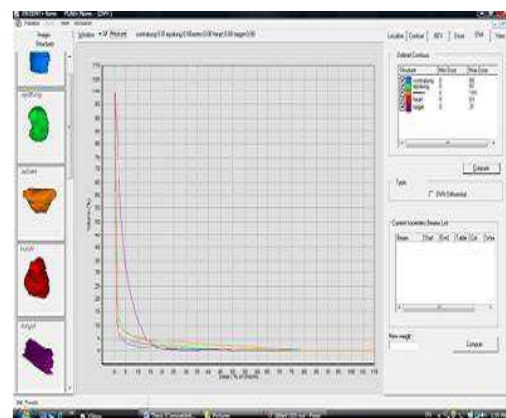
### **3.4.2 Electron Postmastectomy Radiotherapy**

#### **DVH Evaluation:**

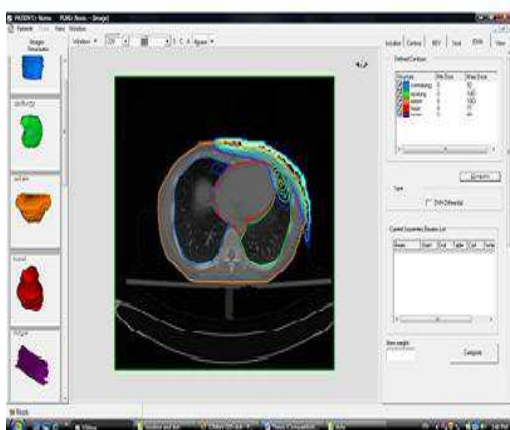
In the following figures the isodose distributions and mean cumulative dose volume histograms are shown for different energies and gantry angles. Considering the two dimensional DVH representation, the horizontal axis represents the percentage of the dose normalized to the maximum dose, while the vertical axis represents the percentage of the volume of the different organs; target, ipsilateral lung, heart, contralateral lung and extern, which is the external contour of the patient's body.



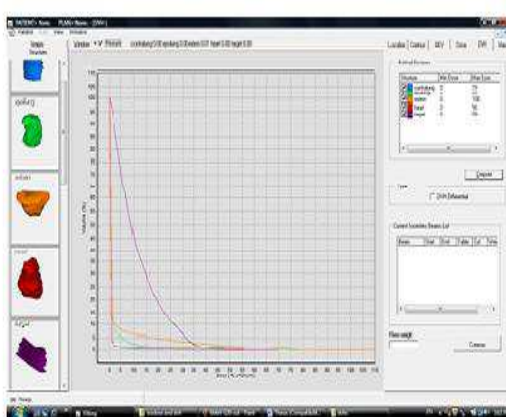
6 MeV G-10



6 MeV G-10

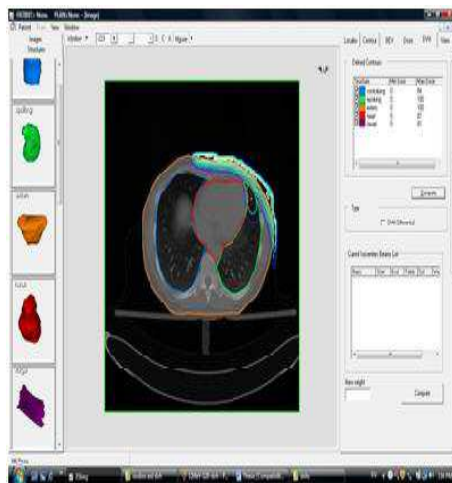


6 MeV G-20

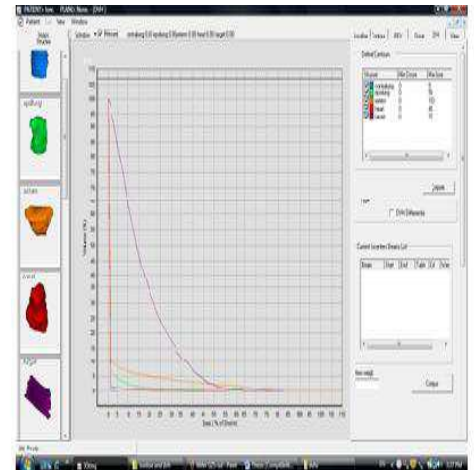


6 MeV G-20

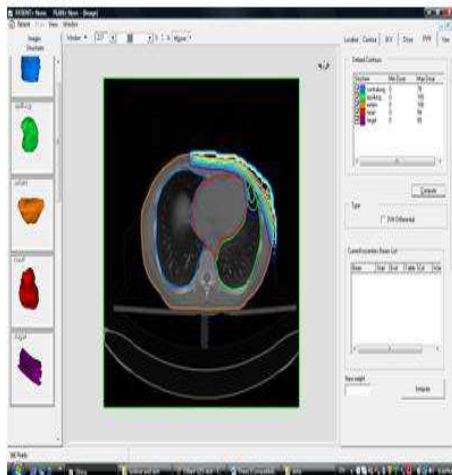
**FIGURE 27-a:** Isodose lines and DVH for 6 MeV gantry angles 10 and 20



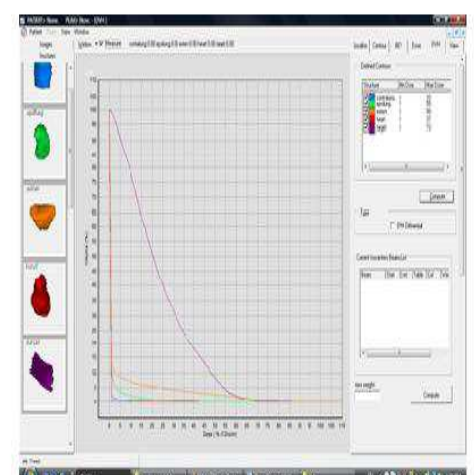
6 MeV G-25



6 MeV G-25



6 MeV G-30

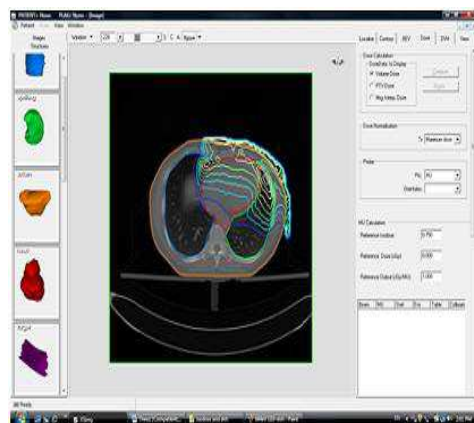


6 MeV G-30

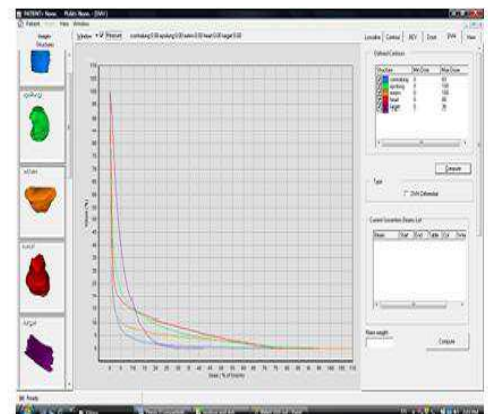
**FIGURE 27-b:** Isodose lines and DVH for 6 MeV gantry angles 25 and 30

From Figures 27 a and b it is realized that the lung and heart doses are very low for 6 MeV electron beams but the target coverage is rather poor regardless of the angle of irradiation, although it increases with increasing angles.

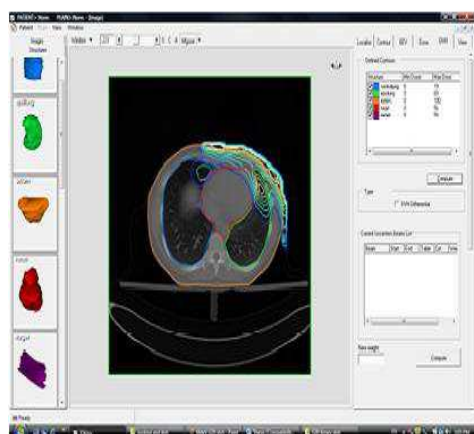




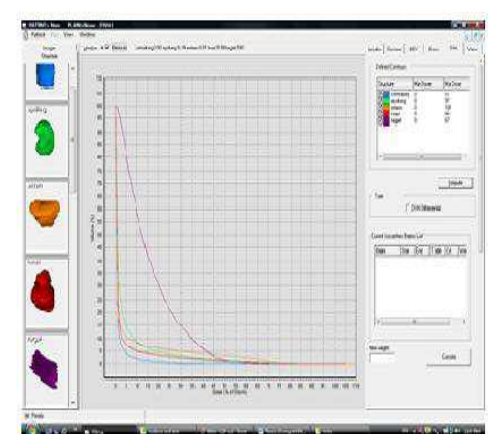
8 MeV G-10



8 MeV G-10

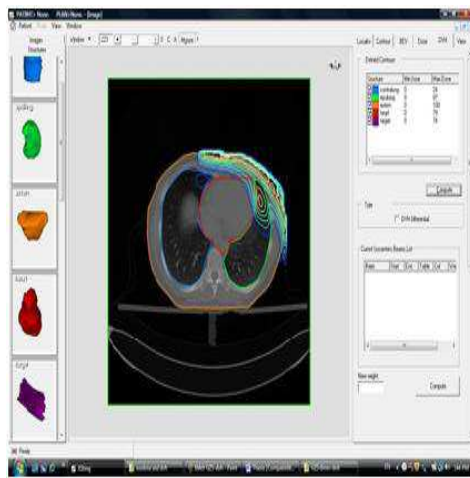


8 MeV G-20

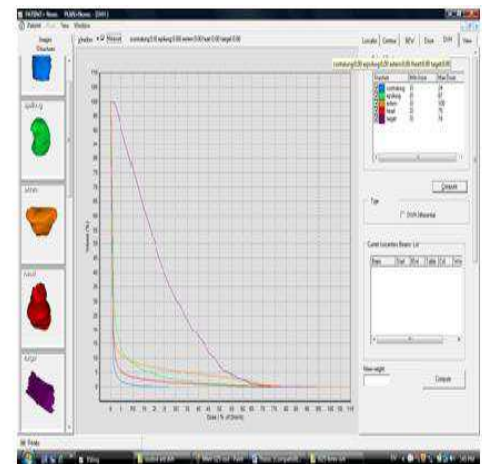


8 MeV G-20

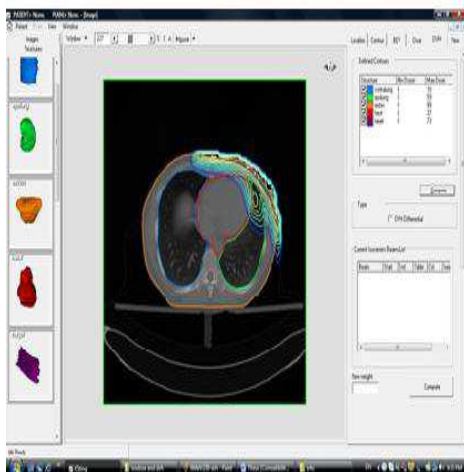
**FIGURE 28-a:** Isodose lines and DVH for 8 MeV gantry angles 10 and 20



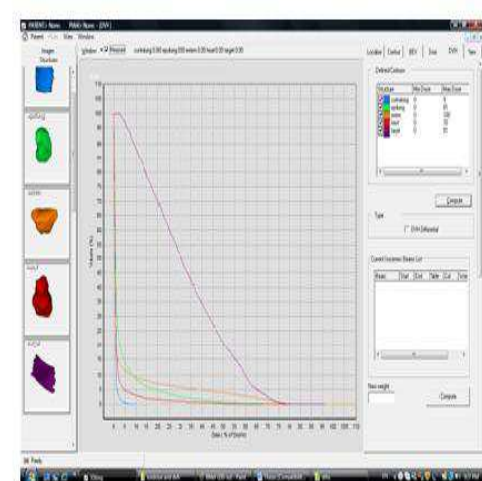
8 MeV G-25



8 MeV G-25

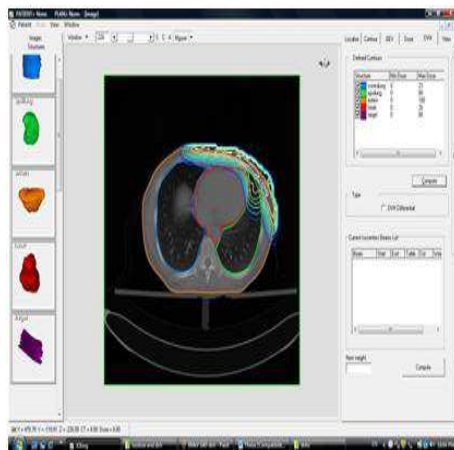


8 MeV G-30

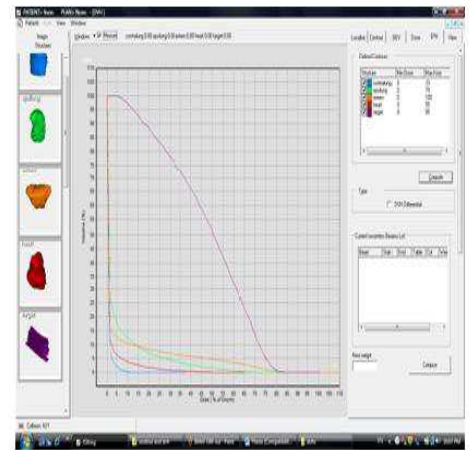


8 MeV G-30

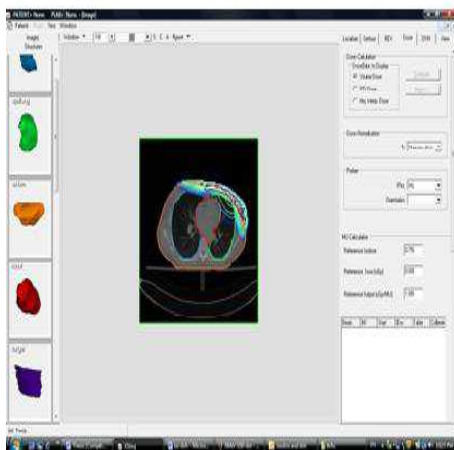
**FIGURE 28-b:** Isodose lines and DVH for 8 MeV gantry angles 25 and 30



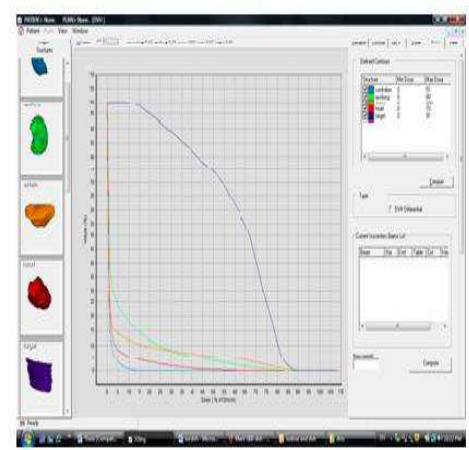
8 MeV G40



8 MeV G40



8 MeV G50

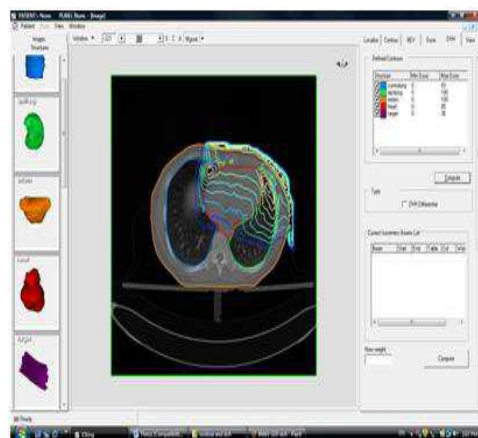


8 MeV G50

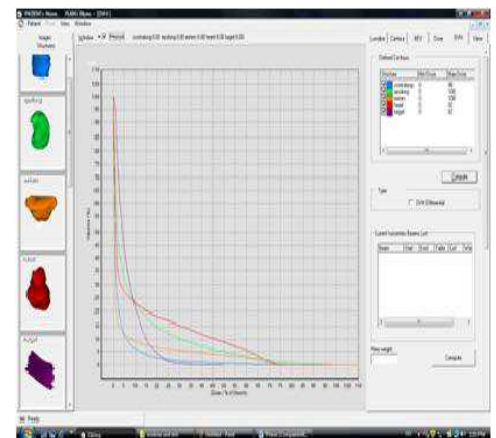
**FIGURE 28-c:** Isodose lines and DVH for 8 MeV gantry angles 40 and 50

From figures 28 a, b and c it is also realized that the doses at the organs at risk are low. The target coverage is very much improved at a gantry angle of 50 degrees, but it is still rather poor.

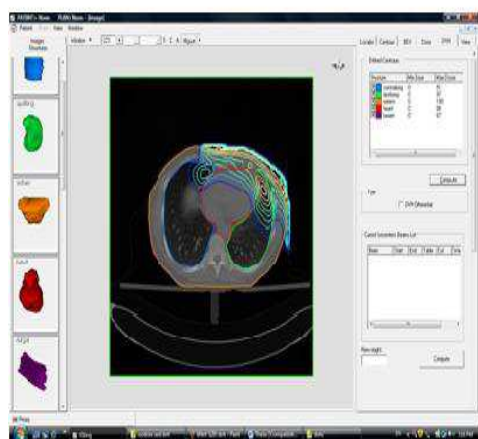




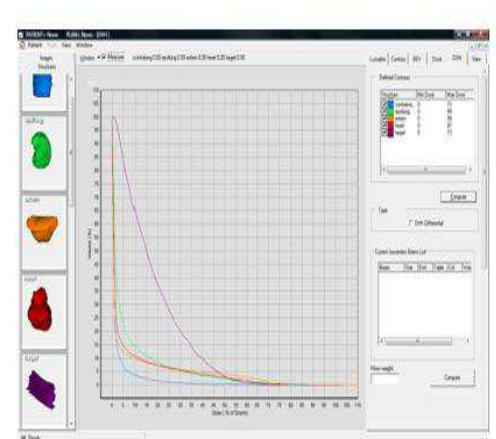
10 MeV G-10



10 MeV G-10

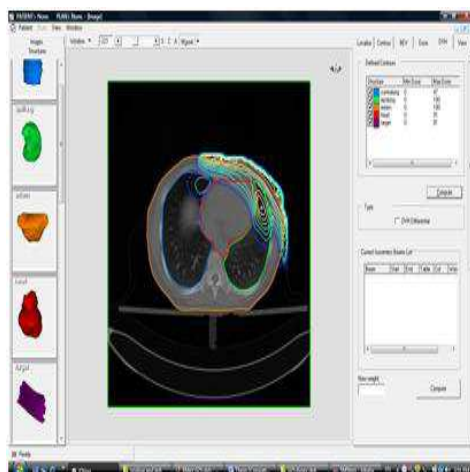


10 MeV G-20

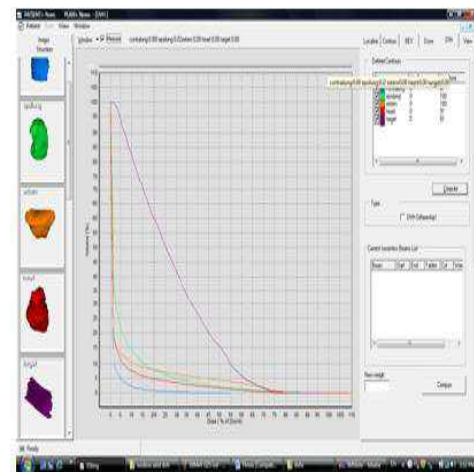


10 MeV G-20

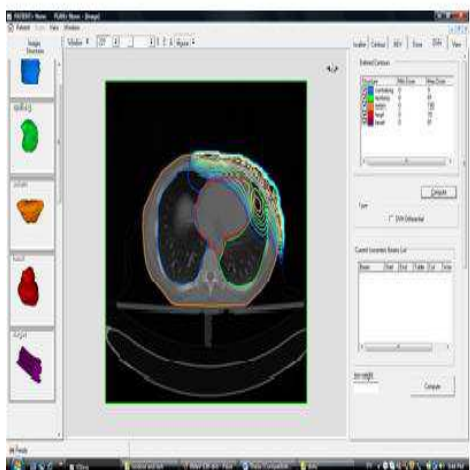
**FIGURE 29-a:** Isodose lines and DVH for 10 MeV gantry angles 10 and 20



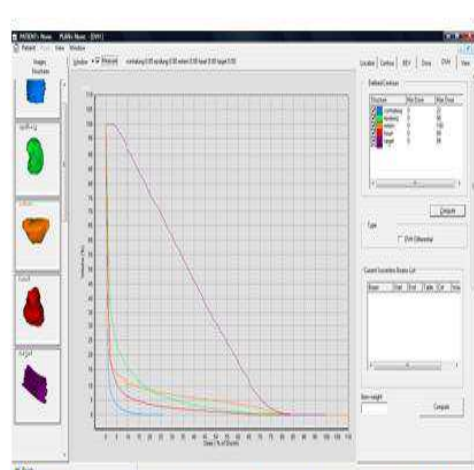
10 MeV G-25



10 MeV G-25

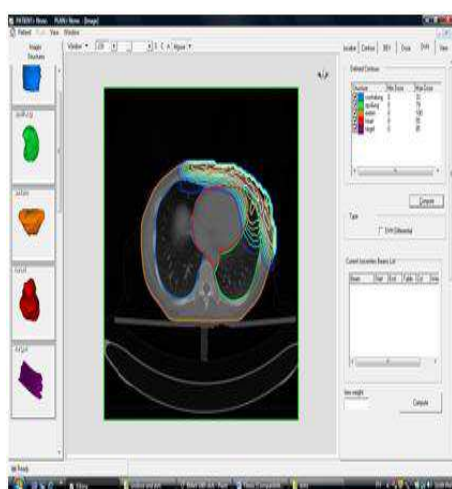


10 MeV G-30

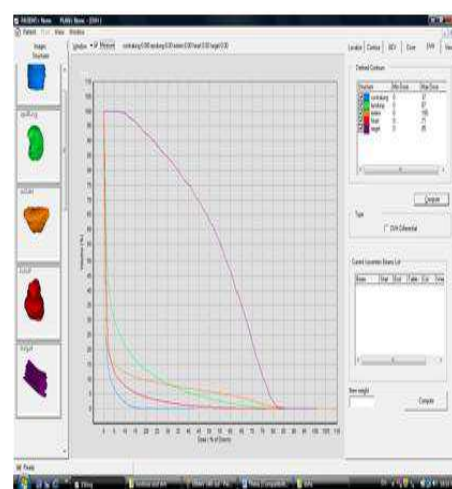


10 MeV G-30

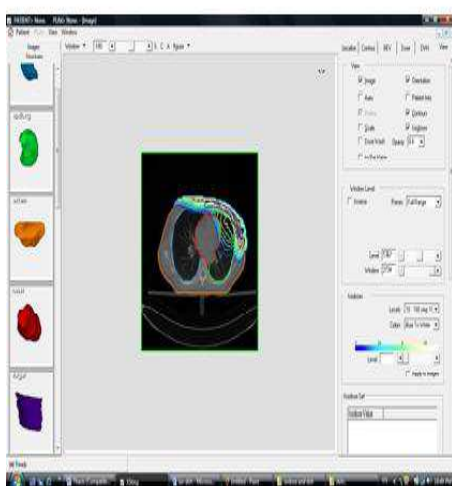
**FIGURE 29-b:** Isodose lines and DVH for 10 MeV gantry angles 25 and 30



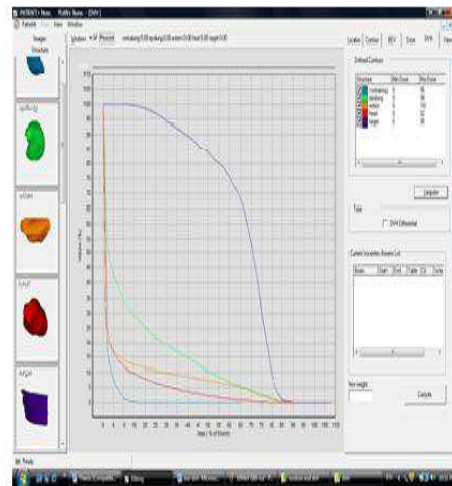
10 MeV G-40



10 MeV G-40



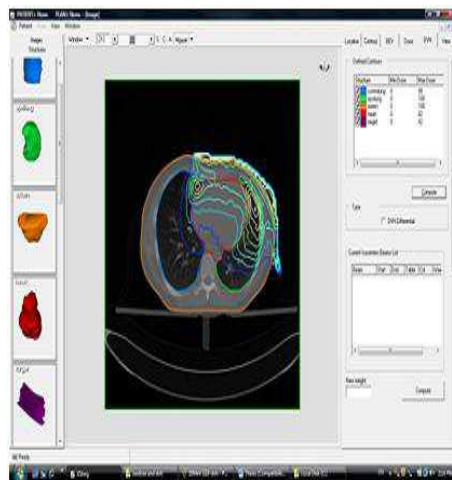
10 MeV G-60



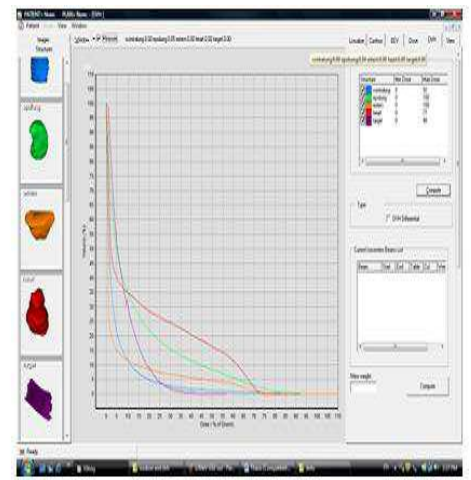
10 MeV G-60

**FIGURE 29-c:** Isodose lines and DVH for 10 MeV gantry angles 40 and 60

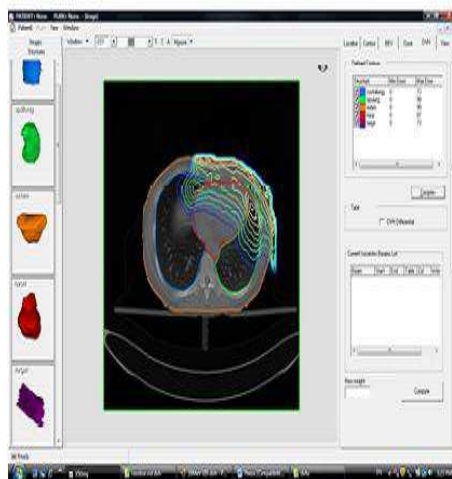
From figures 29 a-c, the heart dose increases very slightly with increased inclination. The dose at the ipsilateral lung also increases with increasing the gantry angle but V20 remains below 20% even for 60°, which is the maximum inclination tested. The target coverage improves with increasing the gantry angle and is much better than with the previous lower energies.



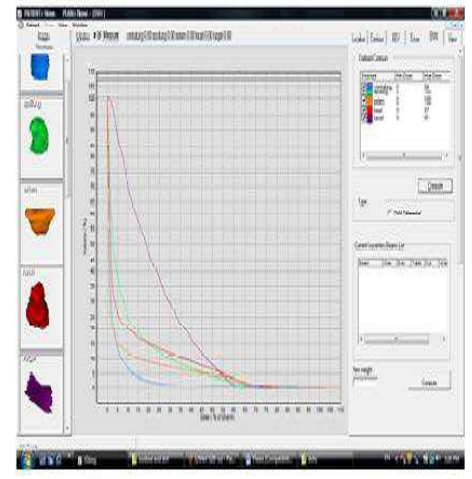
12 MeV G-10



12 MeV G-10



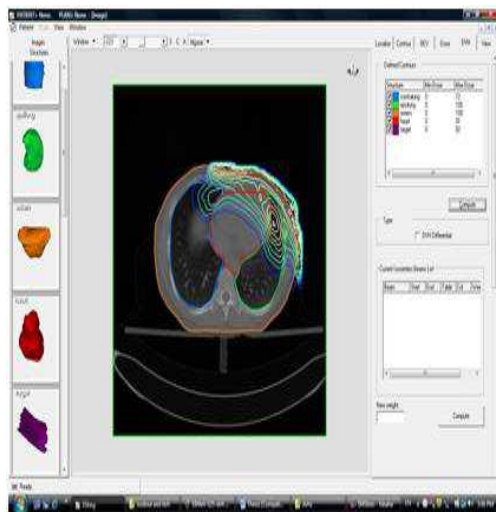
12 MeV G-20



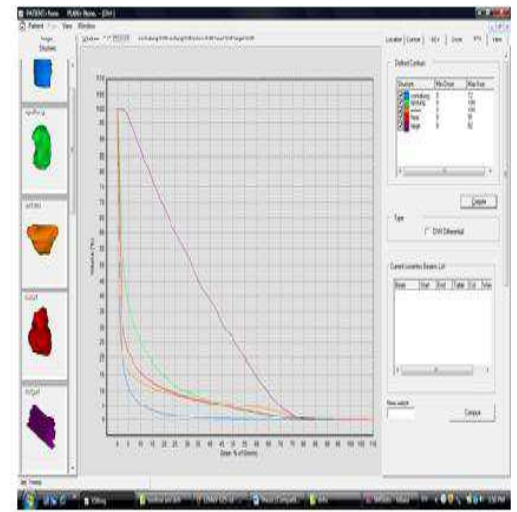
12 MeV G-20

**FIGURE 30-a:** Isodose lines and DVH for 12 MeV gantry angles 10 and 20

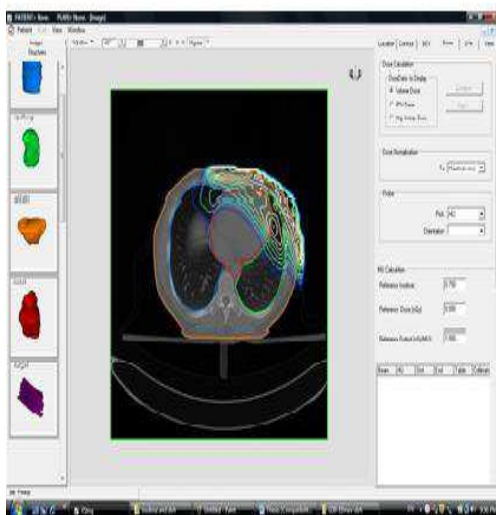




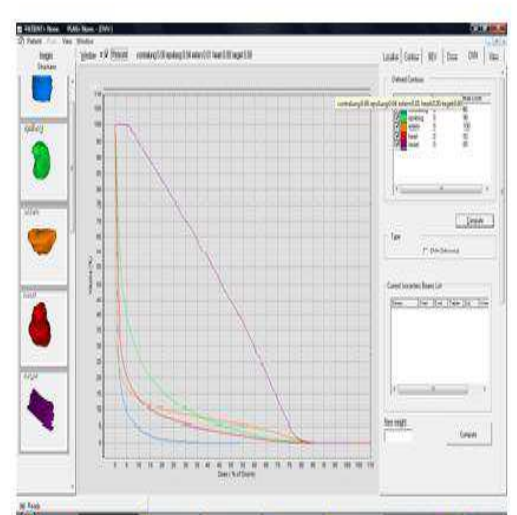
12 MeV G-25



12 MeV G-25

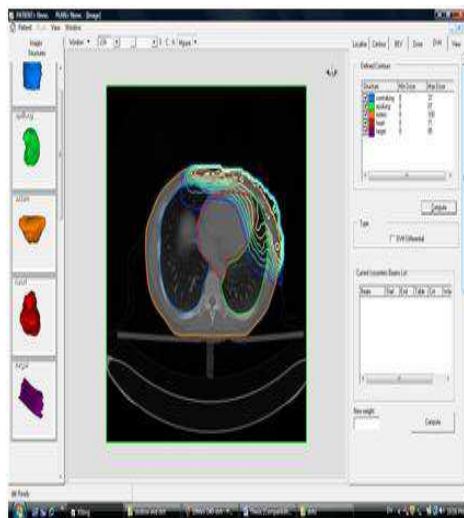


12 MeV G-30

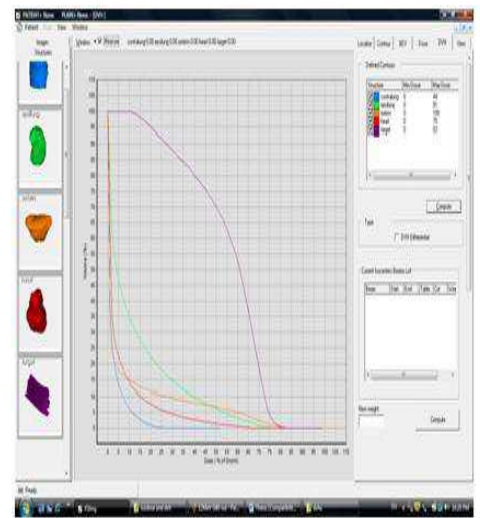


12 MeV G-30

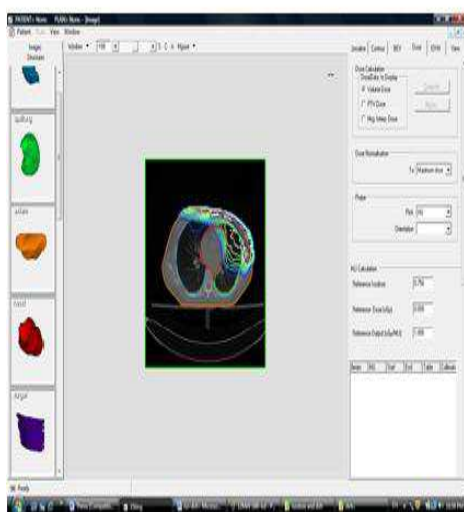
**FIGURE 30-b:** Isodose lines and DVH for 12 MeV gantry angles 25 and 30



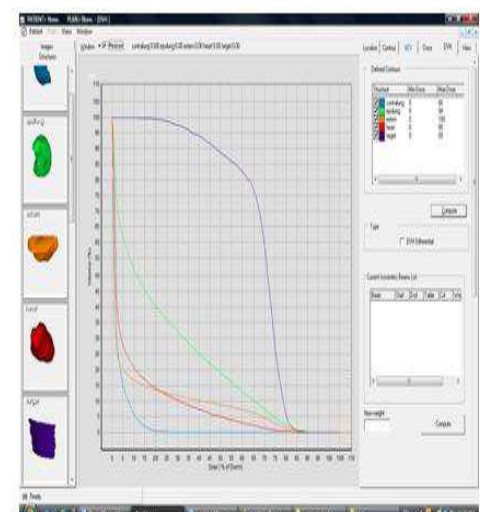
12 MeV G-40



12 MeV G-40



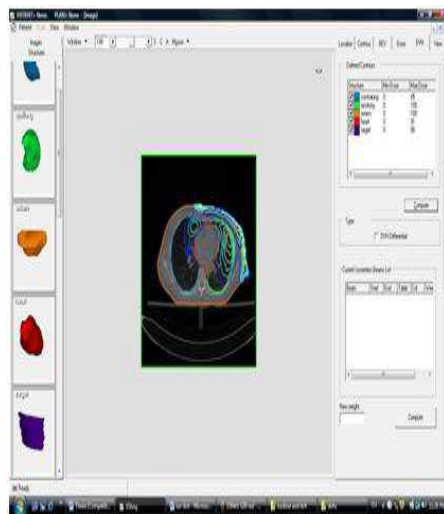
12 MeV G-60



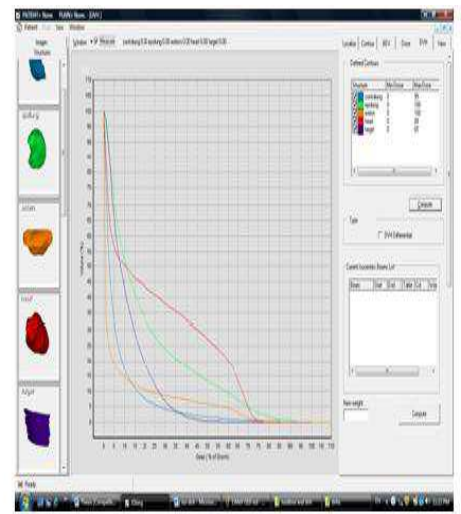
12 MeV G-60

**FIGURE 30-c:** Isodose lines and DVH for 12 MeV gantry angles 40 and 60

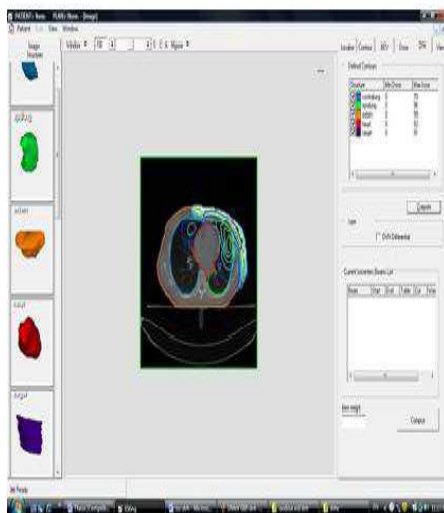
From figures 30 a-c, the heart dose slightly increases with an increase in the gantry angles. The lung dose also increases and V20 is about 24 Gy for gantry angle of 60 degrees. Target coverage increases with increasing the gantry angle.



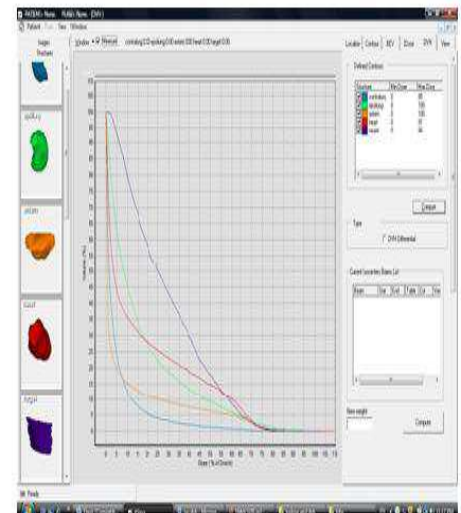
15 MeV G-10



15 MeV G-10

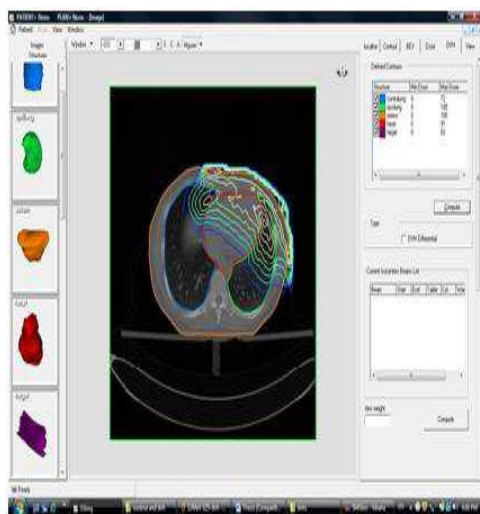


15 MeV G-20

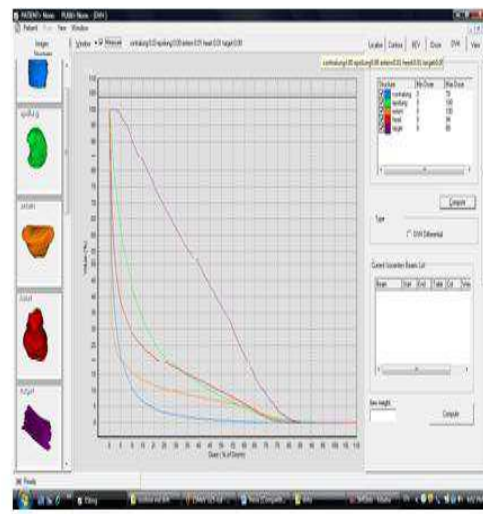


15 MeV G-20

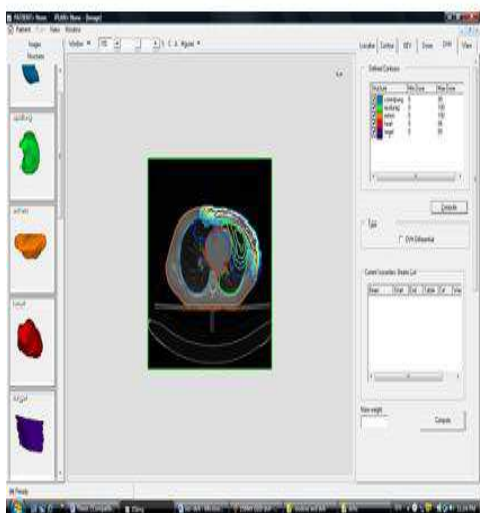
**FIGURE 31-a:** Isodose lines and DVH for 15 MeV gantry angles 10 and 20



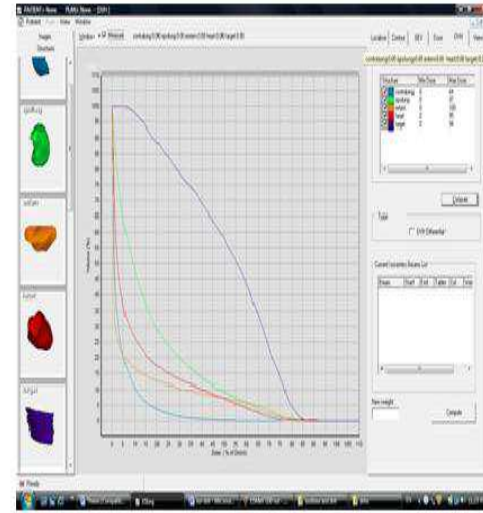
15 MeV G-25



15 MeV G-25



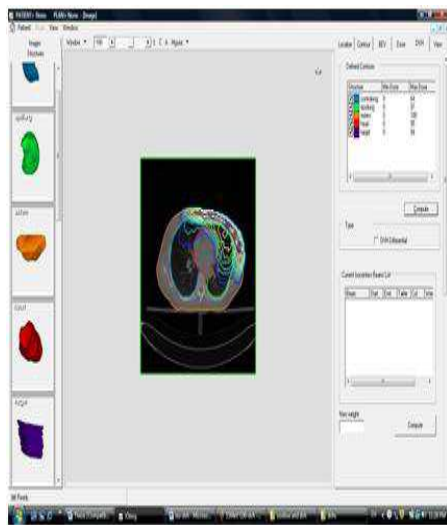
15 MeV G-30



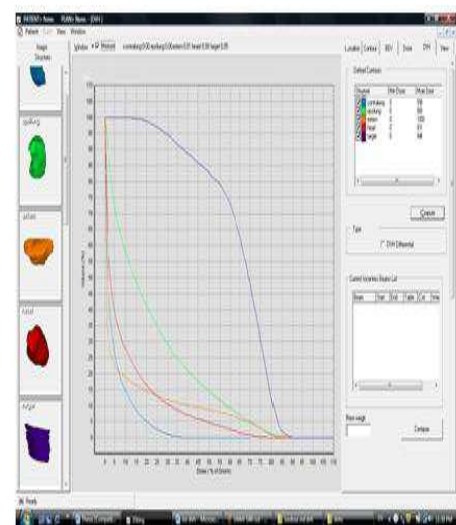
15 MeV G-30

**FIGURE 31-b:** Isodose lines and DVH for 15 MeV gantry angles 25 and 30

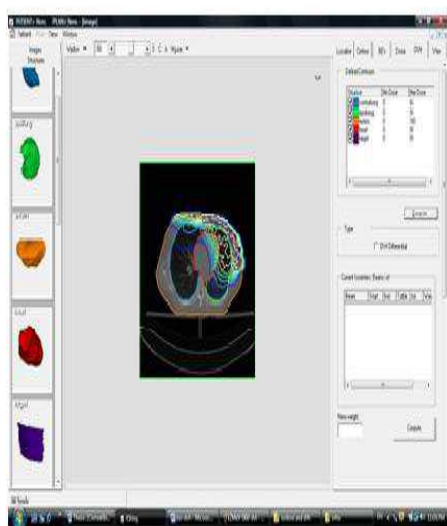




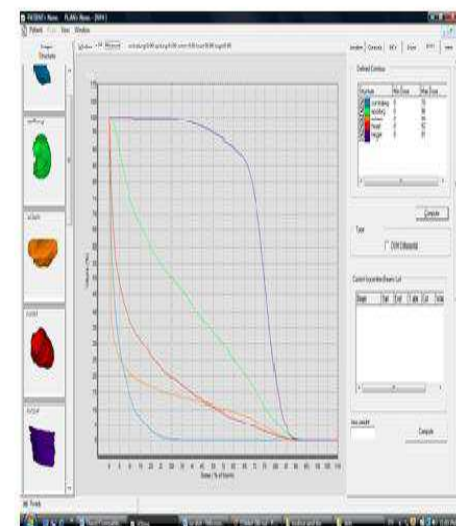
15 MeV G-40



15 MeV G-40



15 MeV G-60



15 MeV G-60

**FIGURE 31-c:** Isodose lines and DVH for 15 MeV gantry angles 40 and 60

From figures 31 a-c, it is realized that target coverage is excellent with 15 MeV, gantry angle of 60 degrees, but at the expense of the heart and, especially the epsilateral lung's dose, where V20 exceeds 25 Gy.

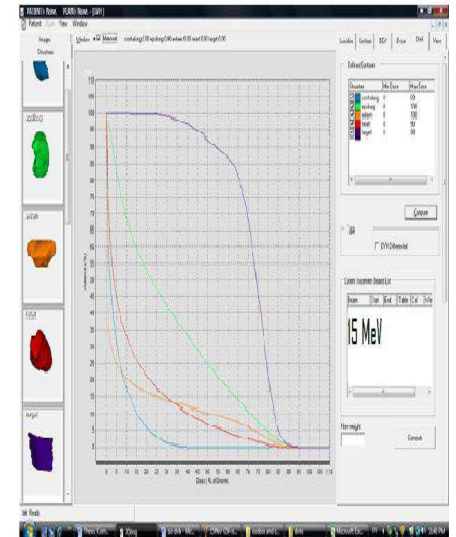
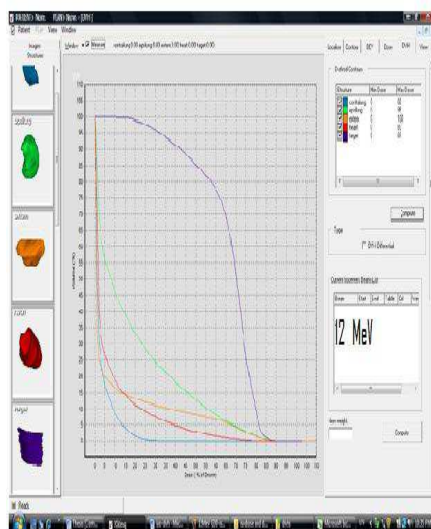
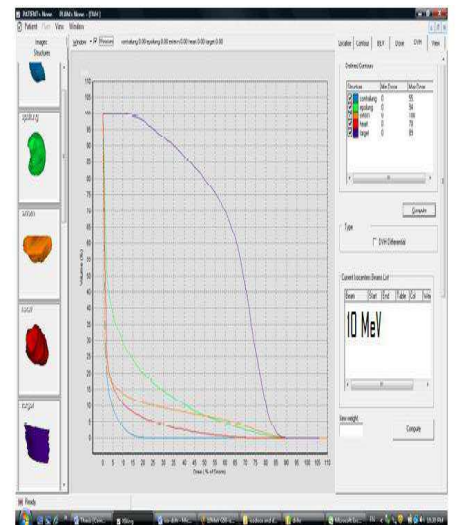
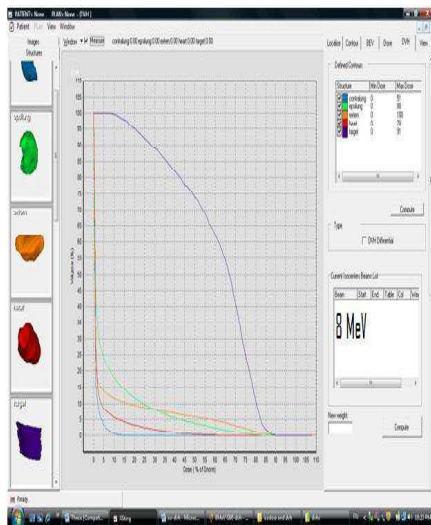


**FIGURE 32:** DVH for 8, 10, 12 and 15 MeV at gantry angle 50

In this figure, different energies 8, 10, 12 and 15 MeV are compared. It can be realized that target coverage as well as doses at organs at risk increase with increasing energies.

### Dose Response Evaluation using DORES

Dose response evaluation was performed using DORES for the lung. It was not possible to perform evaluation of the NTCP of the heart because this organ is still not an option in DORES evaluation. DVHs for the lung were exported from XSTING and loaded to DORES as explained in the previous chapter. Parameters for D50, n, and m were chosen from the LKB model and Seppenwoolde et al (2003) and a/b ratios of 3.1 (Dubray et al. 1995) and 4 (Bentzen et al. 2000) were chosen for lung fibrosis and pneumonitis respectively. The results of the runs are shown in figures 33 and 34 below.

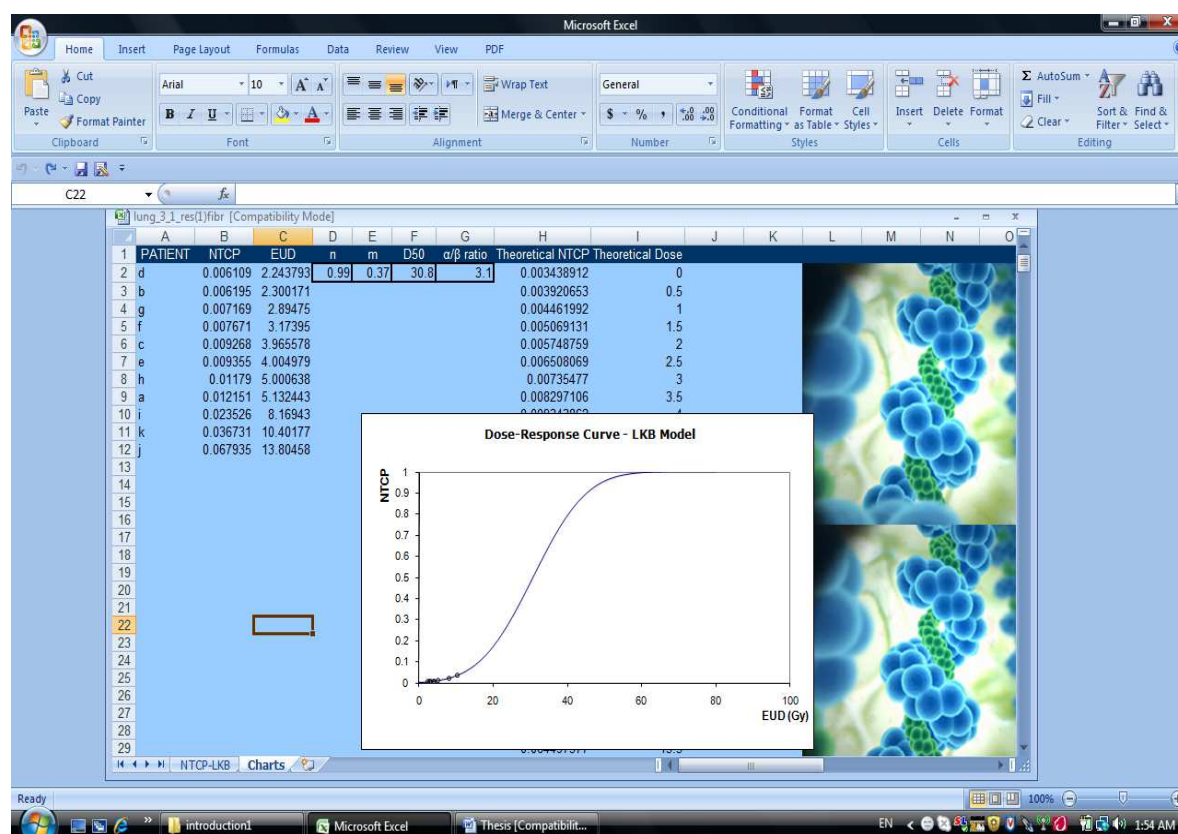


**FIGURE 33:** NTCP for lung fibrosis

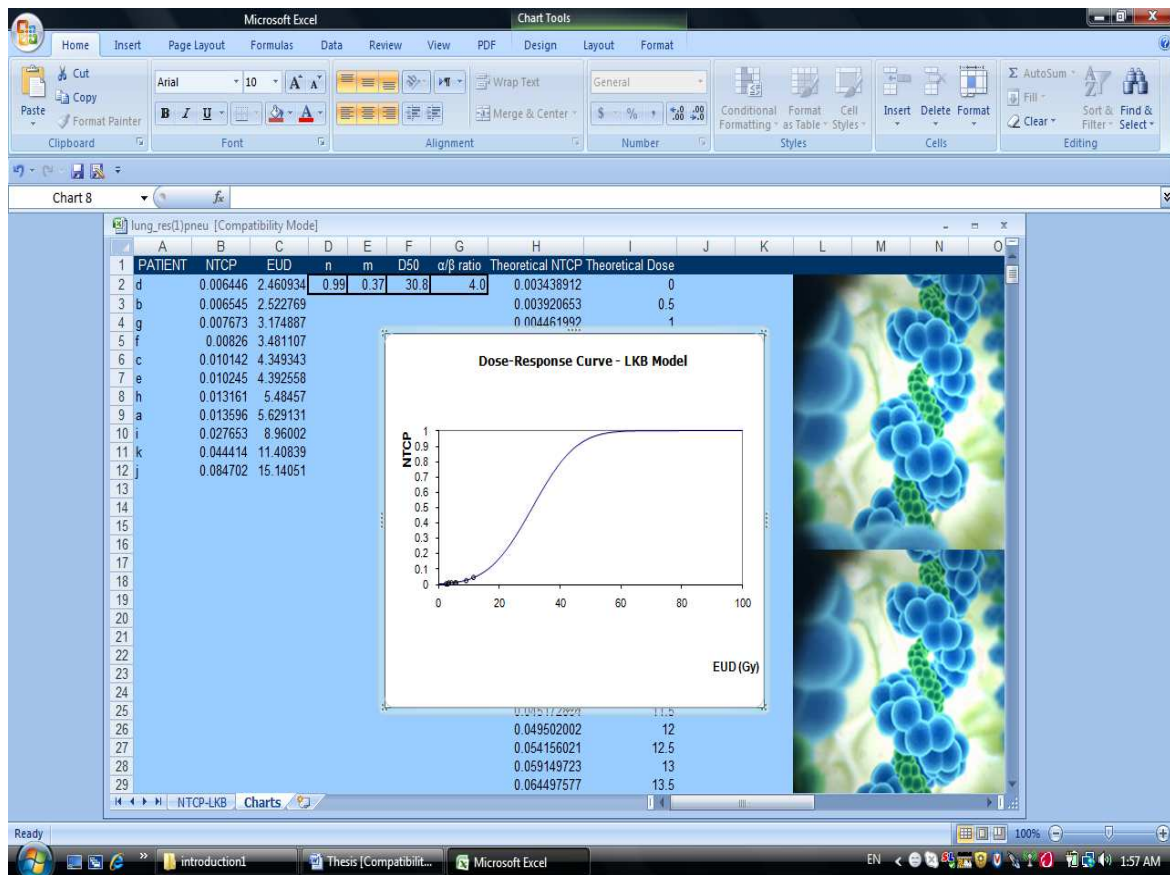


**FIGURE 34:** NTCP for pneumonitis

It can be seen clearly from these results that the risk of lung fibrosis and pneumonitis is fairly low. The maximum NTCP was for 15 MeV, as expected and as will be discussed later.

## **CHAPTER FOUR: DISCUSSIONS**

## 4.1 LINAC SIMULATION AND VERIFICATION:

Radiotherapy treatment-planning in general, and electron beam planning in particular, is very complex because electron scattering is strongly affected by changes in density and composition the patient. In addition, the incident energy and angular distribution are almost unknown [93]. Simulations of electron beams can be a tedious job because electron beams are very sensitive to the design and materials of the Linac components as was shown in this work. Detailed knowledge of the beam parameters and the Linac configurations are very essential for accurate simulations. Unfortunately many details are missing from the manual provided by the vendors and hundreds of runs based on trial-and-error were performed to reach to a satisfactory match between measurements and calculations.

Browsing pubmed one can find many studies on Monte Carlo studies using photons, for intensity modulated radiotherapy and even neutrons, but the number of studies on electron Monte Carlo is very limited. Some studies were performed on the evaluation of the effects of beam parameters and on the effect of field size and scattering foil design but there are no studies available guiding the researchers on the possible sources of errors in simulations and how to understand them from looking at the percent depth dose and off-axis dose profiles.

To reach a good match on the Pdd curves many trials were performed changing the energy of the beam and the energy width, or full width at half. The differences for the Pdd curves were more significant in the build-up region and especially at the surface. Possible contaminating neutrons, scattered electrons from the phantom, dependence on the measuring device, the choice of the effective point of measurements and other parameters could be responsible for this mismatch. The mismatch becomes much smaller as the beam energy increases. On the other hand a slight discrepancy between measurements and calculations is noticed at the fall-off region with higher energies. But, in general these differences are within the 2%-2mm range.

Regarding the off-axis dose profiles there was a good match between measurements and calculations. To get to this agreement a slight change in the jaws opening had to be made. The major discrepancy between measurements and calculations was in the right shoulder, where the measurements showed slight depression for some energies and field sizes. When one shoulder is apparently depressed and varies from the other one that is in a good match with MC calculations we consider that MC simulation was fulfilled.



## 4.2 Evaluation of sources of systematic errors in simulations

Accurate simulation of the beam parameters and linear accelerator configurations is very crucial for electron beams since slight alterations may affect the output dose distribution. This paper studies some of the effects caused by slight alterations on both percent depth dose and lateral dose profiles as summarized below.

**ENERGY DISTRIBUTION OF THE INITIAL BEAM:** The energy width of the electron beam that produces a good match between measured and calculated Pdd and dose profiles ranges from 20% to 30% of the most probable energy, depending on the energy. The percentage is higher for lower electron beam energies. An increase in this value affects the flatness of the beam profiles and a decrease may increase the dose gradient resulting in miss-match between the measurements and calculations.

**SOURCE TO SURFACE DISTANCE (SSD):** When electrons are simulated for clinical applications the actual SSD should be accounted for because slight alterations were found to influence the surface dose as well as the lateral dose distributions.

**VOXEL SIZE:** Voxel sizes of  $0.5 \times 0.5 \times 0.5 \text{ cm}^3$  seem to give a better match between measured and calculated data. Decreasing the voxel size increases the uncertainty because fewer particles deposit dose in a small volume. Increasing the voxel size reduces the uncertainty but may introduce errors due to reduced spatial resolution. This is seen clearly in the results where the dose at the edges was not accurately measured.

Table 3 below summarizes the effects of slight alterations of input parameters

IP/effect	PDD- surface dose	PDD- Dose gradient	PDD- Bremsst. tail	Prof- penumbra	Prof- flatness
Increase FWHM	No effect	Sharp decrease	Slight increase	No effect	Increase
Increase SSD	Slightly reduce for higher energy	No effect	No effect	increase	No effect
Voxel size	Reduced by 10% with small voxel	Sharp decrease with increase voxel size	No effect	Wider with big voxels	Best for medium voxels

**Table 3:** Summary of effects of input parameters (beam/phantom)

### LINAC CONFIGURATIONS:

THE SECONDARY SCATTERING FOILS: FLATFILT component module is recommended for simulating the secondary scattering foils because it allows simulating the foils for different energies and includes the walls. The walls of the secondary scattering foils were found to influence the dose distributions especially for higher energies electron beams, where walls can be simulated with FLATFILT.

THE IONIZATION CHAMBERS: Although IONCHAMB component module does not account for the difference in the materials of the inner walls, it allows accurate simulation of the ionization chambers as shown in the results. The segmentation of the ionization chamber reduces scatter effects [21]. This is probably why simulating the ionization chamber as a SLAB of Mylar had more influence on the PDD than not simulating it at all. Absence of this component module did not have a big influence on the PDD but reduces the flatness of the beam profiles. This it is important to accurately simulate the ionization chambers.

THE MIRRORS: It is necessary to accurately simulate the mirrors for low energy electron beams because despite its thin nature, it can affect the scattering of the low energy beams. Mirrors do not affect the moderate or high energy beams.

THE JAWS: The jaws opening values obtained from the Linac monitor, referred to as monitor jaws are bigger than the calculated openings, especially for 4 MeV. This results in more scattered radiation at the edges of the beam. It is thus necessary to calculate the jaws openings according to the required field size.

APPLICATORS CONFIGURATIONS: The applicators play the most important role in beam shaping and have a major role in dose distribution due to their scattering effects on the electron beams at the water phantom. The amount of scattered radiation from applicators is dependent on the applicator design and materials. Applicators made from high Z materials such as lead are the ones of choice especially when dealing with high electron energies. Low Z materials such as aluminum can be used only for low energy electron beams.



Table 4 below summarizes the effects of slight alterations of Linac configurations

IP/effect	PDD- surface dose	PDD- Dose gradient	PDD- Bremsst. tail	Prof- penumbra	Prof- flatness
With sec. Scat. walls	Increase for low energy	Slightly increase for high energy	No effect	No effect	Increase
ion chamber	No effect	Decrease with mylar slab for low energy	No effect	No effect	Decrease with mylar slab
With Mirror	Slight increase for low energy	No effect	No effect	No effect	Increase
Jaws at monitor	Slight decrease for low energy	No effect	No effect	No effect	Decrease
Al applicator	Increase for high energy	Decrease for high energy	Decrease for high energy	Increase for high energy	Decrease

**Table 4:** Effect of Linac configurations

To summarize this Simulation of low energy beams was found to be more sensitive to the components that lie perpendicular to the direction of the beam even the very thin mirror, while high energy electron beams are more influenced by alterations at the edges of the beam like the walls of the scattering foils and the applicators.

Percent depth dose curves on the other hand are more influenced by accurate modeling of the different parts of the linear accelerator, especially at depths below Dmax. Little effect is noticed as a result of altering the beam parameters on the percent depth dose before Dmax. Beam and phantom input parameters, as well as some Linac components like scattering foil walls, jaws opening and material of the applicators affect the off-axis dose distributions by altering the side scatter.

## 4.3 Electron Postmastectomy Radiotherapy

### 4.3.1 XSTING

Radiotherapy research lacks a flexible computational research environment for Monte Carlo and patient-specific treatment planning. XSTING is a powerful tool and a useful addition to Monte Carlo research at the Medical Physics Department. XSTING has much useful functionality. It has the ability of producing accurate dose distribution curves

and generating accurate accumulative or differential dose volume histograms. This is clearly seen from figures 25 and 26. Moreover, the ability to export the DVHs to EXCEL file allows further utilizations of the result, for example for dose response evaluations. It can also be used to compare different studies using a variety of modalities, energies and field sizes.

XSTING is an efficient and fast tool. A certain study, including importing a patient's CT data, importing 3dd dose file from Monte Carlo studies and calculating the dose distribution and DVH for several regions of interest takes about 15 minutes, if the organ contouring is previously made and imported for the particular study. Contouring is the most time consuming procedure and may take a few hours to contour three or four organs but using XSTING it is not necessary to contour all slices of the CT scan. XSTING has the ability of auto-contouring some slices if the previous and following ones were contoured. The time for calculating the dose distribution is reduced if different 3dd files were used for the same patient because the voxels where the doses are calculated do not need to be re-created.

Similar to the GUI implemented in BEAM and its utilities, a user with limited or no computation skills can use XSTING. It is a user-friendly environment with straight forward applications.

### **4.3.2 Electron Postmastectomy Radiotherapy**

The radio-therapeutic doses received by the patient are limited by the tolerance of the normal tissues. Radiation is an unusual toxic agent, because the time of expression of cellular injury can be very variable from one tissue and tumor to another. Moreover, different patients given a standardized treatment can exhibit a range of normal tissue reactions. Thus, there is both dose dependence and variability in individual radio-sensitivity [47].

The risks and benefits of postmastectomy radiation treatment for breast cancer patients has been one of the most comprehensively studied topics in all of oncology. Multiple studies have indicated that radiation reduces the relative risk of local-regional recurrence by 65%-75% as discussed in details in chapter one. The harmful effects of radiation on healthy organs counterbalance this reduction.

The lung and the heart are important dose limiting organs for radiation therapy of tumors in the thoracic region. The risks of pulmonary and cardiac toxicities depend on many factors amongst which are the volumes of organ irradiated by a certain threshold dose. The concept of the volume effect is observed when large volumes of organ tissue are

irradiated. When large volumes of tissue are irradiated a decline is seen in the functional ability of an organ, where as the tissue sensitivity per unit volume is not affected. The radio-sensitivity of each individual cell in a tissue is not increased if the irradiated volume increases but the overall functionality or clinical tolerance is strongly affected.

The estimation of the radiation induced risks of today's breast radiotherapy requires the development of reliable dose-response relationships, which, in turn, require detailed organs at risk OAR dosimetry of past regimens given to women for whom long-term follow-up data is available. For example, at present, few heart dosimetry data from breast cancer radiotherapy are available. Furthermore, it is unknown which quantitative measures of the heart dose or volume is most relevant to subsequent heart disease risk. Studies have used a variety of heart dose specifications, including the absorbed dose, biologically effective dose (BED), and the "cumulative radiation effect" (an estimate of the biologic radiation dose). Published data recording the percentage volume of the heart irradiated to various doses are limited. Such information might, however, be important in assessing radiation-related heart disease, because the percentage volume of the heart irradiated to a certain "threshold" dose might be a better predictor for cardiac death than, for instance, the mean heart dose or BED. Information is also needed concerning the effect of irradiating different cardiac structures, especially the coronary arteries. Coronary artery doses have been reported for several techniques, but only for left-sided irradiation; however, most studies have reported only the mean dose to the whole heart. [56] In recent studies evaluating the dose-volume effect for the lung and heart, a contributing risk factor for the development of pneumonitis was found to be the volume of the lung irradiated [13, 94]. Graham et al. [95] showed a lung V20 (volume that received 20 Gy) to be an independent and significant predictor of GRADE2 or greater pneumonitis. The authors suggested that if V20<25% the risk of pneumonitis is low. Moreover, V30 was observed by Gagliardi et al. [96] to be the threshold for calculated risks of ischemic heart diseases. V45 was associated with pathologic data that suggest the development of coronary vessels stenosis [39].

The dose-volume effects on the lung and heart were included in this study. Isodose distributions and DVH values were obtained for different electron energies and field sizes for the target, the lungs and heart. In the previous chapter, results for 20X20 field sizes are displayed. This is because smaller field sizes did not provide sufficient coverage of the target area, which is wider than 14 cm. The following summarizes the effects of different energies and gantry angles on the target and the organs at risk.

**The target:** the target coverage was poor for 6 MeV and 8 MeV regardless of the gantry angle. This is because these electron energies are too weak to penetrate to the

chest muscles included in the target volume. The situation is somewhat better for Gantry angle 60 degrees. The target coverage is improved with increasing energies and angles as can be seen from the above results.

**The lung:** the dose at the ipsilateral lung increases with energy and gantry angle. The percentage of the volume that receives above 20 Gy, on a 50Gy treatment basis V20 exceeds 20% only with 12 MeV gantry angle 60 degrees and 15 MeV gantry angles 40, 50 and 60 degrees. But if the whole lung volume, including the contralateral lung is considered, the parameter V20 =20% is not exceeded. The dose at the contralateral lung is very limited regardless of the energy or angle of inclination.

**The heart:** the dose-volume effect at the heart decreases with increasing the gantry angle, although the maximum dose at the heart slightly increases. It is apparent from the results that the heart dose is more influenced by the gantry angle than the energy of the beam.

It is realized from figures 27 to 31 that the volume of the lung that receives low dose of radiation increases with the energy and decreases with gantry angle for low energy electron beams, but is not affected by the gantry angle for high-energy electron beams. For 15 MeV electrons, almost the entire lung receives low doses. Moreover, the volume of the heart that receives low doses of radiation increases with energy and decreases with gantry angles. Large volumes of organs at risk were associated to long term effects like secondary malignancies. This is still a subject of much debate. Any health effect directly linked to low-dose radiation exposure must have molecular/biochemical and biological bases. For low dose radiation to be carcinogenic a low-level acute, or even a chronic, exposure of ionizing radiation must bring about all the different mechanisms (mutagenic, cytotoxic, and epigenetic) and genotypic/phenotypic changes needed to convert normal cells to an invasive, malignant cell, given all the protective, repair, and suppressive systems known to exist in the human body. The prevailing paradigm that ionizing radiation brings about cancer primarily by DNA damage, and its conversion to gene and chromosomal mutations, drove the interpretation of radiation carcinogenesis. Trosko et al. (2005) states the facts both that epigenetic events play a major role in carcinogenesis and that low-dose radiation can also induce epigenetic events in and between cells in tissues. [97] This is contradicted by Tubiana (2009) who suggests that the high efficacy of defense mechanisms against radiation carcinogenesis, particularly when the tissue is not disorganized, can explain the lack of carcinogenic effect of contamination by small doses of radium or thorium, which has been observed on radium dial painters or in patients injected with thorotrast [98].

For this specific patient, it can be noted that the most suitable treatment is with 10 or 12 MeV at 40-50 degrees gantry angles. This is not to be generalized for all patients because the appropriate energy and gantry angles depend on the thickness of the chest wall as well as the geometry of the patient. But it seems that a single beam cannot provide appropriate target coverage regardless of the energy of the beam or the gantry angle.

### **Dose Response evaluation using DORES**

The aim of radiotherapy is to deliver enough radiation to the tumor to destroy it without irradiating normal tissue to a dose that will lead to serious complications (morbidity). The principle is usually illustrated by plotting two sigmoid curves, one for the tumor control probability (TCP) and the other for the normal tissue complication probability (NTCP). The optimum choice of radiation dose delivery technique in the treatment of a given tumor is such that it maximizes the TCP and simultaneously minimizes the NTCP. For a typical good radiotherapy treatment,  $TCP \geq 0.5$  and  $NTCP \leq 0.05$ . [99]

The further the NTCP curve is to the right of TCP curve the easier it is to achieve the radio-therapeutic goal, the larger is the therapeutic ratio and the less likely will it be that the treatment causes complications.

There is a number of calculation steps involved in determining NTCP, and these are complex, making the risk of errors high. Furthermore the real time taken for a manual computation is substantial restricting the possibility of a making quick treatment plans evaluation. The availability of software that can accurately and efficiently calculate these values enhances analytic dose response studies. Using DORES the average time taken to compute the NTCP for a single patient and produce an associated dose-response plot is 5.6 sec. Consequently sets of patients can be analyzed rapidly allowing for an inter-comparison of their associated dose-response. By knowing the clinical outcome for each patient's treatment DORES can be used as a post irradiation analysis tool, to evaluate the ability of the dose-response models in accurately foreseeing a specific level complication. Combined with a similar TCP evaluation, treatment plans can be optimized to ensure accurate dose delivery to tumors and minimal normal tissue complication [84], [100].

Using the parameters of the LKB models, the results from DORES includes the Normal Tissue Complication Probability (NTCP) as well as the Equivalent Uniform Dose (EUD). The NTCP values were chosen for the evaluation since it is simple and straightforward. From the results in the previous chapter it is realized that the NTCP values for both lung fibrosis and pneumonitis are fairly low, beyond 0.05 except for the last scenario, which involves a 15 MeV electron beam. The results are summarized in tables 5 and 6 below:

SCENARIO	NTCP	EUD
10 MeV gantry 30	0.006109	2.243793
10 MeV gantry 20	0.006195	2.300171
08 MeV gantry 50	0.007169	2.89475
10 MeV gantry 40	0.007671	3.17395
12 MeV gantry 20	0.009268	3.965578
12 MeV gantry 30	0.009355	4.004979
10 MeV gantry 50	0.01179	5.000638
12 MeV gantry 40	0.012151	5.132443
12 MeV gantry 50	0.023526	8.16943
12 MeV gantry 60	0.036731	10.40177
15 MeV gantry 50	0.067935	13.80458

**Table 5:** NTCP and EUD values for lung fibrosis for different scenarios

SCENARIO	NTCP	EUD
10 MeV gantry 30	0.006446	2.460934
10 MeV gantry 20	0.006545	2.522769
08 MeV gantry 50	0.007673	3.174887
10 MeV gantry 40	0.00826	3.481107
12 MeV gantry 20	0.010142	4.349343
12 MeV gantry 30	0.010245	4.392558
10 MeV gantry 50	0.013161	5.48457
12 MeV gantry 40	0.013596	5.629131
12 MeV gantry 50	0.027653	8.96002
12 MeV gantry 60	0.044414	11.40839
15 MeV gantry 50	0.084702	15.14051

**Table 6:** NTCP and EUD values for pneumonitis for different scenarios

It can be seen from these tables that the NTCP increases with energy and; with an exception of the first two values, increases with gantry angle. The last scenario, with 15 MeV results in relatively high NTCP values > 0.05 for both, lung fibrosis and radiation induced pneumonitis and may indicate that is unacceptable for postmastectomy radiotherapy. This is in line with the DVH results above.

Dose is not the only decisive factor for radiation pneumonitis. It has been shown by Tsougos et al 2007 [98] that the difference between the mean DVH of the complication and complication free groups is rather small. Other factors like radiation sensitivity between

patients may contribute significantly to risk of radiation-induced pneumonitis. But from this study and the generated NTCP values one can estimate that the risk of pulmonary and cardiac injuries is quite low in electron postmastectomy radiotherapy. Nevertheless, these results are not conclusive. This is because appropriate target coverage was not fulfilled in this study, using a single electron field without an unacceptable dose to the organs at risk. Moreover, the target area is not usually a square field, which is the area irradiated in our different scenarios, with a square applicator. In addition to that, the depth of the different layers within the target is not constant and the anatomy of the target area is not homogeneous. This is especially the case if the internal mammary nodes or the supraclavicular lymph nodes are included in the delineated target. In the real life scenarios, the target area is divided into sections, each of which is considered individually, as in Figure 35 below:

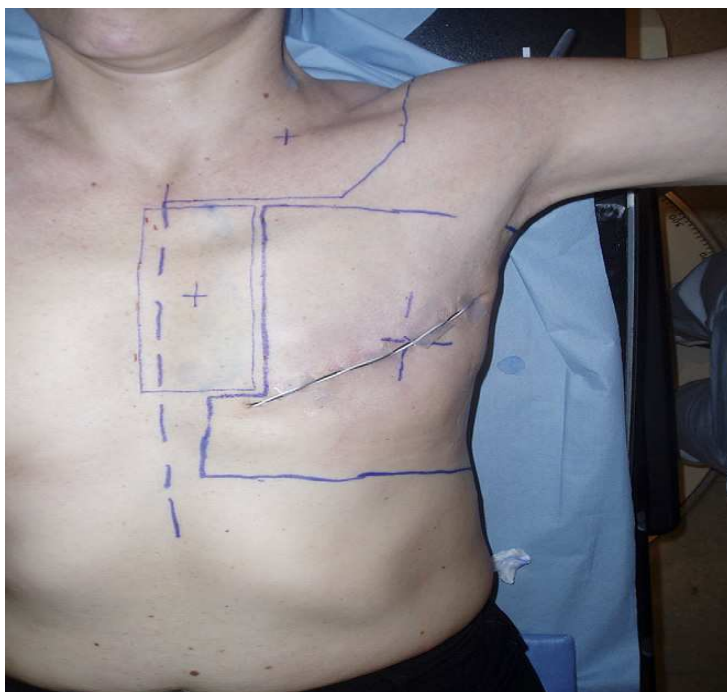


**FIGURE 35:** Different target areas including the chest wall IMN and SCV nodes

Zackirson et al (1996) reported successfully using a single electron field or postmastectomy radiotherapy. The energy used was very high, 20 MeV, but a bolus was used to shape the beam and reduce the dose to the organs at risk [101].

Electron, photons or electron/photon mix may be given to the different areas. Electron boost to some areas is also common in many cases. Beam shaping using cut-outs and addition of a bolus will insure better target coverage and fewer doses to the

surrounding health organs. Moreover, the study was performed on one patient and the dose distribution is affected by the patient's anatomy and geometry.

Due to the differences between the patients, trial and evaluation of different scenarios is the only way to find the optimum plan for that individual patient. Some treatment planning systems allow performing such trials in a short time. Yet, Monte Carlo techniques offer the most accurate calculations of dose distributions within the patients. In the near future many vendors will make use of the accuracy and precision of Monte Carlo calculations in the new treatment planning systems. Dose evaluation and visualization and calculation tools and dose response evaluation software can be endorsed in these treatment planning systems. This will insure the highest quality and maximum utilization of electron and photon treatments of areas like the thorax, where expensive modalities like intensity modulated radiotherapy (IMRT) or proton radiotherapy are not necessary.



## **CHAPTER FIVE: CONCLUSIONS AND RECOMMENDATION**

## 5.1 Conclusions

The Monte Carlo (MC) method has been shown through many research studies to calculate accurate dose distributions for clinical radiotherapy, particularly in heterogeneous patient tissues where the effects of electron transport cannot be accurately handled with conventional, deterministic dose algorithms [87]. The BEAM code and its graphical user interface facilities implemented in BEAMnrc/DOSXYZnrc and BEAMDP, allow researchers with limited software knowledge to benefit from the accuracy of Monte Carlo simulations for radiotherapy studies.

Electron beam simulation is a very sensitive procedure that requires precision and accuracy. Many sources of systematic errors have been investigated in this work. The Linear accelerator vendors do not give all the details about the beam parameters and the Linac configurations, so researchers may consider the slight alterations explained to reach to a satisfactory match between measured and calculated data. Accurate simulation is very crucial for investigations and application of Monte Carlo for treatment planning studies.

Postmastectomy radiotherapy cannot be performed with a single electron beam without beam shaping, because regardless of the energy, field size or angle, it is not possible to provide adequate target coverage. Multiple electron, photon or electron/photon mix fields with appropriate field shaping using cut-outs or a bolus with partitioned target area will allow better target coverage.

DVH and NTCP evaluation of the different scenarios - energy and gantry angle combinations- showed that the probability of radiation induced lung fibrosis and pneumonitis are fairly low below 15 MeV. Irradiation with 15 MeV electron beams may result in higher risk of lung and heart complications.

XSTING is an excellent addition to the Monte Carlo research facilities in the department. It provides accurate means for visualizing and analyzing the dose distribution in any patient and for any type of Monte Carlo studies.

DORES is documented and benchmarked dose response evaluation software. It also enhances the research facilities in the Monte Carlo laboratory, especially after the designing and utilization of XSTING.

## 5.2 Recommendations

### 5.2.1 More efficient Network Queuing System

A faster and more efficient network queuing system NQS that can handle many parallel jobs can allow making simulations and dosimetric studies in a much shorter time. This is especially important since a bigger cluster, with over 25 computers will be available for Monte Carlo studies in the laboratory in the near future.

### 5.2.2 Further studies

Having accurately simulated electrons and photons with both, normal jaws and multi-leaf collimators, the land is now fertile for Monte Carlo research. Any dosimetric study on CT data can now be achieved within a short period of time.

This work did not study the possibility for matching electron beams, which may improve target coverage without increasing the dose to the organs at risk. Careful investigation for this is recommended.

The dose received by the breast skin area is also a deterministic factor in electron beam radiotherapy. Skin complications may necessitate a pause in treatment because the pain may be non-tolerable. Unlike photons, the surface dose of electron beams is high, especially for high energies and skin sparing is not possible without a bolus. The skin dose for the different energies with and without a bolus should be studied in order to complete the evaluation of electron postmastectomy radiotherapy. It has been reported in old studies that absorbed skin doses of at least 60 Gy given at daily doses of 2 Gy are common in clinical practice and rarely produce severe acute complications [101].

Application of Monte Carlo techniques for dosimetry, radiation protection, nuclear medicine, tomotherapy and brachytherapy may also be explored. Different codes e.g. GEANT4, MCNP must be installed for some of these applications that could not be handled by the BEAM/EGSnrc code.

### 5.2.3 Documentation

The steps for installing the different software used should be documented. During the start of this work some files in the BEAM code previously installed were corrupted. The available DICOM software, for reading CT data was not compatible with the available MATLAB software, so before the completion of XSTING, dose evaluation was not possible, though previous researchers in the laboratory have used DICOM. Some commands change

with the code or the queuing system, having such commands available is of help. It is thus recommended that each researcher fill in the laboratory log book the types of obstacles and trouble-shooting actions made to overcome these obstacles. This will save a lot of time for the new researchers in managing the constraints that are not related to the soul of their research.

## Περίληψη

Στην παρούσα εργασία πραγματοποιήθηκε εξομοίωση δεσμών ηλεκτρονίων και δεσμών ηλεκτρονίων σε ακτινοθεραπεία μετά από μαστεκτομή με την χρήση τεχνικών Μόντε Κάρλο (Monte Carlo). Η διαδικασία για την επίτευξη αυτού ήταν η ακόλουθη.

Στο πρώτο στάδιο της διαδικασίας αυτής πραγματοποιήθηκαν μετρήσεις σε ομοίωμα νερού της κατανομής δόσης για διαφορετικές ενέργειες και μεγέθη πεδίων στον γραμμικό επιταχυντή SL18 της ELEKTA, ο οποίος βρίσκεται στο Πανεπιστημιακό Νοσοκομείο Λάρισας. Συγκεκριμένα λήφθηκαν μετρήσεις επί της εκατό δόσης βάθους στον κεντρικό άξονα της δέσμης (PDD) και προφίλ επί της εκατό δόσης εκτός του κεντρικού άξονα (OAR) σε βάθος της μέγιστης δόσης ( $D_{max}$ ). Ο χρησιμοποιούμενος κώδικας που εγκαταστάθηκε και χρησιμοποιήθηκε ήταν ο EGSnrc μαζί με τα προγράμματα BEAMnrcMP, DOSXYZnrc και BEAMDP. Για την εξομοίωση του γραμμικού επιταχυντή χρησιμοποιήθηκαν τα blue print της ELEKTA. Οι καμπύλες επί της εκατό δόσης και δόσης προφίλ που προέκυψαν από τις εξομοιώσεις συγκρίθηκαν με τις αντίστοιχες που λήφθηκαν στο ομοίωμα νερού. Σκοπός της σύγκρισης ήταν η διαφορά των καμπυλών να βρίσκεται εντός αποδεκτών ορίων έτσι ώστε να θεωρηθεί ότι ο γραμμικός επιταχυντής εξομοιώθηκε επιτυχώς.

Προκειμένου να επιτευχθεί η καλύτερη δυνατή ταύτιση των καμπυλών PDD έγιναν αρκετές δοκιμές για την εύρεση της κατάλληλης ενέργειας της δέσμης και του κατάλληλου ενεργειακού εύρους ή πλήρους εύρους στα μισά του μέγιστου (FWHM). Οι διαφοροποιήσεις των PDD καμπυλών ήταν μεγαλύτερες στην περιοχή ανοικοδόμησης (build-up region) και ειδικότερα στην επιφάνεια. Πιθανοί λόγοι αυτού ήταν η ύπαρξη νετρονίων, σκεδαζόμενων ηλεκτρονίων από το ομοίωμα, εξάρτησης του μετρητή, επιλογή κατάλληλου σημείου μέτρησης και άλλων παραγόντων. Η διαφορές ελαττώνονται καθώς η ενέργεια της δέσμης αυξάνεται. Στην περιοχή μετά από τη μέγιστη δόση παρατηρείται για μεγάλες ενέργειες μικρή διαφορά μεταξύ μετρήσεων και εξομοίωσης. Σε γενικές γραμμές όμως οι διαφορές αυτές δεν ξεπερνούν το 2% - 2mm εύρος.

Σε σχέση με τις καμπύλες OAR η σύγκριση έδειξε καλή ταύτιση μεταξύ μετρήσεων και εξομοιώσεων. Για την επίτευξη της ταύτισης αυτής έγινε μία σχετικά μικρή μεταβολή στα ανοίγματα των διαφραγμάτων πεδίου (jaws). Η μεγαλύτερη διαφορά μεταξύ μετρήσεων και εξομοιώσεων σημειώθηκε στον δεξί ώμο, όπου τα αποτελέσματα έδειξαν μία ελαφριά πτώση για μερικές ενέργειες και εύρη πεδίων. Σε περίπτωση που ο ένας ώμος έχει ελαφριά πτώση

σε σχέση με τον άλλο και ο άλλος βρίσκεται εντός αποδεκτών ορίων, τότε θεωρείται ότι το εξομοιωμένο προφίλ είναι σωστό.

Στο δεύτερο κομμάτι της παρούσας εργασίας μελετήθηκαν οι διαφορετικές πηγές συστηματικών λαθών στην εξομοίωση γραμμικών επιταχυντών. Αυτό σήμαινε μικρές μεταβολές στις εισαγόμενες παραμέτρους της, στον σχεδιασμό του ομοιώματος και της τοποθέτησης του και της διαμόρφωσης των τμημάτων του γραμμικού. Σκοπός της παρούσας μελέτης ήταν να βοηθηθούν μελλοντικοί ερευνητές στην γνώση του που βρίσκεται το πιθανό λάθος κατά την εξομοίωση PDD και OAR.

Η εξομοίωση δεσμών χαμηλής ενέργειας βρέθηκε να είναι πιο ευαίσθητη στα τμήματα που βρίσκονται κάθετα στην κατεύθυνση της δέσμης ακόμα και στην περίπτωση του καθρέφτη που είναι πολύ λεπτός, ενώ η υψηλής ενέργειας δέσμες ηλεκτρονίων είναι ευεπηρεάστες στις μεταβολές στα άκρα της δέσμης, όπως τα τοιχώματα του φίλτρου σκέδασης (scattering foil) και της διάταξης εφαρμογής (applicators).

Οι καμπύλες δόσης βάθους επηρεάζονται περισσότερο από την ακριβή προσομοίωση των τμημάτων του γραμμικού επιταχυντή, ειδικότερα σε βάθη μικρότερα του μέγιστου ( $D_{max}$ ). Μικρές μεταβολές παρατηρήθηκαν στην ίδια περιοχή ως αποτέλεσμα αλλαγών στις παραμέτρους της εξομοίωσης. Οι παράμετροι εισαγωγής της δέσμης και του ομοιώματος, τμημάτων του γραμμικού επιταχυντή όπως τα τοιχώματα του φίλτρου σκέδασης, το άνοιγμα των διαφραγμάτων πεδίου και του υλικού της διάταξης εφαρμογής επηρεάζουν την εκτός του κεντρικού άξονα κατανομή της δέσμης με μεταβολή του πλευρικού σκεδαστή (side scatter).

Στο τρίτο στάδιο ο κώδικας XSTING, ο οποίος χρησιμοποιείται για στερεοτακτική ακτινοχειρουργική αναπρογραμματίστηκε και δοκιμάστηκε για να μπορεί να δέχεται δόσεις από τον κώδικα EGSnrc. Οι παραγόμενες ισοδοσιακές καμπύλες συγκρίθηκαν με τις αντίστοιχες του DOSXYZ\_show. Τα παραγόμενα DVHs επιβεβαιώθηκαν επίσης χρησιμοποιώντας δύο απλές μεθόδους απεικόνισης. Τα DVHs δε μπορούσαν να συγκριθούν με χρήση του DOSXYZ\_show γιατί το τελευταίο δεν παρέχει την δυνατότητα σκιαγράφησης των στόχων άρα και την παραγωγή DVHs. Στη συνέχεια δέσμες ηλεκτρονίων με διαφορετικές ενέργειες, εύρη πεδίων και διαφορετική γωνία κλίσης χρησιμοποιήθηκαν για μελέτες ακτινοθεραπείας μετά από μαστεκτομή. Τα παραγόμενα DVHs από το XSTING χρησιμοποιήθηκαν σαν είσοδος στο λογισμικό DORES (Dose Response Software) για να μελετηθεί η χρησιμοποιούμενη φόρμα θεραπείας του πνεύμονα σε σχέση με την πρόβλεψη

πνευμονίτιδας, που σχετίζεται με την ακτινοθεραπεία με δέσμες ηλεκτρονίων μετά από μαστεκτομή.

Η εκτίμηση της θεραπείας μετά από μαστεκτομή με τη χρήση του XSTING και DORES αποκαλύπτει ότι η πιθανότητα ακτινικής πνευμονίτιδας στην ακτινοθεραπεία με ηλεκτρόνια μετά από μαστεκτομή είναι πού μικρή. Ο κίνδυνος αυξάνει με την αύξηση της ενέργειας και της γωνίας της κεφαλής (gantry).

Η ακτινοθεραπεία μετά την μαστεκτομή δεν μπορεί να εφαρμοστεί με την χρήση μονής δέσμης ηλεκτρονίων, διότι, εκτός από την ενέργεια, το μέγεθος του πεδίου ή την γωνία, δεν είναι εφικτό να εξασφαλιστεί επαρκής κάλυψη του στόχου προς ακτινοβόληση. Πολλαπλές δέσμες ηλεκτρονίων, φωτονίων ή και συνδυασμός αυτών, με το απαραίτητο σχήμα πεδίου που θα δοθεί με διαχωρισμό της δέσμης ή την χρήση ομοιώματος θα επιτρέψει την καλύτερη κάλυψη του στόχου.

## References

1. A. J Kapur Monte Carlo Dode Calculations for Clinical Electrons and Intensity Modulated Photon Beams in Radiotherapy, PhD Thesis Stanford University (2000)
2. H.D. Suit, J. Becht, J. Leong, M. Stracher, W.C Wood, L. Verhey and M. Goitein, "Potential for improvement in radiotherapy", *Int. J. Radiat. Oncol. Biol. Phys.* 44, 777-786 (1988).
3. D.L.G Hill, P.G. Batchelor, M Holden and D.J. Hawkes, "Medical image registration", *Phys. Med. Biol.* 46, R1-R45 (2001)
4. A.J. Nederveen, J.J.W. Lagendijk and P. Hofman, "Feasibility of automatic marker detection with an a-Si flat-panel images", *Phys. Med. Biol.* 46, 1219-1230 (2001).
5. H.D. Kubo and B.C. Hill, "Respiration gated radiotherapy treatment: a technical study", *Phys. Med. Biol.* 41, 83-91 (1996)
6. J.W. Wong, M.B. Sharpe, D.A. Jaffray, V.R. Kini, J.M. Robertson, J.S Stromberg and A.A. Martinez, "The use of active breathing control (ABC) to reduce margins for breathing motion", *Int. J. Radiat. Oncol. Biol. Phys.* 44, 911-919 (1999)
7. Bruce J. Gerbi (2006) "Clinical Applications of High-Energy Electrons": Technical Basis of Radiation Therapy 4<sup>th</sup> Edition (Springer, Berlin, Heidelberg)
8. Faiz M. Khan (1994) "The Physics of Radiation Therapy" (Williams and Wilkins, Baltimore, MD)
9. Francisc Salvat (2007) "Overview of Monte Carlo: Principles and Methods" Lecture: International Workshop on Monte Carlo Codes; NPL, UK
10. Kenneth K Hogstrom and Peter Almond (2006) "Review of Electron Beam Therapy Physics" *Phys Med. Biol.* 51 pp R455- R498
11. D. W. O. Rogers (2002) "Monte Carlo Techniques in Radiotherapy" *Physics in Canada Vol 58(2)* pp 63-70
12. <http://www.breastcancersource.com/breastcancersourcehpc>
13. Early Breast Cancer Trialists' Collaborative Group (Ebcctcg) Effects Of Radiotherapy And Of Differences In The Extent Of Surgery For Early Breast Cancer On Local Recurrence And 15-Year Survival: An Overview Of The Randomised Trials. *Lancet* 2005; 366: 2087-2106
14. Thomas A. Buchholz, Eric A. Strom, George H. Perkins and Marsha D. Mcneese. Controversies Regarding The Use Of Radiation After Mastectomy In Breast Cancer *The Oncologist* 2002; 7: 539-546
15. Jan Van De Steene, Vincent Vinh-Hung, Burno Cutuli, Guy Storme. Adjuvant Radiotherapy For Breast Cancer: Effects Of Longer Follow-Up. *Radiotherapy And Oncology* 2004; 72: 35-43
16. Marc S. Rudoltz, Ryan S. Perkins, Robert W. Luthmann, Rick Croley, Scot N. Ackerman. The Role Of Radiation Therapy Post Mastectomy For Invasive Carcinoma Of The Breast: A Review. *Jacksonville Medicine* 1998
17. Eric A. Strom, Wendy A. Woodward, Angela Katz, Thomas A. Buchholz, George H. Perkins, Anuja Jhingran, Richard Theriault, Eva Singletary, Aysegul Sahin And Marsha D. Mcneese. Rregional Nodal Faliure Patterns In Breast Cancer Patients



- Treated With Mastectomy Without Radiotherapy. *Int. J. Radiation Oncology Biol. Phys.* 2005; 63(5): 1508-1513
18. Amin-Zimmerman, K. Paris, G.I. Minor, W, Spanos. Postmastectomy Chest Wall Radiation With Electron-Beam Therapy: Outcomes And Complications At The University Of Lonisville *The Cancer Journal* 2005: 11(3): 204-208
  19. Thomas A, Buchholz. Postmastectomy Radiation As A Component Of The Multi-Disciplinary Management Of Breast Cancer Patients *The Cancer Journal* 2005: 11 (3): 198-200
  20. Eng-Yen Huang, Hui-Chun Chen, Li-Min Sun, Fu-Min Fang, Hsuan-Chih Hsu, Ching-Yeh Hsiung, Yu-Jie Huang, Chang-Yu Wang, Chong-Jong Wang. Multivariate Analyses Of Locoregional Recurrences And Skin Complications After Postmastectomy Radiotherapy Using Electrons Or Photons. *Int. J. Radiation Oncology Biol. Phys.* 2006; 65 (5): 1389-1396
  21. Pauline T. Truong, Ivo A. Olivotto, Caroline H. Speers, Elaine S. Wai, Eric Berthelet, And Hosam A. Kader. A Positive Margin Is Not Always An Indication For Radiotherapy After Mastectomy In Early Breast Cancer. *Int. J. Radiation Oncology Biol. Phys.* 2004; 58 (3): 797-804
  22. Inger Højris, Jørn Andersen, Marie Overgaard And Jens Overgaard. Late Treatment Morbidity In Breast Cancer Patients Randomized To Postmastectomy Radiotherapy And Systemic Treatment Versus Systemic Treatment Alone. *Acta Oncologica* 2000; 39: 354-372
  23. Marie-Luise Sautter-Bihl, Rolf Sauer. One More Change Of Paradigm In Breast Cancer Treatment: Postmastectomy Radiotherapy For Patients With One To Three Lymph Node Metastases? *Strahlentherapie Und Onkologie* 2007; 183: 357-359
  24. Sean E. McGuire, Ana M. Gonzalez-Angulo, Eugene H. Huang, Susan L. Tucker, Shu-Wan C. Kau, Tse-Kuan Yu, Eric A. Strom, Julia L. Oh, Wendy A. Woodward, Welela Tereffe, Kelly K. Hunt, Henry M. Kuerer Aysegul A. Sahin, Gabriel N. Hortobagyi, And Thomas A. Buchholz. Postmastectomy Radiation Improves The Outcome Of Patients With Locally Advanced Breast Cancer Who Achieve A Pathologic Complete Response To Neoadjuvant Chemotherapy *Int. J. Radiation Oncology Biol. Phys.* 2007; 68 (4): 1004-1009
  25. Elizabeth Ceilley, Reshma Jagsi, Saveli Goldberg, Laurent Grignon, Lisa Kachnic, Simon Powell And Alphonse Taghian. Radiotherapy For Invasive Breast Cancer In North America And Europe: Results Of A Survey. *Int J. Radiation Oncology Biol. Phys* 2005; 61 (2): 365-373
  26. R. Jagsi, A. Makris, S. Goldber A.Taghian. Intra-European Differences In Radiotherapeutic Management Of Breast Cancer: A Survey Study. *Clinical Oncology* 2006; 18: 369-375
  27. Ivo A. Olivotto, Pauline T. Truong, Boon Chua, Peter Maccallum. Postmastectomy Radiation Therapy: Who Needs It? *Journal Of Clinical Oncology* 2004; 22 (21): 4237-4239
  28. Jason Chia-Hsien Cheng, Chii-Ming Chen, Mei-Ching Liu, Mei-Hua Tsou, Po-Sheng Yang, James Jer-Min Jian, Skye Hongiun Cheng, Stella Y. Tsai, Szu-Yun Leu and Andrew T. Huang—Locoregional Failure Of Postmastectomy Patients With 1-3

- Positive Axillary Lymph Nodes Without Adjuvant Radiotherapy. *Int. J. Radiation Oncology Biol. Phys.* 2002; 52 (4): 980-988
29. Marie Overgaard, Hanne M. Nielsen, Jens Overgaard. Is The Benefit Of Postmastectomy Irradiation Limited to Patients With Four Or More Positive Nodes, as Recommended in International Consensus Reports? A Subgroup Analysis Of The DBCG 82 B&C Randomized Trials. *Radiotherapy and Oncology* 2007; 82 247-253
  30. Pauline T. Truong, Ivo A. Olivotto, Timothy J. Whelan, Mark Levine (2004) "Clinical Practice Guidelines For The Care And Treatment Of Breast Cancer: 16. Locoregional Post-Mastectomy Radiotherapy" *Cmaj*; 170 (8): 1263-73
  31. Abram Recht, Stephen B. Edge, Lawrence J. Solin, David S. Robinson, Alison Estabrook, Richard E. Fine, Gini F. Fleming, Silvia Formenti, Clifford Hudis, Jeffrey J. Kirshner, David A. Krause, Robert R. Kuske, Amy S. Langer, George W. Sledge, Jr, Timothy J. Whelan, And David G. Pfister. ASCO SPECIAL ARTICLE: Postmastectomy Radiotherapy: Guidelines Of The American Society Of Clinical Oncology *J. Clin. Oncol.* 2001; 19: 1539-1569
  32. H. Probst, S. Griffiths. Overview: Moving To A High-Tech Approach To The Irradiation Of Early Breast Cancer: Is It Possible To Balance Efficacy, Morbidity And Resource Use. *Clinical Oncology* 2006; 18: 268-275
  33. W. Beavis. Treatment Planning Challenges In Breast Irradiation: The Ideal And The Practical. *Clinical Oncology* 2006; 18: 200-209
  34. A Suleiman, H. Omer, K Theodorou And C Kappas. Review On Intra And Inter-Fractional Tumor Motion Measurements For Radiotherapy *Int J. Sci. Res.* 2006; 15: 41-55
  35. D Parkin, SL Whelan, J Ferlay Cancer Incidence in Five Continents. Lyon, France: International Agency For Research On Cancer Scientific Publications 1997; VII
  36. Hes Pearson Coronary Occlusion Following Thoracic Radiotherapy 2 Cases. *Proc R Soc Med* 1957; 50: 516
  37. Hes. Pearson Incidental Dangers Of X-Ray Therapy. *Lancet* 1958; 1: 222-223
  38. Inger Højris, Jørn Andersen, Marie Overgaard And Jens Overgaard. Late Treatment Morbidity In Breast Cancer Patients Randomized To Postmastectomy Radiotherapy And Systemic Treatment Versus Systemic Treatment Alone. *Acta Oncologica* 2000; 39: 354-372
  39. Editha A. Krueger, Matthew J. Schipper, Todd Koelling, Robin B. Marsh, James B. Butler And Lori J. Pierce. Cardiac Chamber And Coronary Artery Doses Associated With Postmastectomy Radiotherapy Techniques To The Chest Wall And Regional Nodes. *Int. J. Radiation Oncology Biol. Phys.* 2004; 60(4): 1195-1203
  40. J. A. Dewar. Overview: Postmastectomy Radiotherapy *Clinical Oncology* 2006; 18: 185-190
  41. John J. Doyle, Alfred I. Neugut, Judith S. Jacobson, Jian Wang, Russell McBride, Alison Grann, Victor R. Grann, And Dawn Hershman. Radiation Therapy, Cardiac Risk Factors, And Cardiac Toxicity In Early-Stage Breast Cancer Patients. *Int. J. Radiation Oncology Biol. Phys.* 2007; 68 (1): 82-93
  42. Jerzy Z Skoczylas, Søren M. Bentzen, Marie Overgaard And Jens Overgaard. Time Course Of Radiological Lung Density Changes After Postmastectomy Radiotherapy. *Acta Oncologica* 2000; 39 (2): 181-187

43. E. Senkus-Konefka, J. Jassem. Overview: Complications Of Breast-Cancer Radiotherapy. *Clinical Oncology* 2006; 18: 229-235
44. Pehr A.R.M Lind, Berit Wemmberg, Giovanna Gagliardi and Tommy Fornander. Pulmonary Complications Following Different Radiotherapy Techniques For Breast Cancer; And The Association To Irradiated Lung Volume And Dose Breast Cancer Research and Treatment 2001; 69: 199-210
45. J.C.M Theuws, S.L.S Kwa, A.C Wagenaar, L.J Boersma, E.M.F Damen, S.H.Muller, P. Baas And J.V Lebesque. Dose-Effect Relations For Early Local Pulmonary Injury After Irradiation For Malignant Lymphoma And Breast Cancer. *Radiotherapy and Oncology* 1998; 48: 33-43
46. Jermy D Ruben, Sidney Davis, Cherie Evans, Phillip Jones, Frank Gagliardi, Matthew Haynes And Alistair Hunter. The Effect Of Intensity-Modulated Radiotherapy On Radiation-Induced Second Malignancies. *Int. J. Radiation Oncology Biol. Phys.* 2008; 70 (5): 1530-1536
47. Silvia Johansson, Hans Svensson, And Juliana Denekamp. Dose Response And Latency For Radiation-Induced Fibrosis, Edema, And Neuropathy In Breast Cancer Patients *Int. J. Radiation Oncology Biol. Phys.* 2002; 52 (5): 1207-1219
48. Christian S Hinrichs, Nancy L Watroba, Hamid Rezaishiraz William Giese, Thelma Hurd, Katheleen A Fassl And Stephen B Edge. Lymphedema Secondary To Postmastectomy Radiation: Incidence And Risk Factors *Annals Of Surgical Oncology* 2004; 11 (6): 573-580
49. Thomas Hehr, Johannes Classen, Marco Huth, Ilona Durst, Gunter Christ, Michael Bamberg, Wilfried Budach. Postmastectomy Radiotherapy Of The Chest Wall: Comparison Of Electron-Rotation Technique And Common Tangential Photon Fields *Strahlenther Onkol* 2004; 180: 629-36
50. Marie Overgaard, Per S. Hansen, Jens Overgaard, Carsten Rose, Michael Andersson, Flemming Bach Mogens Kjaer, Carl C. Gadeberg, Henning T. Mouridsen, Maj-Britt Jensen, Karin Zedeler. Postoperative Radiotherapy In High-Risk Premenopausal Women With Breast Cancer Who Receive Adjuvant Chemotherapy. *Danish Breast Cancer Cooperative Group 82b Trial. N Engl J Med* 1997;337 (14): 949-955
51. Marie Overgaard, Maj-Britt Jensen, Jens Overgaard, Per S Hansen, Carsten Rose, Michael Andersson, Claus Kamby, Mogens Kjaer, Carl C Gadeberg, Birgitte Bruun Rasmussen, Mogens Blichert-Toft and Henning T Mouridsen. Postoperative Radiotherapy In High-Risk Postmenopausal Breast-Cancer Patients Given Adjuvant Tamoxifen: Danish Breast Cancer Cooperative Group DBCG 82c randomised trial. *Lancet* 1999; 353 (9165): 1641-1648
52. Joseph Ragaz, Stewart M. Jackson, Nhu Le, Ian H. Plenderleith, John J. Spinelli, Vivian E. Basco, Kenneth S. Wilson, Margaret A. Knowling, Christopher M.L. Coppin, Marilyn Paradis, Andrew J. Coldman, and Ivo A. Olivotto. Adjuvant radiotherapy and chemotherapy in node-positive premenopausal women with breast cancer. *N Engl J Med* 1997;337 (14): 956-962
53. Joseph Ragaz, Ivo A. Olivotto, John J. Spinelli, Norman Phillips, Stewart M. Jackson, Kenneth. S. Wilson, Margaret A. Knowling, Christopher M. L. Coppin, Lorna Weir, Karen Gelmon, Nhu Le, Ralph Durand, Andrew J. Coldman, Mohamed Manji. Locoregional Radiation Therapy In Patients With High-Risk Breast Cancer Receiving

- Adjuvant Chemotherapy: 20-Year Results Of The British Columbia Randomized Trial. *J. Natl Cancer Inst* 2005; 97 (2): 116-126
54. Marnee M. Spierer, Linda X. Hong, Raquel T. Wagman, Matthew S. Katz, Rebecca L. Spierer And Beryl McCormick. Postmastectomy CT-Based Electron Beam Radiotherapy: Dosimetry, Efficacy, And Toxicity In 118 Patients. *Int. J. Radiation Oncology Biol. Phys.* 2004; 60 ( 4): 1182-1189
  55. Val Gebski, Marivic Lagleva, Anthony Keech, John Simes, Allan O. Langlands Survival Effects Of Postmastectomy Adjuvant Radiation Therapy Using Biologically Equivalent Doses: A Clinical Perspective. *Journal Of The National Cancer Institute* 2006; 98 (1): 26-38
  56. Carolyn W. Taylor, Andrew Nisbet, Paul McGale, and Sarah C. Darby. Cardiac Exposures in Breast Cancer Radiotherapy: 1950s-1990s. *Int. J. Radiation Oncology Biol. Phys.* 2007; 69 (5): 1484-1495
  57. Lori J. Pierce, James B. Butler, Mary K. Martel, Daniel P. Normolle, Tod Koelling, Robin B. Marsh, Allen S. Lichter, And Benedick A. Fraass. Postmastectomy Radiotherapy Of The Chest Wall: Dosimetric Comparison Of Common Techniques *Int. J. Radiation Oncology Biol. Phys.* 2002; 52 (5) 1220-1230
  58. Eliahu Gez. Postmastectomy Radiotherapy In Breast Cancer With High Risk Of Relapse: Current And Future Approaches. *J. Future Oncology* 2005; 6: 767-769
  59. Deborah Sonnik, Raj N. Selvaraj, Clare Faul, Kristina Gerszten, Dwight E Heron And Gwendolyn C. King. Treatment Techniques For 3D Conformal Radiation To Breast And Chest Wall Including The Internal Mammary Chain. *Medical Dosimetry* 2007; 32 (1): 7-12
  60. Eliahu Gez, Nurit Ashaf, Rachel Bar-Deroma, Edward Rosenblatt And Abraham Kuten. Postmastectomy Electron-Beam Chest-Wall Irradiation In Women With Breast Cancer. *Int. J. Radiation Oncology Biol. Phys.* 2004; 60 (4): 1190-1194
  61. Mette S. Thomsen, Marten Berg, Hanne Nielsen, Andres Pedersen, Marie Overgaard, Marianne Ewertz, Thomas Block, Hans Brodersen, Claudio Caldera, Eric Jakosen, Claus Kamby, Flemming Kristoffersen, Dorte Klitgaard, Mette Nielsen, Lars Stenbygaard, Sune Zimmermann, Cai Grau. Postmastectomy in Denmark: from 2D to 3D treatment planning guidelines of The Danish Breast Cancer Cooperative Group. *Acta Oncologica.* 2008; 47:654-661
  62. Youlia M. Kirova, Francois Campana, Nathalie Fournier-Bidoz, Anne Stilhart, Remi Dendale, Marc A. Bollet, and Alain Fourquet. Postmastectomy Electron Beam Chest Wall Irradiation In Women With Breast Cancer: A Clinical Step Toward Conformal Electron Therapy *Int. J. Radiat. Oncol. Biol. Phys.* 2007; 69 (4): 1139-44
  63. David K. Gaffney, Christopher M. Lee, Dennis D. Leavitt, Dennis C. Shrieve, And J. Robert Stewart. Electron Arc Irradiation Of The Postmastectomy Chest Wall In Locally Recurrent And Metastatic Breast Cancer. *Am. J. Clin. Oncol.* 2003; 26 (3): 241-246
  64. David K. Gaffney, Dennis D. Leavitt, Alexander Tsodikov, Lynn Smith, Gordon Watson, Gregory Patton, Fred A. Gibbs, And J. Robert Stewart. Electron Arc Irradiation Of The Postmastectomy Chest Wall With CT Treatment Planning: 20-Year Experience. *Int. J. Radiation Oncology Biol. Phys.* 2001; 51 (4): 994-1001

65. Fred Deigert, Walter Gunn, Fred Lindemann, Tim Stack, And Tom Cherewick. A Blended Beam Technique To Decrease Toxic Effects Of Post Mastectomy Irradiation By Combining And Sequentially Mixing Electrons And Photons Medical Dosimetry. 1995; 20 (3): 183- 190
66. Limbergen, Erik Van, Weltens, Caroline. New Trends In Radiotherapy For Breast Cancer. Current Opinion In Oncology 2006; 18 (6) 555-562
67. Damien C Weber, Carmen Ares, Antony J Lomax, And John M Kurtz. Radiation Therapy Planning With Photons And Protons For Early And Advanced Breast Cancer: An Overview Radiat Oncol. 2006
68. Editha A. Krueger, Benedick A. Fraass, Daniel L. Mcshan, Robin Marsh And Lori J. Pierce. Potential Gains For Irradiation Of Chest Wall And Regional Nodes With Intensity Modulated Radiotherapy. Int. J. Radiation Oncology Biol. Phys. 2003; 56 (4): 1023-1037
69. W Xiong, J Li, L Chen, R A Price, G Freedman, M. Ding, L Qin J Yang And C-M Ma. Optimization Of Combined Electron And Photon Beams For Breast Cancer. Physics In Medicine and Biology 2004; 49: 1973-1989
70. Ajay K Bhatnagar, Edward Brandner, Deborah Sonnik, Andrew Wu, Shalom Kalnicki, Melvin Deutsch And Dwight E. Heron. Intensity Modulated Radiation Therapy (IMRT) Reduces The Dose To The Contralateral Breast When Compared To Conventional Tangential Fields For Primary Breast Irradiation Breast Cancer Research and Treatment 2006; 96: 41-46
71. Mark W. McDonald, Karen D. Godette, Elizabeth K. Butker, Lawrence W. Davis, And Peter A. S. Johnstone. Long-Term Outcomes of IMRT For Breast Cancer: A Single-Institution Cohort Analysis. Int. J. Radiation Oncology Biol. Phys. 2008; 72 (4): 1031-1040
72. George X Ding, An investigation of Radiotherapy Electron Beams Using Monte Carlo Techniques PhD thesis Ottawa-Carleton Institute of Physics (1995)]
73. I. Kawrakow (2000) "Accurate Condensed History Monte Carlo Simulation of Electron Transport. I. EGSnrc, The New EGS4 Version" Med. Phys. Vol. 27(3) pp485-498
74. I. Kawrakow and D. W. O. Rogers, The EGSnrc Code System: Monte Carlo simulation of electron and photon transport, NRC Report PIRS-701
75. D. W. O. Rogers. Review Fifty Years Of Monte Carlo Simulations For Medical Physics. Phys. Med. Biol. 2006; 51: R287-R301
76. Cylger J E., Lochrin C. Daskalov G. M., Zohr R. Esche B. Eapen L. Grimard L., and Caudrelier JM "CLINICAL USE OF A COMMERCIAL MONTE CARLO TREATMENT PLANNING SYSTEM FOR ELECTRON BEAMS (2005) Phys. Med. Biol. 50 1029-1034
77. MONTE CARLO FOR ELECTRON RADIOTHERAPY TREATMENT PLANNING" 1998 Radiation Physics and Chemistry 53 217-227
78. Faddegon Bruce, Balogh Judith, Mackenzie Robert and Scora Daryl "CLINICAL CONSIDERATIONS OF MONTE CARLO FOR ELECTRON RADIOTHERAPY TREATMENT PLANNING" 1998 Radiation Physics and Chemistry 53 217-227
79. ELEKTA ONCOLOGY SYSTEM SL18 manual
80. D. W. O. Rogers, B. Walters, and I. Kawrakow (2004) "BEAMnrc Users Manual" NRC Report PIRS 509(a) rev I, 2004.

81. B. R. B. Walters and D. W. O. Rogers. DOSXYZnrc Users Manual. NRC Report PIRS 794 (rev B)
82. J. R. Treurniet, B. R. Walters, I. Kawrakow and D. W. O. Rogers *BEAMnrc, DOSXYZnrc and BEAMDP GUI User's Manual* NRCC Report *PIRS-0623(rev C)*
83. STATDOSE for 3D dose distributions H.C.E. McGowan, B.A. Faddegon and C-M Ma NRCC Report PIRS-0509(F) 2007
84. I. Tsougos, I. Grout, K. Theodorou, C. Kappas: A free software for the evaluation and comparison of dose response models in clinical radiotherapy (DORES) *Int. J. Radiat. Biol.*, Vol. 85, No. 3, March 2009, pp. 227–237
85. P Bjork.; T Knoos. and P Nilsson. Influence of Initial Electron Beam Characteristics on Monte Carlo Calculated Absorbed Dose Distribution for Linear Accelerator Electron Beams *Phys. Med Biol.* 2002: **47**; 4019-404.
86. International Commission on Radiation Units and Measurements. Physical Characteristics of Electron Beams *Journal of the ICRU.* 2004: **4 (1)**
87. I. J. Chetty, B. Curran, J. E Cygler, J. J DeMarco, G. Ezzell, B. A Faddegon, I. Kawrakow, P.J Keall, H. Liu, C. M Ma, D. W. O Rogers, J Seuntjens, D. Sheikh-Bagheri, J. V. Siebers Report of the AAPM Task Group No. 105: Issues associated with clinical implementation of Monte Carlo-based photon and electron external beam treatment planning *Med. Phys.* 2007: **34 (12)**; 4818-4853.
88. M. Bieda, J. Anoltak, and K. B. Hogstrom Effect of Scattering Foil Parameters on Electron-Beam Monte Carlo Calculations *Med. Phys* 2001: **28(12)**; 2527-2534.
89. E. C Schreiber and B. A Faddegon Sensitivity of Large-Field Electron Beams to Variations in a Monte Carlo Accelerator Model *Phys. Med. Biol.* 2005: **50(5)**; 769-78
90. K. K Kainz, J. A Antolak, P. R. Almond, C. D Bloch and K. R. Hogstrom Dual Scattering Foil Design for Poly-energetic Electron Beams. *Phys. Med. Biol.* 2005: **50**; 755-767
91. B. H. Brown, R. H Smallwood, D. C. Barber, P. V. Lawford and D. R. Hose *Medical Physics and Biomedical Engineering*, 1999 Bristol and Philadelphia, Institute of Physics Publishing.
92. L. J. van Battum, W. van der Zee and H. Huizenga Scattered Radiation from Applicators in Clinical Electron Beams” *Phys. Med. Biol.* 2003: **48**; 2493-2507
93. G. X. Ding, J. E. Cylger, C W Yu, N. I. Kalach and G. Daskalov. A Comparison Of Electron Beam Dose Calculation Accuracy Between Treatment Planning Systems Using Either A Pencil Beam Or A Monte Carlo Algorithm. *Int. J Radiation Oncology Biol. Phys.* 2005: 63 (2): 622-633
94. S. J Clenton, P. M. Fisher, J. Conway, P. Kirkbride and M. K. Hatton. The Use of Lung Dose–Volume Histograms in Predicting Post-radiation Pneumonitis After Non-conventionally Fractionated Radiotherapy for Thoracic Carcinoma. *Clinical Oncology.* 2005: **17 (8)**; 599-603
95. M. V. Graham, J. A. Purdy, B. Emami, W. Harms, W. Bosch, M. A. Lockett and C. A. Perez. Clinical dose–volume histogram analysis for pneumonitis after 3D treatment for non-small cell lung cancer (NSCLC) *Int. J. Radiation Oncology Biol. Phys.* 1999: 45 (2); 323-329

96. G. Gagliardi, I. Lax, S. Soderstrom, G. Gyenes and LE. Rutqvist. Prediction of excess risk of long-term cardiac mortality after radiotherapy of stage I breast cancer. *Radiother Oncol.* 1998: **46(1)**:63-71
97. James E. Trosko, Chia-Cheng Chang, Brad L. Upham and Mei-Hui Tai Low-dose ionizing radiation: induction of differential intracellular signalling possibly affecting intercellular communication. *Radiation and Environmental Biophysics* 2005 **44(1)**:3-9
98. M. Tubiana. Prevention of cancer and the dose-effect relationship: the carcinogenic effects of ionizing radiations. *Cancer Radiother.* 2009; **13(4)**:238-58
99. E B. Podgorsak *RADIATION ONCOLOGY PHYSICS: A HANDBOOK FOR TEACHERS AND STUDENTS INTERNATIONAL ATOMIC ENERGY AGENCY VIENNA*, 2005
100. Ioannis Tsougos, Per Nilsson, Kiki Theodorou, Elizabeth Kjellen, Sven-Borje Ewers, Olof Jarlman, Bengt K Lind, Constantin Kappas and Panayiotis Mavroidis NTCP modeling and pulmonary function tests evaluation for the prediction of radiation induced pneumonitis in non-small-cell lung cancer radiotherapy. *Phys. Med. Biol.* 2007: **52**; 1055-1073
101. Bjorn Zackirson and Mikael Karlsson. Matching of electron beams for conformal therapy of target volumes at moderate depths. *Radiotherapy and Oncology* 1996: **39**; 261-270
102. Pedro Andreo, David T Burns, Klaus Hohlfeld, M Saiful Huq, Tatsuaki Kanai, Fedele Laitano, Vere Smyth, Stefaan Vynckier. *ABSORBED DOSE DETERMINATION IN EXTERNAL BEAM RADIOTHERAPY: An International Code Of Practice For Dosimetry Based On Standards Of Absorbed Dose To Water.* International Atomic Energy Agency IAEA 2004 (**V.11b**)



## APPENDIX

### APPENDIX 1: Worksheet for measurement correction

#### 7.10. Worksheet

##### Determination of the absorbed dose to water in an electron beam

User: \_\_\_\_\_ Date: \_\_\_\_\_

##### 1. Radiation treatment unit and reference conditions for $D_{w,Q}$ determination

Accelerator: \_\_\_\_\_ Nominal energy: \_\_\_\_\_ MeV  
 Nominal dose rate: \_\_\_\_\_ MU min<sup>-1</sup> Measured  $R_{50}$ : \_\_\_\_\_ g cm<sup>-2</sup>  
 Reference phantom: ☐ water ☐ plastic obtained from ☐ ionization ☐ dose curves  
 Reference field size: \_\_\_\_\_ cm x cm Reference SSD: \_\_\_\_\_ 100 cm  
 Beam quality,  $Q(R_{50,w})$ : \_\_\_\_\_ g cm<sup>-2</sup> Reference depth  $z_{ref,w} = 0.6 R_{50} - 0.1$ : \_\_\_\_\_ g cm<sup>-2</sup>

##### 2. Ionization chamber and electrometer

Ionization chamber model: \_\_\_\_\_ Serial no.: \_\_\_\_\_ Type: ☐ pp ☐ cyl  
 Chamber wall / window material: \_\_\_\_\_ thickness: \_\_\_\_\_ g cm<sup>-2</sup>  
 Waterproof sleeve / cover material: \_\_\_\_\_ thickness: \_\_\_\_\_ g cm<sup>-2</sup>  
 Phantom window material: \_\_\_\_\_ thickness: \_\_\_\_\_ g cm<sup>-2</sup>  
 Absorbed-dose-to-water calibration factor  $N_{D,w,Q_0}$  = \_\_\_\_\_ ☐ Gy nC<sup>-1</sup> ☐ Gy rdg<sup>-1</sup>  
 Calibration quality  $Q_0$ : ☐ <sup>60</sup>Co ☐ electron beam Calibration depth: \_\_\_\_\_ g cm<sup>-2</sup>  
 If  $Q_0$  is electron beam, give  $R_{50}$ : \_\_\_\_\_ g cm<sup>-2</sup>  
 Reference conditions for calibration  $P_s$ : \_\_\_\_\_ kPa  $T_s$ : \_\_\_\_\_ °C Rel. humidity: \_\_\_\_\_ %  
 Polarizing potential  $V_f$ : \_\_\_\_\_ V Calibration polarity: ☐ +ve ☐ -ve ☐ corrected for polarity effect  
 User polarity: ☐ +ve ☐ -ve  
 Calibration laboratory: \_\_\_\_\_ Date: \_\_\_\_\_  
 Electrometer model: \_\_\_\_\_ Serial no.: \_\_\_\_\_  
 Calibrated separately from chamber: ☐ yes ☐ no Range setting: \_\_\_\_\_  
 If yes Calibration laboratory: \_\_\_\_\_ Date: \_\_\_\_\_

##### 3. Phantom

Water phantom window material: \_\_\_\_\_ thickness: \_\_\_\_\_ g cm<sup>-2</sup>  
 Plastic phantom phantom material: \_\_\_\_\_ density: \_\_\_\_\_ g cm<sup>-3</sup>  
 depth scaling factor  $c_{pl}$ : \_\_\_\_\_ reference depth  $z_{ref,pl} = z_{ref,w} / c_{pl}$ : \_\_\_\_\_ g cm<sup>-2</sup>  
 fluence scaling factor  $h_{pl}$ : \_\_\_\_\_

##### 4. Dosimeter reading <sup>a</sup> and correction for influence quantities

Uncorrected dosimeter reading at  $V_f$  and user polarity: \_\_\_\_\_ ☐ nC ☐ rdg  
 Corresponding accelerator monitor units: \_\_\_\_\_ MU  
 Ratio of dosimeter reading and monitor units:  $M_f$  = \_\_\_\_\_ ☐ nC MU<sup>-1</sup> ☐ rdg MU<sup>-1</sup>  
 (i) Pressure  $P$ : \_\_\_\_\_ kPa Temperature  $T$ : \_\_\_\_\_ °C Rel. humidity (if known): \_\_\_\_\_ %  
 $k_{TP} = \frac{(273.2 + T) P_a}{(273.2 + T_s) P}$  = \_\_\_\_\_  
 (ii) Electrometer calibration factor  $k_{elec}$ : ☐ nC rdg<sup>-1</sup> ☐ dimensionless  $k_{elec}$  = \_\_\_\_\_



(iii) Polarity correction <sup>a</sup>      rdg at  $+V_f$ :  $M_+$  = \_\_\_\_\_      rdg at  $-V_f$ :  $M_-$  = \_\_\_\_\_

$$k_{pol} = \frac{|M_+| + |M_-|}{2M} = \underline{\hspace{2cm}}$$

(iv) Recombination correction (two-voltage method)

Polarizing voltages:       $V_1$  (normal) = \_\_\_\_\_ V       $V_2$  (reduced) = \_\_\_\_\_ V

Readings <sup>f</sup> at each V:       $M_1$  = \_\_\_\_\_       $M_2$  = \_\_\_\_\_

Voltage ratio  $V_1 / V_2$  = \_\_\_\_\_      Ratio of readings  $M_1 / M_2$  = \_\_\_\_\_

Use Table 4.VII for a beam of type:      ☐ pulsed      ☐ pulsed-scanned

$a_0$  = \_\_\_\_\_       $a_1$  = \_\_\_\_\_       $a_2$  = \_\_\_\_\_

$$k_s = a_0 + a_1 \left( \frac{M_1}{M_2} \right) + a_2 \left( \frac{M_1}{M_2} \right)^2 = \underline{\hspace{2cm}} \quad s, h$$

Corrected dosimeter reading at the voltage  $V_f$ :

$$M_Q = M_1 k_{pl} k_{TP} k_{dec} k_{pol} k_s = \underline{\hspace{2cm}} \quad \square \text{ nC MU}^{-1} \quad \square \text{ rdg MU}^{-1}$$

#### 5. Absorbed dose to water at the reference depth, $z_{ref}$

Beam quality correction factor for user quality  $Q_u$ :

If  $Q_u$  is  $^{60}\text{Co}$       Table 7.III gives

$$k_{Q,Q_0} = \underline{\hspace{2cm}}$$

If  $Q_u$  is electron beam      Table 7.IV gives

$$k_{Q,Q_{ref}} = \underline{\hspace{2cm}} \quad k_{Q,Q_{ref}} = \underline{\hspace{2cm}}$$

$$k_{Q,Q_0} = \frac{k_{Q,Q_{ref}}}{k_{Q_0,Q_{ref}}} = \underline{\hspace{2cm}}$$

If  $k_{Q,Q_0}$  derived from series of electron beam calibrations

$$k_{Q,Q_0} = \underline{\hspace{2cm}}$$

Calibration laboratory: \_\_\_\_\_ Date: \_\_\_\_\_

$$D_{w,Q}(z_{ref}) = M_Q N_{D,w,Q_0} k_{Q,Q_0} = \underline{\hspace{2cm}} \text{ Gy MU}^{-1}$$

#### 6. Absorbed dose to water at the depth of dose maximum, $z_{max}$

Depth of dose maximum:       $z_{max}$  = \_\_\_\_\_ g cm<sup>-2</sup>

Percentage depth-dose at  $z_{ref}$  for a \_\_\_\_\_ cm  $\times$  \_\_\_\_\_ cm field size:  $PDD(z_{ref})$  = \_\_\_\_\_ g cm<sup>-2</sup> = \_\_\_\_\_ %

Absorbed-dose calibration of monitor at  $z_{max}$ :

$$D_{w,Q}(z_{max}) = 100 D_{w,Q}(z_{ref}) / PDD(z_{ref}) = \underline{\hspace{2cm}} \text{ Gy MU}^{-1}$$

<sup>a</sup> Note that if  $Q_u$  is  $^{60}\text{Co}$ ,  $N_{D,w,Q_0}$  is denoted by  $N_{D,w}$ .

<sup>b</sup> If a water phantom is used set the fluence scaling factor  $k_{pl} = 1$ .

<sup>c</sup> All readings should be checked for leakage and corrected if necessary.

<sup>d</sup> If the electrometer is not calibrated separately set  $k_{dec} = 1$ .

<sup>e</sup>  $M$  in the denominator of  $k_{pol}$  denotes reading at the user polarity. Preferably, each reading in the equation should be the average of the ratios of  $M$  (or  $M_+$  or  $M_-$ ) to the reading of an external monitor,  $M_{ext}$ .

It is assumed that the calibration laboratory has performed a polarity correction. Otherwise  $k_{pol}$  is determined according to

rdg at  $+V_f$  for quality  $Q_u$ :  $M_+$  = \_\_\_\_\_      rdg at  $-V_f$  for quality  $Q_u$ :  $M_-$  = \_\_\_\_\_

$$k_{pol} = \frac{\left[ \frac{|M_+| + |M_-|}{|M|} \right]_{Q_u}}{\left[ \frac{|M_+| + |M_-|}{|M|} \right]_{Q_0}} = \underline{\hspace{2cm}}$$

<sup>f</sup> Strictly, readings should be corrected for polarity effect (average with both polarities). Preferably, each reading in the equation should be the average of the ratios of  $M_1$  or  $M_2$  to the reading of an external monitor,  $M_{ext}$ .

\* Check that  $k_2 - 1 \approx \frac{M_1/M_2 - 1}{V_1/V_2 - 1}$

\* It is assumed that the calibration laboratory has performed a recombination correction. Otherwise the factor  $k'_i = k_i/\bar{k}_{i,0}$  should be used instead of  $k_i$ . When  $Q_0$  is  $^{60}\text{Co}$ ,  $k_{i,Q_0}$  (at the calibration laboratory) will normally be close to unity and the effect of not using this equation will be negligible in most cases.

Worksheet for measurement correction [102]

## APPENDIX 2: Stopping power ratios

TABLE 7.V. SPENCER-ATTIX STOPPING-POWER RATIOS ( $\Delta = 10$  keV) WATER TO AIR ( $s_{w,air}$ ) FOR ELECTRON BEAMS, AS A FUNCTION OF BEAM QUALITY  $R_{50}$  AND RELATIVE DEPTH  $z/R_{50}$  IN WATER  
(The data are derived using Eq (B.6) in Appendix B due to Burns et al [91].)

	Beam quality $R_{50}$ (g cm <sup>-2</sup> )																
	1.0	1.4	2.0	2.5	3.0	3.5	4.0	4.5	5.0	5.5	6.0	7.0	8.0	10.0	13.0	16.0	20.0
$z_{ref}$ (g cm <sup>-2</sup> ):	0.5	0.7	1.1	1.4	1.7	2.0	2.3	2.6	2.9	3.2	3.5	4.1	4.7	5.9	7.7	9.5	11.9
$s_{w,air}(z_{ref})$ :	1.102	1.090	1.078	1.070	1.064	1.058	1.053	1.048	1.044	1.040	1.036	1.029	1.022	1.010	0.995	0.983	0.970
Relative depth in water $z/R_{50}$																	
0.02	1.076	1.060	1.042	1.030	1.020	1.012	1.004	0.997	0.991	0.986	0.980	0.971	0.963	0.950	0.935	0.924	0.914
0.05	1.078	1.061	1.044	1.032	1.022	1.014	1.006	1.000	0.994	0.988	0.983	0.974	0.965	0.952	0.937	0.926	0.916
0.10	1.080	1.064	1.047	1.036	1.026	1.018	1.010	1.004	0.998	0.992	0.987	0.978	0.970	0.957	0.942	0.931	0.920
0.15	1.083	1.067	1.050	1.039	1.030	1.022	1.014	1.008	1.002	0.997	0.992	0.983	0.975	0.961	0.946	0.935	0.924
0.20	1.085	1.070	1.053	1.043	1.034	1.026	1.019	1.012	1.006	1.001	0.996	0.987	0.979	0.966	0.951	0.940	0.929
0.25	1.088	1.073	1.057	1.046	1.037	1.030	1.023	1.017	1.011	1.006	1.001	0.992	0.984	0.971	0.956	0.945	0.933
0.30	1.091	1.076	1.060	1.050	1.041	1.034	1.027	1.021	1.016	1.010	1.006	0.997	0.989	0.976	0.961	0.950	0.938
0.35	1.093	1.079	1.064	1.054	1.045	1.038	1.032	1.026	1.020	1.015	1.011	1.002	0.995	0.982	0.966	0.955	0.943
0.40	1.096	1.082	1.067	1.058	1.049	1.042	1.036	1.030	1.025	1.020	1.016	1.007	1.000	0.987	0.972	0.960	0.948
0.45	1.099	1.085	1.071	1.062	1.054	1.047	1.041	1.035	1.030	1.025	1.021	1.013	1.006	0.993	0.978	0.966	0.953
0.50	1.102	1.089	1.075	1.066	1.058	1.051	1.046	1.040	1.035	1.031	1.027	1.019	1.012	0.999	0.984	0.971	0.959
0.55	1.105	1.092	1.078	1.070	1.062	1.056	1.051	1.045	1.041	1.036	1.032	1.025	1.018	1.005	0.990	0.977	0.964
0.60	1.108	1.095	1.082	1.074	1.067	1.061	1.056	1.051	1.046	1.042	1.038	1.031	1.024	1.012	0.996	0.984	0.970
0.65	1.111	1.099	1.086	1.078	1.072	1.066	1.061	1.056	1.052	1.048	1.044	1.037	1.030	1.018	1.003	0.990	0.976
0.70	1.114	1.102	1.090	1.082	1.076	1.071	1.066	1.062	1.058	1.054	1.050	1.043	1.037	1.025	1.010	0.997	0.983
0.75	1.117	1.105	1.094	1.087	1.081	1.076	1.072	1.067	1.064	1.060	1.057	1.050	1.044	1.033	1.017	1.004	0.989
0.80	1.120	1.109	1.098	1.091	1.086	1.081	1.077	1.073	1.070	1.066	1.063	1.057	1.051	1.040	1.025	1.012	0.996
0.85	1.123	1.112	1.102	1.096	1.091	1.087	1.083	1.080	1.076	1.073	1.070	1.064	1.059	1.048	1.033	1.019	1.004
0.90	1.126	1.116	1.107	1.101	1.096	1.092	1.089	1.086	1.083	1.080	1.077	1.072	1.067	1.056	1.041	1.028	1.011
0.95	1.129	1.120	1.111	1.106	1.102	1.098	1.095	1.092	1.090	1.087	1.085	1.080	1.075	1.065	1.050	1.036	1.019
1.00	1.132	1.124	1.115	1.111	1.107	1.104	1.101	1.099	1.097	1.095	1.092	1.088	1.083	1.074	1.059	1.045	1.028
1.05	1.136	1.127	1.120	1.116	1.113	1.110	1.108	1.106	1.104	1.102	1.100	1.096	1.092	1.083	1.069	1.055	1.037
1.10	1.139	1.131	1.125	1.121	1.118	1.116	1.115	1.113	1.112	1.110	1.109	1.105	1.102	1.093	1.079	1.065	1.046
1.15	1.142	1.135	1.129	1.126	1.124	1.123	1.122	1.120	1.119	1.118	1.117	1.114	1.111	1.104	1.090	1.075	1.056
1.20	1.146	1.139	1.134	1.132	1.130	1.129	1.129	1.128	1.128	1.127	1.126	1.124	1.121	1.115	1.101	1.086	1.066

Stopping power ratios for conversion of measured ionization to absorbed depth dose  
[101]

### APPENDIX 3: Ionization to dose conversion example

	10 MeV	ic thickness	0.102	meas R50	3.955						
6x6	10x10	14x14	20x20	Z/R50	Z	Sw,air		6x6	10x10	14x14	20x20
91.66	89.19	89.79	90.28	0.02	0.08	1.004		91.34	90.56	90.49	91.68
90.98	90.2	90.13	91.32	0.05	0.20	1.006		92.21	91.43	91.70	92.57
91.66	90.88	91.15	92.01	0.10	0.40	1.010		95.03	93.83	93.78	95.03
93.05	91.89	92.17	93.05	0.15	0.59	1.014		96.81	94.89	95.53	96.81
94.09	92.9	92.85	94.09	0.20	0.79	1.019		97.65	96.39	97.04	97.65
94.79	93.24	93.53	94.79	0.25	0.99	1.023		98.39	97.81	97.77	99.09
95.48	93.58	94.21	95.48	0.30	1.19	1.027		99.84	99.58	99.58	99.84
95.83	94.25	94.89	95.83	0.35	1.38	1.032		101.41	100.76	101.09	101.77
95.83	94.59	95.23	95.83	0.40	1.58	1.036		102.16	102.20	102.54	103.60
95.83	94.93	95.23	96.18	0.45	1.78	1.041		103.74	103.05	103.39	104.10
96.18	95.61	95.57	96.87	0.50	1.98	1.046		104.60	104.60	104.60	104.60
96.87	96.29	96.25	97.21	0.55	2.17	1.051		105.10	104.74	104.74	105.10
97.21	96.96	96.94	97.21	0.60	2.37	1.056		105.23	104.17	104.52	105.23
97.56	97.3	97.61	97.56	0.65	2.57	1.061		102.79	101.80	102.49	103.14
98.26	97.64	97.96	98.61	0.70	2.77	1.066		99.19	98.98	98.98	100.67
98.61	98.31	98.30	99.65	0.75	2.96	1.072		94.92	95.25	94.08	96.78
98.61	98.65	98.97	100.00	0.80	3.16	1.077		89.02	89.14	89.02	90.12
98.96	98.65	99.32	100.00	0.85	3.36	1.083		81.22	81.96	81.03	83.10
99.65	98.99	99.32	100.00	0.90	3.56	1.089		74.05	75.69	74.05	76.23
100.00	99.66	99.66	100.00	0.95	3.75	1.095		67.34	67.34	67.34	67.89
100.00	100	100.00	100.00	1.00	3.95	1.101		54.72	54.72	54.72	55.05
100.00	99.66	99.66	100.00	1.05	4.15	1.108		43.99	44.10	43.99	44.43
100.00	98.99	99.32	100.00	1.10	4.35	1.115		33.23	33.56	32.34	34.60
99.65	98.65	98.97	99.65	1.15	4.54	1.122		25.58	25.47	24.68	25.69
98.96	98.31	98.30	98.96	1.20	4.74	1.129		17.84	17.61	17.27	17.39
98.26	97.3	97.61	98.26								
96.88	95.95	96.60	97.21								
94.79	94.59	94.90	95.83								
93.05	92.9	92.85	94.44								
91.32	90.88	90.48	92.70								
88.54	88.85	87.76	90.28								
85.42	86.15	85.37	87.15								
82.64	82.77	82.65	83.68								
79.17	79.39	78.91	80.21								
74.99	75.68	74.82	76.73								
69.79	70.27	69.73	71.87								
62.15	62.16	62.24	63.88								
52.77	52.7	52.71	54.16								
42.70	42.9	42.51	44.09								
32.98	33.11	32.65	34.03								
24.66	24.32	23.81	24.99								
17.02	16.89	16.33	17.36								
10.77	11.49	10.88	11.81								
6.60	7.43	7.15	7.64								
3.47	3.72	3.75	3.82								
1.74	1.69	1.70	1.74								
1.39	1.35	1.36	1.39								
1.39	1.35	1.36	1.39								
1.39	1.35	1.36	1.39								
1.39	1.35	1.36	1.39								
1.39	1.35	1.36	1.39								

## APPENDIX 4: The different component modules of BEAM

### SLABS

SLABS is used for multiple slabs of arbitrary thickness and material which are perpendicular to the z axis. The outer boundary is a square.

### CONS3R

CONS3R is designed to simulate cylindrical structures that can be described using a series of (Z,R) points rotated about the Z axis. Examples of such structures are rings, cylindrical slabs and cones (primary collimators). This CM has only 3 regions: the interior of the cylindrical structure, the outside of the structure, and (possibly) the air gap at the front). The current version can only allow convex shapes in the Z direction [i.e.,  $Z(i+1)$  must be greater or equal to  $Z(i)$ , see section 14.3.3 for more details].

### CONESTAK

CONESTAK is used to simulate a stack of truncated cones. A primary collimator is a special case for CONESTAK using only one cone. Each layer is of user-defined thickness, and, within each layer, the user defines the radius of the cone at the top of the layer and at the bottom of the layer, as well as the medium inside the cone and outside the cone. In addition, the entire, multi-layered, conical structure may be surrounded by a cylindrical wall of user-defined medium. CONESTAK is rotationally symmetric about the beam axis.

### FLATFILT

This is an even more general purpose CM to simulate a set of truncated stacked cones. It is necessary for some very complex flattening filter designs. Similar to CONS3R and CONESTAK, FLATFILT is rotationally symmetric about the beam axis.

### CHAMBER

CHAMBER is used for parallel-plate ion chamber in the container with top and bottom planes of arbitrary thickness and material. CHAMBER can also be used to score the central axis dose in a water phantom outside an accelerator (see section 14.3.6 for more details). This is a cylindrical CM, rotationally symmetric about the beam axis.

### JAWS

JAWS is used for sets of paired bars or jaws, which can be in the collimator or applicator. The user defines the angle of the inner faces of the jaws with respect to the Z (beam) axis. The jaws can open in either the X or Y direction. The bars are of arbitrary thickness and material. The outer boundary of JAWS is a square centered on the beam axis.

### APPLICAT

APPLICAT is used for a set of rectangular scrapers. Each scraper is defined by the outer region of two concentric rectangles, the inner region being air. The scrapers are of arbitrary thickness, width and position relative to the reference plane ( $Z = 0$ ). The scrapers can be of different materials. The outer boundary of APPLICAT has square symmetry centered on the beam axis. This is an extension of the CM APPSQ described in the BEAMnrc paper[1].

## APPENDIX 5: DORES output chart

lung\_3\_1\_res(1)fibr [Compatibility Mode] - Microsoft Excel

Home Insert Page Layout Formulas Data Review View PDF

Cut Copy Paste Format Painter Clipboard Font Alignment Number Styles Cells Editing

A2 University Hospital Larisa

	A	B	C	D	E	F	G	H	I	J	K	L	M	N	O	P	Q
	Hospital	Patient	Organ Classification	Total Dose (Gy)	No. of fractionations	NTCP [LKB]	EUD (Gy)	s	y	m	n	D50	$\alpha/\beta$				
2	University Hospital Larisa	a	Lung	55	25	0.012150703	5.132443015			0.37	0.99	30.8	3.1				
3	University Hospital Larisa	b	lung	55	25	0.006194565	2.300171395			0.37	0.99	30.8	3.1				
4	University Hospital Larisa	c	lung	55	25	0.009268262	3.965577625			0.37	0.99	30.8	3.1				
5	University Hospital Larisa	d	lung	55	25	0.006108569	2.243793126			0.37	0.99	30.8	3.1				
6	University Hospital Larisa	e	lung	55	25	0.009354841	4.004978988			0.37	0.99	30.8	3.1				
7	University Hospital Larisa	f	lung	55	25	0.007671324	3.173950151			0.37	0.99	30.8	3.1				
8	University Hospital Larisa	g	lung	55	25	0.007168877	2.894750195			0.37	0.99	30.8	3.1				
9	University Hospital Larisa	h	lung	55	25	0.011790248	5.000637689			0.37	0.99	30.8	3.1				
10	University Hospital Larisa	i	lung	55	25	0.023525854	8.169429657			0.37	0.99	30.8	3.1				
11	University Hospital Larisa	j	lung	55	25	0.067834872	13.80457889			0.37	0.99	30.8	3.1				
12	University Hospital Larisa	k	lung	55	25	0.036731257	10.4017689			0.37	0.99	30.8	3.1				
13																	
14																	
15																	
16																	
17																	
18																	
19																	
20																	
21																	
22																	
23																	
24																	
25																	
26																	
27																	
28																	
29																	
30																	
31																	
32																	
33																	
34																	
35																	
36																	
37																	

Ready Count: 11 80%

introduction1 Thesis [Compatibility... 20\_12%20DORES[1]... Microsoft Excel - lu...